2
MIX

THE SURFACE TEMPERATURES OF SOLAR SYSTEM OBJECTS BY THERMAL EMISSION: A HOMOGENEOUS MODEL SOLUTION

Get DRA

by

George Brinton Burnett III

1971

Report No. 6

ASTROPHYSICS

School of Physics and Astronomy
University of Minnesota

The Surface Temperatures of Solar System Objects by Thermal Emission: A Homogeneous Model Solution

A Thesis
Submitted to the Faculty of the Graduate School
of the University of Minnesota

by
George Brinton Burnett III

NASA NGL 24 005 008

In Partial Fulfillment of the
Requirements for the Degree of
Master of Science

August, 1971

TABLE OF CONTENTS

Abstract

Diurnal and integral cooling curves are obtained for the Moon (1040), Mercury (570), Mars (170), Vesta, Ceres (300), Io, Europa (1000), Ganymede (600), Callisto (1200), Titan and Triton. A homogeneous model solution of the heat conduction equation is used. By comparison to infrared data the values of Gamma in brackets are found. Lack of agreement for Io and Titan suggest the presence of an atmosphere. The Moon and the Jovian satellites are considered in eclipse. A rock-dust crater model is used to determine the % rock in the craters Aristarchus (2%), Copernicus (2%), and Tycho (8%) by comparison to 12μ data.

List of Figures

Page and No.

Page and No.

Page and No.

List of Tables

Acknowledgments

The author is first indebted to Dr. Edward P. Ney for suggesting this work, for developing the necessary equipment needed to obtain much of the infrared data used in this thesis and for the use of that data.

Special thanks go to Dr. David A. Allen for many useful criticisms of the general direction and theoretical aspects of this work and for the use of his data.

Thanks also go to Thomas L. Murdock for the use of his data.

Introduction.

The germ of this thesis came about in early 1968 when work was begun on a computer program to obtain cooling curves for the lunar surface in anticipation of collecting data from the lunar eclipses of April 13 and October 6 of that year. It was decided to develop a homogeneous model for the thermal behavior of the lunar surface as was first done by Wesselink (1948), and then to improve the model by including radiative conduction and thermal parameters that were a function of temperature and depth, patterned after the work of Linsky (1966). However, no data was obtained at the University of Minnesota's O'Brien Observatory for either of these events due to weather, and the project was set aside.

Since that time infrared data is steadily being accrued on the Moon, Mercury, Mars, Ceres, Pallas, Juno, Vesta, the Jovian Satellites and Titan. These are all objects in the solar system whose thermal radiation is representative of the surface temperature. These bodies are being used as infrared calibration sources as well as to study their surface characteristics, and to these ends it was decided to revive the above project in order to compile a consistent, comprehensive set of cooling curves of both integral and non-integral surface temperatures for the twelve heretofore mentioned bodies. It is desired to do this using a single computer program with one set of thermal parameters, and further to have this same program available to compare with particular situations as they arise. Many of the cooling curves for the above bodies are available in the literature, but there generated with a variety of programs and physical parameters and presented in a variety of sizes and shapes, all of which make inter-comparison difficult.

A large number of lunar surface temperature models have been derived to fit the available infrared data with varying success. The most realistic of these, in light of the knowledge gained from the Surveyor and Apollo projects, is that by Winter and Saari (1969). The main difficulty with all of these models is that they contain enough free parameters to fit almost any curve, and thus cannot be easily distinguished upon physical grounds. Further, as David Allen (1970a) has pointed out, none of the models properly account for the presence of rocks on the lunar surface, and until they do they will never properly explain the data.

The homogeneous model, while lacking the sophistication of the later models, nevertheless for a given case is capable of fitting the data surprisingly well as is seen in this thesis. Admittedly a detailed analysis of the lunar (or other) surface requires a more complete model such as the one by Winter and Saari. But as the homogeneous model is simple, perfectly capable of obtaining surface cooling curves that agree well with the data to the accuracy necessary for this survey, and since our information about Mercury, Mars, the Asteroids, and the outer moons is meager, it was decided to use the homogeneous model for the present study.

Descriptional comments about the surface knowledge of the objects herein will be kept to a minimum to prevent the compilation of a book on the physical surface properties of the planets. The derived curves speak for themselves. Generally a surface composed of fine (less than ten microns), glassy, slightly cohesive rock powder to a depth of one to ten meters is envisioned with an increase in the static bearing strength and corresponding decrease in the thermal resistance with depth. Below this is a more or less continuous bedrock. Rocks with a variety of sizes and shapes are strewn on the surface.

Whenever possible, the thesis that rocks on the lunar surface account for the observed thermal anomalies and variation in brightness temperature with wavelength, so convincingly expounded by Allen (1970a) is tested within the confines of the model. The particular solution to the homogeneous model employed is covered in Chapter I and succeeding chapters apply this model to the above objects to obtain the desired set of cooling curves.

Chapter I - A Numerical Solution of the Homogeneous Model

1.A. - The Crank-Nicholson Equations.

The problem is to solve the heat conduction equation,

$$(1.1) \qquad \rho c \frac{\partial T}{\partial t} = \frac{\partial}{\partial x} \left(K \frac{\partial T}{\partial x}\right)$$

in the case where the thermal conductivity K, the density ρ, and the specific heat c are all independent of temperature and depth, for a semi-infinite medium. The surface of this medium is Lambertian, receiving radiative energy from the Sun and radiating to space. Surface curvature is neglected and isotropy assumed, reducing the solution to the one dimensional form with only a single spatial coordinate x reckoned positive with depth below the surface, and time t.

Because the boundary condition is non-linear, the above equation does not emit itself to analytic solution and numerical methods must be turned to. The approach taken here uses a modified Crank-Nicholson (1947) finite difference approximation. The basic approximation is:

$$(1.2) \qquad \frac{T_{i,j+1} - T_{i,j}}{k} = \frac{K}{\rho c} \left[\frac{T_{i+1,j+1} - 2T_{i,j+1} + T_{i-1,j+1}}{h^2} + \frac{T_{i+1,j} - 2T_{i,j} + T_{i-1,j}}{h^2} \right]$$

where j represents steps in time of $k = \Delta t$, and i represents steps in depth of $h = \Delta x$. Thus depth $x = ih$

and time $t = jk$. This equation is arrived at by taking the mean of the explicit finite difference representations of the j and $j + 1$ time rows of the heat conduction equation. This method is employed because it leads to an implicit solution that is inherently stable for all step sizes. Here the step size is limited only by instabilities at the non-linear boundary. Unlike explicit methods (which must be used when the specific heat and thermal conductivity are functions of temperature and depth) step sizes are chosen to be consistent with the desired accuracy of the result without having to be needlessly small just to keep the solution stable at the expense of computer time. Such a solution carried forward in time, unlike a Fourier type solution to the problem, is also not restricted to the periodic case (this is of importance in considering eclipses).

Letting $A = \frac{kK}{\rho c h^2}$, equation (1.2) reduces to the following implicit equation with three unknowns appearing on the left hand side of the equation:

$$(1.3) \quad -AT_{i-1,j+1} + (2 + 2A)\, T_{i,j+1} - AT_{i+1,j+1}$$

$$= AT_{i-1,j} + (2-2A)\, T_{i,j} + AT_{i+1,j}.$$

The resultant set of equations for all i, when properly started at the upper boundary and generated down to the desired lower depth, takes on a tridiagonal form that lends itself to an efficient solution by means of Gauss'elimination method.

1.B. - The Boundary Condition.

Conservation of energy at the surface requires the following upper boundary equation:

$$(1.4) \qquad K \frac{\partial T_{sur}}{\partial x} = \varepsilon_{IR} \sigma T_{sur}^4 - \varepsilon_B S,$$

where S = incoming solar flux

σ = Stephan-Boltzman constant

$= 1.3543 \times 10^{-12}$ cal/cm^2/°K^4/sec

ε_{IR} = mean infrared emissivity of the emitting lunar surface

ε_B = Bond emissivity (fraction of solar flux absorbed).

This study takes the Bond emissivity (1-Bond albedo) as a measure of the Solar flux absorbed at the surface. For exterior bodies this emissivity is only approximately known as their phase curves cannot be ascertained. In general this emissivity should be lowered due to an increase in albedo in the 0.9 - 5 micron region. However, since a number of questions remain in this area, and since the homogeneous solutions are not strongly dependent on the emissivity used, the Bond emissivities calculated from the measurements of Harris, (1961) are used unaltered.

The radiation from actual surfaces falls short of the ideal black body, being dependent on the physical properties of the material, surface conditions, and temperature. To make the problem tractable all such surfaces are related to the ideal black body by the total emissivity, ε, and the spectral emissivity, ε_λ, which are empirical corrections to the ideal case. For the celestial bodies dealt with here, with a general lack of detailed surface emissivity information, and in view of the fact that most substances are reasonably black in the infrared, ε_λ is considered constant at infrared wavelengths, ε_{IR}, and set equal to the Bond emissivity of the Moon, $\varepsilon_{IR} = 0.93$, in all cases. The unreclaimable error associated with ε_{IR} after equations (1.5) and (1.6) are applied is calculated to be <1°K for a change in ε_{IR} of $\pm$ 0.1. The same holds for a change in ε_B.

$$(1.5) \qquad \varepsilon_{IR}\, \sigma\, T_A^{\,4} = \varepsilon_x\, \sigma\, T_x^{\,4}$$

T_A = surface temperature associated with ε_{IR}.

T_x = surface temperature associated with another estimate of the emissivity, ε_x.

In cases where $\varepsilon_{IR} = \varepsilon_B$ (the Moon, Mercury, Vesta, and Ceres), the effects of these two emissivities on the solution are almost completely offsetting, resulting in a surface temperature equal to that obtained by setting $\varepsilon_{IR} = \varepsilon_B = 1$ as explained in Section 3.C. However, when the two emissivities are not equal and/or when one is changed, the following and preceding considerations hold.

In this thesis T_A is plotted in all cases, and the data is corrected by the spectral form of equation (1.5), equation (1.6) where $\varepsilon_x = 1$ and T_x equals the black body brightness temperature observed.

$$(1.6) \quad \varepsilon_{IR}\, C_1 \,{}^{-5}/(e^{c_2/\lambda T_A} - 1) = C_1 \,{}^{-5}/(e^{c_2/\lambda T_x} - 1)$$

$C_1 = 1.19086 \times 10^{10}$ microwatts . micron^2
$C_2 = 1.43879 \times 10^4$ microns . °K
λ = wavelength in microns

This correction is only on the order of a few degrees at most, and for darkside temperatures can often be neglected. Nevertheless the difference between T_A and T_x should be remembered as it is always present.

The neglect of the dependence of the emissivity on the angle of the emitted and absorbed radiation at the surface is equivalent to assuming a Lambertian surface. The data for the Moon and Mercury show this not to be the case. However, a detailed model for surface roughness is not within the scope of this project. In the case of the Moon and Mercury, a fit to gamma is made at night when surface roughness is not important, and the difference between the model and the data noted for the day. This difference is then applied to exterior body solutions to obtain a tentative value of Gamma where only daytime measurements over limited phase angle are available.

The parameter Gamma must be introduced at this point. It was first shown by Wesselink (1948) that equations (1.1) and (1.4) in the case under consideration admit of a homology transformation from whence it may be seen that if the insolation function and rotational period are held fixed, the whole family of solutions that follow depend only on the parameter $(K\rho c)^{1/2}$. This parameter may be physically interpreted as a measure of the resistance of the surface to a change in temperature, and is thus referred to as the thermal inertia. When calculated in c.g.s. units it takes on a range from 0.05 for basalt type rock to 0.001 for fine powders or dust, the range of interest here. Gamma is the inverse of the thermal inertia, and thus varies from 20 to 1000 in the above case. Gamma is often used in place of the thermal inertia as is done in this study. Given a fixed insolation function and rotational period, there is only one solution to the above equations (1.1) and (1.4) for a given value of Gamma. It is thus the only thermal parameter that may be ascertained for a celestial body by comparison with infrared thermal measurements.

At the boundary where it is necessary to represent equation (1.4) accurately, a fictitious temperature is introduced at the external mesh point $T_{-1,j}$ to allow the use of a central difference formulation.

$$(1.7) \quad T_{1,j+1} - T_{-1,j+1} = \frac{2h}{K}(\varepsilon_{IR}\,\sigma\,T^4_{o,j+1} - \varepsilon_B\,S)$$

Further, in order to solve the Crank-Nicholson equations (1.3), it is assumed that the heat conduction equation is valid at the surface. It then becomes possible to eliminate $T_{+1,j+1}$ between equation (1.7) and the uppermost Crank-Nicholson equation, thus allowing the equations to be put in the tridiagonal form if only $T_{o,j+1}$ can be initially determined to a good approximation. The values from the previous row's solution are of course known. The initial temperature with depth to start off the solution is discussed later. The uppermost Crank-Nicholson equation is then:

$$(1.8) \quad -AT_{-1,j+1} + (2+2A)\,T_{o,j+1} = \frac{2hA}{K}(\varepsilon_{IR}\,\sigma\,T^4_{o,j+1} - \varepsilon_B\,S)$$

$$+ AT_{-1,j} + (2-2A)\,T_{o,j} + AT_{1,j}$$

It is quickly discovered that the initial determination of $T_{o,j+1}$ to find the surface flux for the particular time row being solved is the most unstable aspect of the entire solution. Initially a simple explicit method was employed to obtain the desired surface temperature,

$$(1.9) \quad T_{o,j+1} = T_{o,j} + A(T_{-1,j} - 2T_{o,j} + T_{1,j}).$$

But this was found to lead to instabilities whenever the surface temperature gradient became steep unless unrealistically small time steps were used, (<3 minutes in the lunar case), a value even much smaller than that needed to satisfy the stability criterion for the explicit case, $r = \frac{K}{\rho c} \frac{k}{h^2} < 1$.

This problem is overcome by tying more securely the initial solution for $T_{o,j+1}$ to the known sub-surface temperatures of the previous row, making the flux allowed in at the surface consistent with that already established. This is done by using equation (1.9) to explicitly solve for the third grid point in from the surface, $T_{3,j+1}$, where the gradients are not as steep, and then working by substitution using the Crank-Nicholson equations back to the boundary and equation (1.7) to obtain $T_{o,j+1}$ initially. This procedure results in the following fourth order equation in the desired surface temperature initial estimate to start the Crank-Nicholson implicit solution at all grid points for the time j+1:

$$(1.10) \quad G_1 T^4_{o,j+1} + G_2 T_{o,j+1} + G_3 = 0 \qquad \text{where,}$$

$$G_1 = \frac{2Ah\ \varepsilon_{IR}\ \sigma}{K}$$

$$G_2 = \left[\ (2+2A) - \frac{2A^2}{(2+2A)}\ \right]$$

$$G_3 = -\frac{2A(AT_{o,j} + (2-2A)\,T_{1,j} + AT_{2,j})}{(2+2A)}$$

$$+\ \frac{2A^2\ (T_{2,j}+A(T_{1,j} - 2\ T_{2,j} + T_{3,j}))}{(2+2A)}$$

$$+\ (AT_{-1,j} + (2-2A)\ T_{o,j} + AT_{1,j})$$

$$+\ \frac{2Ah\ \varepsilon_B\ S}{K}$$

The Newton-Raphson iteration method is used to solve equation (1.10). This method converges to the final answer much more rapidly, since it is a second order process, when the initial trial value is close, as here where they are known from the previous time row. In all cases the following equation has returned a value with successive iterations <0.01°K of each other within 5 iterations;

$$(1.11)\qquad T_{o,j+1}(k+1) = \frac{3G_1\ T^4_{o,j+1}\ (k) - G_3}{4G_1\ T^3_{o,j+1}\ (k) + G_2}$$

With the introduction of this method of eliminating all the unknowns from the right hand side of equation (1.8), the step size in time is increased from the previous three minutes to two hours with no reduction in the accuracy of the solution.

1.C - Considerations with Depth.

In a further attempt to increase speed of computation, the step size with depth is increased at appropriate intervals. This is accomplished by introducing five layers into the model, and increasing the step size from one layer to the next. This allows the use of a fine depth step near the surface where it is needed to handle large temperature gradients, and progressively larger steps with depth as the gradients diminish. In practice it is found that increasing h by 1.5 across each internal boundary works well, giving results in agreement with using the same h throughout to better than 0.1°K. The layers are spaced at even intervals with depth steps. Equation (1.12) gives the differential form of the heat conduction equation applied at each interior boundary.

$$(1.12)\quad \frac{T_{b,j+1} - T_{b,j}}{k} = \frac{2K}{\rho c(h_d + h_{d+1})} \left[\frac{T_{b+1,j} - T_{b,j}}{h_{d+1}} - \frac{T_{b,j} - T_{b-1,j}}{h_d}\right]$$

The above equation is then summed between two time rows to determine the correct Crank-Nicholson equation for the internal boundary where the depth step is changed.

$$(1.13)\quad -\frac{C}{h_d} T_{b-1,j+1} + \left[1 + \frac{C}{h_d} + \frac{C}{h_{d+1}}\right] T_{b,j+1} - \frac{C}{h_{d+1}} T_{b+1,j+1} =$$

$$\frac{C}{h_d} T_{b-1,j} + \left[1 - \frac{C}{h_d} - \frac{C}{h_{d+1}}\right] T_{b,j} + \frac{C}{h_{d+1}} T_{b+1,j}$$

where

$$C = \frac{K}{\rho c} \cdot \frac{k}{(h_d + h_{d+1})}$$

$d = 1,2,3,4,5.$

This modified Crank-Nicholson equation is introduced into the tridiagonal matrix at the proper points in place of equation (1.3). The time for solution is thereby cut by a factor of four over the use of one step size over the entire depth.

Given the homogeneous model described here, as the solution is extended in depth, high harmonics in the temperature due to the changing flux at the surface damp out leaving a sinusoidal solution which reduces in amplitude to a constant. This constant temperature is simply the average of the surface temperature over one period. Radar studies of the Moon have shown this to be the case to first order (Troitsky et al., 1968). This periodic picture holds except during eclipse (where the depth the thermal wave penetrates is only a small fraction of the diurnal depth and the initial temperature distribution is known from the diurnal solution), and thus it is useful to use the Fourier solution to the problem to help visualize what is going on, to establish the initial temperature with depth, and to determine what depth the solution should be taken to. The homogeneous solution for the first harmonic is (Wesselink, 1948):

(1.14) $T(x,t) = A + Be^{-x/\lambda}\cos(-x/\lambda + 2\ t/P + \varepsilon)$, where

A = constant temperature at large depth

B = amplitude of first harmonic

P = diurnal period

λ = thermal wavelength = $\left(\frac{KP}{\rho c \pi} \right)^{1/2}$

ε = constant phase lag (appreciable for small Gamma or high spin rate).

With initial guesses at A and B from previous knowledge and use of the black body equilibrium temperature at full phase, equation (1.14) is used by the program to determine the initial temperature distribution with depth in starting the solution off. The solution is carried to a depth of five thermal wavelengths where the amplitude of the fluctuation is e^{-5} times the surface temperature amplitude. This is 0.67% of the surface amplitude or 2°K for the Moon, and small enough to be considered constant. At this depth then the solution is held at a constant temperature which is the average of the surface temperature. Knowledge of this constant temperature also puts the final Crank-Nicholson equation in the proper tridiagonal form. Using this depth as opposed to one greater effects the solution by <0.1°K. All solutions are carried through a minimum of four periods to relax the solution. The bottom temperature is recomputed at the conclusion of the first period. The variation between this bottom temperature and that of the final period is always less than .1°K. In general it is found that a 10°K error in the bottom temperature at five thermal wavelengths results in a 1°K error in the surface temperature.

When considering rocks of Gamma equal to twenty in the succeeding chapters, the above is also held to. This means that the bottom temperature of the rock is not held to the bottom temperature of the Gamma 1000 surrounding material, but rather has a bottom temperature consistent with its own average surface temperature (a value some 100°K warmer than the Gamma 1000 case at night). This means that sizable rocks are being considered, greater than a thermal wavelength or about one meter for the Moon. Such a procedure is reasonable as it has been shown that for such large slabs, negligible heat is transferred between the rock and the sand around it even in the case of the large gradients that may exist on the Moon or Mercury (Roelof, 1967). The three dimensional effects of rocks are not dealt with here.

In order to easily generalize the program to celestial bodies other than the Moon, the depth step is calculated in terms of the thermal wavelength, and the time step is calculated in terms of the diurnal period of the particular body under investigation.

When this is done, the accuracy of the solution for a given choice of step sizes becomes nearly independent of Gamma and the particular object.

1.D - The Solution.

Everything needed to solve the proposed homogeneous model in an efficient manner is now established. In section 1.B the uppermost Crank-Nicholson equation is reduced to two unknowns on the left hand side, and in section 1.C the last equation is put in a similar form by knowledge of the constant bottom temperature. The Crank-Nicholson equations for solution now fall into the following tridiagonal form:

$$
\begin{aligned}
a_{-1}T_{-1} + b_{-1}T_o \qquad\qquad\qquad &= d_{-1} \\
a_oT_{-1} + b_oT_o + c_oT_1 \qquad &= d_o \\
a_1T_o + b_1T_1 + c_1T_2 &= d_1 \\
\text{(1.15)} \quad \text{-------------------} \qquad & \\
a_{n-1}T_{n-2} + b_{n-1}T_{n-1} &= d_{n-1}
\end{aligned}
$$

These n+1 equations and n+1 unknown temperatures are then solved by Gauss' elimination method (Smith, 1965, p. 20). Here the first equation is used to eliminate T_{-1} from the second equation, etc., until by successive substitution the last equation contains only one unknown T_{n-1} which is then known. The other unknowns are found by back-substitution. This method is especially efficient as the coefficients of the above equations do not change from one time row to the next, and need only be calculated once for a given solution.

In this homogeneous model a constant value for the specific heat c of 0.2 cal/gm°K is used throughout. The Solar constant used is 1.95 cal/cm^2/min (Thekalkara, 1969). A density of 3.0 gm/cm^3 is employed for values of $\gamma < 100$ and a density of 1.5 gm/cm^3 is used for $\gamma \geq 100$, values consistent with the results of Surveyor and Apollo 11 and 12 (Phinney, 1969; Pet (1), 1969). When rock-dust combinations are considered, a value of $\gamma = 20$ is used for rock ($K=4.17 \times 10^{-3}$ cal/cm/sec/k°) (Roelof, 1967) and a value of $\gamma = 1040$ for dust (section 2.B). The program employs c.g.s. units throughout.

The typical computing time for the model on the University of Minnesota's CDC 6600 is three seconds per diurnal period. The homogeneous model described here is used to obtain cooling curves in all of the succeeding chapters. Chapter II applies the model to the Moon, Chapter III to Mercury, and Chapter IV to Mars, Ceres, Vesta, the Jovian Satellites, Titan and Triton. A copy of the main program is found in Appendix A.

Chapter II - The Homogeneous Model Applied to the Moon.

2.A - General Considerations.

The homogeneous model is applied to the Moon to obtain diurnal, eclipse, and integral cooling curves of the flat and cratered lunar surface. These results are then compared with the available observational infrared data to determine the surface value of Gamma and the percentage of surface rock where possible.

The Moon is undoubtedly the best studied object in astronomy. A great deal is known about its orbital and physical surface properties through both remote and in situ observations, and no attempt will be made to summarize this wealth of material. Unless otherwise noted all orbital parameters and the like are taken from Allen (1963) throughout this thesis. The eccentricity of the lunar orbit is 0.0549 while that of the Earth's orbit is 0.0168. The variation in distance from the Sun is mainly due to the Earth's orbit, ranging from 0.981 AU at perihelion to 1.019 AU at aphelion. In comparison, the mean distance from the Earth to the Moon is 0.00257 AU. The rotation of the Moon is direct with a diurnal period of 29.54 days and is inclined 83.2° to the orbit plane which in turn is inclined 5.2° to the ecliptic.

The variation of the sub-Solar point surface temperature due to the above motion is from 397°K at perihelion to 391°K at aphelion. The model solutions are made only for mean distance of 1 AU for a Moon rotating at a constant rate with its spin axis perpendicular to the ecliptic. Daytime measurements should be corrected back to mean distance to avoid the above 6°K variation. The effect of the variation on the integral and nightside temperatures is negligible. As the Moon is not a constant rotator with a perpendicular spin axis, optical librations occur with the movement of a point on the surface of the Moon up to a maximum of ± 7.6° in selenographic longitude and ± 6.7° in latitude. These effects again may be neglected in the integral case and at night. For point measurements during the day one is advised to transform by the proper rotations from the selenographic coordinate system (SLAT, SLONG) to the coordinate system centered on the selenographic sub-Solar position at the time of interest (SSLAT,SSLONG). This is the frame most closely corresponding to that of the model. All references to longitude or latitude in the figures refer to SSLONG and SSLAT. If this is done an error of less than 0.5°K results since the daytime surface is nearly in equilibrium with the incoming solar flux; the error results from a smearing of the actual sub-lunian temperatures by the above ± 7° as compared to the temperatures with depth used by the model. As will be seen in section 2.E, during the day one is often better off simply using the equilibrium black body temperature of the sunlit surface. It should be noted that a proper transformation may also be necessary making use of the optical librations and the lunar axis position angle in converting from the apparent selenographic longitude and latitude as seen by an observer positioned on the Earth (ASLAT, ASLONG) to obtain SLAT, SLONG and then perhaps SSLAT, SSLONG if the selenographic coordinates of the observed position are not a known crater, etc., on the surface. Henceforth all three of the above coordinate systems will be referred to by their mnemonics above.

The step sizes chosen for all lunar solutions are,

$$\Delta t = \frac{\text{diurnal period}}{360} = 118 \text{ minutes}$$

$$\Delta x = 0.05 \text{ (thermal wavelength)}.$$

For a range of step sizes around the above, after carrying the solution through four lunations to equilibrium, a finer grid results in solution convergence <0.1°K at night and <1°K during the day. A larger grid results in these values being exceeded. Convergence is with respect to test solutions carried through ten lunations.

2.B - Lunation Cooling Curves.

The insolation is computed as follows in time:

$$S = \text{Solar Constant}\ \cos(\text{SSLAT})\underbrace{\cos\left(\text{SSLONG}+\frac{2\pi}{\text{diurnal period}}t\right)}_{\text{instantaneous Sun angle, SA}} \tag{2.1}$$

for $\pi/2 < SA > 3\pi/2$

$S = 0$ for $\pi/2 \geq SA \leq 3\pi/2$

t = time, reckoned from noon of SSLONG = 0°.

Lunation cooling curves are obtained for the values of Gamma and SSLAT listed in Table 2.1.

Table 2.1

Gamma	15, 20, 25, 30, 35, 600, 800, 1000, 1200, 1400
SSLAT	0, 20, 40, 60, 80

These values of Gamma are chosen to encompass those likely to exist on the lunar surface for rock and dust. SSLAT is chosen to obtain a grid from which the surface temperature may be interpolated to better than 0.1°K for any SSLAT. Table 2.2 presents the thermal wavelengths, λ, associated with the above values of Gamma where the specific heat is 0.2 cal/gm°K and the density 3 gm/cm^3 for rock and 1.5 for dust in the calculation as explained in equation (1.14) and section 1.D.

Table 2.2

Gamma	15	20	25	30	35	600	800	1000	1200	1400
λ(cm)	100.13	75.10	60.08	50.07	42.91	5.01	3.75	3.00	2.50	2.15

Table 2.3 describes the lunation cooling curves included in this thesis.

Table 2.3

Figure	Description of contents
2.1	Gamma = 1000, SSLAT = 0, 6 depths
2.2	Gamma = 20, SSLAT = 0, 6 depths
2.3	All Gamma, SSLAT = 0
2.4	All Gamma, SSLAT = 20
2.5	All Gamma, SSLAT = 40
2.6	All Gamma, SSLAT = 60
2.7	All Gamma, SSLAT = 80

Inspection of these figures show them to be consistent with what one would expect given the homogeneous model described in Chapter I. Figures 2.1 and 2.2 show the proper phase and amplitude change with depth in agreement with the harmonic solution, equation (1.14). The phase lag of maximum amplitude at minimum Sun angle increases as Gamma decreases. The bottom temperature (the temperature at five thermal wavelengths depth) increases as the thermal inertia increases, and decreases with latitude where the Solar radiation becomes less. The variations of this constant bottom temperature with Gamma and SSLAT are tabulated in table 2.4.

Table 2.4

Lunar Bottom Temperatures °K

	SSLAT				
Gamma	0°	20°	40°	60°	80°
15	282	279	267	244	198
20	278	276	263	241	195
25	275	271	260	238	192
30	272	268	257	236	190
35	270	266	255	234	188
600	226	225	214	196	158
800	223	220	211	193	155
1000	220	217	208	191	153
1200	218	215	206	189	152
1400	216	214	205	187	150

Comparison of these curves with the 11.6μ and 21μ data obtained by David Allen (1970a, p. 39) on limb scans of the nighttime lunar surface gives a best fit to Gamma = 1040 $\pm$ 25 for the 21μ data and a Gamma = 800 $\pm$ 25 for the 11.5μ data. Tables 2.5-2.7 show the measured and computed temperatures in each case.

These values of Gamma also agree with the 11μ data of Wildey, Murray and Westphal (1967) and the 22μ predawn value of Low (1965) as seen in figure 2.8.

Table 2.5

Comparison of David Allen's January 10, 1969 (5.5 days cooling from sunset) 21μ Cold Limb Scan Data with Model - Best Fit Gamma = 1030 ± 25.

Temp°K SSLAT	Data	γ=800	γ=1000	γ=1200
0	103	109	103	99
20	102	108	103	99
40	101	107	101	97
60	97	103	98	94

Table 2.6

Comparison of David Allen's March 21, 1969 (4.3 days cooling from sunset) 21μ Cold Limb Scan Data with Model Best Fit Gamma = 1050 ± 25.

Temp°K SSLAT	Data	γ=800	γ=1000	γ=1200
40	103	109	104	100
60	100	106	100	96
80	89	97	92	88

Table 2.7

Comparison of David Allen's March 16, 1970 (9.0 days cooling from sunset) 11.6μ Cold Limb Scan Data with Model - Best Fit Gamma = 800 ± 25.

Temp°K / SSLAT	Data	γ=800	γ=1000	γ=1200
0	103	102	97	93
20	101	101	96	92
40	99	100	95	91

If this difference in Gamma of 240 is taken to be due to rocks on the lunar surface, and if one assumes that the 21μ data represents the dust component with a negligible contribution from rock, one then obtains the following fractions for rock of Gamma = 20 that must be present in order to depress Gamma to 800 at 12μ throughout the night.

$$\text{(2.2)} \qquad \%\ \text{rock} = \frac{F_{800} - F_{1040}}{F_{20} - F_{1040}} \times 100$$

where

$$\text{(2.3)} \qquad F_x = \frac{C_1}{\lambda^5 \left(e^{\frac{C_2}{\lambda T_x}} - 1\right)}$$

Table 2.8

Fraction of Rock on Lunar Surface

Days cooling from sunset	1	2	4	6	8	10	12	14
Percent rock on surface	0.41	0.28	0.17	0.12	0.09	0.08	0.06	0.06

It is clear from table 2.8 that a decreasing fraction of rock is needed to depress a Gamma = 1040 surface to Gamma = 800 at 12μ. This is in agreement with the picture of smaller rocks being thermally clamped by their surrounding dust as the night wears on, leaving only rocks larger than their thermal wavelength (roughly greater than one meter) toward the end of the night. However, there is no apriori reason why the lunar surface rock distribution should conform solely to a Gamma = 800 surface at 12μ throughout the night, and more data is needed to confirm and help clarify this point. David Allen (1970a, p. 47) estimates that 0.15% by area of large boulders or rock, as it is thought of in this thesis, should contribute thermally by night given typical boulder size distributions on the lunar surface.

2.C. - The Crater Model.

A simple model of a lunar crater is developed to determine how homogeneous solutions compare with the data taken at 11.6μ by Allen and Ney (1969) of three major creaters given the rock hypothesis. Again, neither depth and temperature-dependent thermal parameters, roughness, nor the three-dimensionality of individual rocks are considered. A twelve-sided crater, with 20° sloping walls of rock (Gamma = 20) and a floor of dust (Gamma = 1040) is employed. The crater is also taken to be of such a size that shadowing and re-radiation may be neglected.

This model is physically unrealistic in that it assumes the hot regions (the rock) to be on the crater rim (measurements indicate that the hot regions pervade the entire crater region and are not limited to the rim), but nevertheless should give an indication of the amount of rock involved insofar as the homogeneous model applies. Since the beam size, 26 arc sec, used to make the measurements is smaller or nearly the same size as the craters considered, the normal projected area of each side and the floor of the above model is taken to just fill the beam, and is used to determine the crater percentage rock. The fact that the measurements are not made necessarily at normal incidence is not of consequence here due to the diffuse nature of the hot regions in and around the crater. It is desired to see how the percentage rock determined from the above model and a 12μ brightness temperature agrees with the fraction of enhanced crater area radiation determined independently from the flux measurements with color of Allen and Ney (1969).

The model is run and compared to the data at 12μ for the following three craters.

Table 2.9

NAME	SLAT	SLONG	DIAMETER
Tycho	-45.9	-15.85	77km
Copernicus	6.90	-18.22	90km
Aristarchus	19.28	-46.24	34km

(Mills and Sudbary, 1968; Alter, 1968, p. 343)

For each of these craters, twelve determinations, one for each rock face, and one for the dust floor are made using the homogeneous model over a lunation from local noon to local noon. Four lunations are used to relax the solution in each case. The incident Sun angle (SA_n, $n = 1,2,\ldots\ldots 12$) for each rock face is given by:

(2.4) $$SA_n = \cos(L_1)\cos\left(SLONG + L_2 + \frac{2\pi}{\text{diurnal period}}\,t\right)$$

where,

$$L_1 = \sin^{-1} \sin(SLAT)\cos(20°) + \cos(SLAT)\sin(20°)\cos(\theta)$$

$$L_2 = \sin^{-1} \frac{\sin(\theta)\sin(20°)}{\cos(L_1)}$$

$$\theta = 30°(n-1),\ n = 1,2\ldots\ldots\ldots 12.$$

The incident Sun angle for the dust floor is simply:

(2.5) $$SA_f = \cos(SLAT)\cos\left(SLONG + \frac{2\pi}{\text{diurnal period}}\,t\right).$$

Following the thirteen homogeneous solutions of each crater, the 11.6μ flux is determined for the thirteen areas involved at each point in time by means of equation (2.3). The fluxes are next multiplied by the proper fraction of normal projected area and summed. The fractions, x, of normal projected rock face used are:

x=0.00,0.01,0.011,0.02,0.03,0.05,0.06,0.075,0.10,0.15,0.20.

The resultant integral flux is then converted back to an equivalent 11.6 μ brightness temperature by using the inverse of equation (2.3). The internal accuracy of the solution is ± .1°K, and that of the data is ± 1.0°K.

The results are plotted in figures 2.9-2.11. In comparing the data with the model one notes that the percentage rock falls off with cooling from sunset in the cases of Tycho and Copernicus. This is in agreement with the results found by Allen and Ney (1969), and is attributed to the progressive cooling of rocks with less than one meter diameter. It is further noted that all the craters fit the data well after 4.5 days cooling, where it may be concluded that only large rocks contribute. Also, surprisingly, the model fits the data for Aristarchus with 2.0% rock throughout the night. It is concluded from this that Aristarchus contains only large rocks. A comparison of the percentage rock found in this study and by the multi-color analysis by Allen and Ney (1969) is found in the following table 2.10

Table 2.10

Crater	Model	Allen and Ney
Tycho	10.0%(2.5 days)	10.0%(2.5 days)
	6.0%(9.7 days)	3.5%(9.7 days)
Copernicus	3.0%(1.7 days)	8.0%(1.7 days)
	1.1%(8.9 days)	2.0%(8.9 days)
Aristarchus	2.0%(1.0 days)	-----
	2.0%(6.9 days)	3.0%(6.9 days)

days = days cooling from sunset

The above figures are also in general agreement with studies of Lunar Orbiter Photographs of these craters made by David Allen (1970a, p. 98).

The close agreement between the three above methods of determining percentage rock of the lunar surface gives strong support to the thesis that rocks are the primary cause of the anomalously hot readings obtained from these craters. A more detailed model must necessarily consider the size distribution and three dimensional radiational properties of rocks in and around craters. As Allen and Ney did not obtain a percentage rock value for Aristarchus early in the night, the present result of a lack of small rocks cannot be compared. Further lunation measurements are needed to confirm or deny this tentative result. Also these craters need be measured throughout an eclipse at as many wavelengths as possible, where if the rock theory is correct, even smaller rocks, thus increased percentage rock, should come into play.

2.D - The Moon in Eclipse.

The circumstances of a lunar eclipse are not unlike those for a lunation from a computational point of view given the homogeneous model. However, here the solution is non-periodic, having a duration of only a few hours, and the insolation function is substantially more complex, varying significantly with position on the lunar surface. The reduced time scale means that only the upper few millimeters of surface are involved. To obtain an understanding of the circumstances surrounding a lunar eclipse one is referred to Kopal (1962) and Link (1969).

Many of the parameters of an eclipse may be obtained from The American Ephemeris and Nautical Almanac; these are listed in table 2.11. The remainder follow from a consideration of what an observer located at the point of interest on the lunar surface experiences as the Sun passes behind the Earth. The sizes of the two disks, the velocity with which their centers move, and the distance of closest approach are found in this way. From this information in turn is calculated the penumbral and umbral durations which lead to the proper time and depth steps, and the circumstances of insolation for the given location. A detailed description follows.

$\phi_\odot$, $\delta_\odot$ = right ascension, declination of Sun

$\phi_{\leftmoon}$, $\delta_{\leftmoon}$ = right ascension, declination of Moon

$\Delta\delta_\odot, \Delta\delta_\odot$ = hourly motions of Sun

$\Delta\delta_{\leftmoon}, \Delta\delta_{\leftmoon}$ = hourly motions of Moon

$HP_\odot$ = horizontal parallax of Sun

$HP_{\leftmoon}$ = horizontal parallax of Moon

$R_\odot$ = semi-diameter, radius, of Sun

$R_{\leftmoon}$ = semi-diameter, radius, of Moon

R_1 = Sun-earth distance

R_2 = Earth-moon distance

t = the various times associated with the occurrence

From a consideration of a translation, from an Earth centered coordinate system to a lunar centered coordinate system, one finds that angular distances in general transform as:

$$\alpha' = \frac{\alpha}{(1 + \frac{R_2}{R_1}} \tag{2.5}$$

All angles in the following equations are considered to be in units of arc. The lunar centered system is considered the primed (') system. The radius of the Sun, $R'_\odot$, as seen from the Moon is found in terms of the semi-diameter of the Sun, $R_\odot$, as seen from Earth:

$$(2.6) \qquad R'_\odot = \frac{R_\odot}{(1 + \frac{R_2}{R_1}}$$

$R'_\odot$ is used as the standard of length in determing the following parameters.

The angular motion of the Moon, M, with respect to the shadow center in the Earth frame (where the shadow has coordinates $\psi_\odot + 180°$, $- \delta_\odot$ and hourly motion $\Delta\phi_\odot$, $-\Delta\delta_\odot$) is:

$$(2.7) \quad M = \sqrt{[(\Delta\phi_\odot - \Delta\phi_☾)\cos \delta_☾]^2 + [\Delta\delta_☾ + \Delta\delta_\odot]^2}.$$

The inclination, i, of this motion with respect to an East-West axis is,

$$(2.8) \quad i = \tan^{-1} [\frac{\Delta\delta_☾ + \Delta\delta_\odot}{\cos \delta_☾ (\Delta\phi_\odot - \Delta\phi_☾)}$$

Making use of the above translation, the motion of the Sun relative to the Earth, M' in terms of Sun radii, $R'_\odot$, as seen from the Moon is:

$$(2.9) \qquad M' = M/R_\odot$$

The radius of the Earth in terms of $R'_{\odot}$ as seen from the primed system is,

$$(2.10) \qquad R'_{\oplus} = HP_{☾}/R'_{\odot}$$

In determining the insolation the detailed effects due to the Earth's atmosphere are neglected, and it is deemed sufficient to simply increase by 2.3% the radius of the Earth as has been determined by experiment from measurements of the umbral shadow to be the increase necessary due to the Earth's atmosphere (Link 1969, p. 104).

$$(2.11) \qquad R'_{\oplus} = R'_{\oplus}1.023$$

To obtain the distance of closest approach of the two disks for an observer at the position x on the lunar surface it is needed to transform the selenographic coordinates (SLAT,SLONG) to the apparent selenographic coordinates of x (ASLAT,ASLONG)as determined from the projected celestial system centered on the Moon. This is accomplished by rotations by ψ, the lunar axis position angle, and the optical librations. One thus obtains a $\Delta\phi_x,\Delta\delta_x$ of the point of interest with respect to the apparent center of the Moon. At the time of opposition for the position x,

$$(2.12) \qquad \phi_{\odot} + 12 \text{ hours} = \phi + \Delta\phi_x ,$$

the angle π between the center of the shadow and x in declination is found,

$$\pi = \delta_{☾} + \delta_{\odot} + \Delta\delta_x \tag{2.13}$$

The arc ω of closest approach as seen from the Earth is then

$$\omega = \pi \cos i \tag{2.14}$$

Transforming this as before to the minimum distance D' between the Earth and the Sun as seen from the position x at closest approach in terms of R' gives the desired result:

$$D' = \omega/R_{\odot} \tag{2.15}$$

The time T_x at which first contact takes place for the point of interest on the Moon is easily determined from the times given in the Ephemeris and a consideration of how the penumbral shadow sweeps across the lunar surface. This time need only be determined to ± 10 minutes to adequately determine the pre-eclipse surface temperature for the point x. Here the program is also given the sub-Solar-selenographic coordinates, SSLAT, SSLONG of the point of interest.

Next the manner in which the disk of the Sun is covered behind that of the Earth is determined. This event is depected in figure 2.12. The horizontal distance parallel to the relative motion between the centers at first contact is:

$$DF' = [(1 + R'_{\oplus})^2 - (D')^2]^{1/2} \tag{2.16}$$

The actual distance between centers with time is then:

$$DT' = [(DF' - M't)^2 + (D')^2]^{1/2} \tag{2.17}$$

The time duration Δt from first to fourth contact then becomes:

$$\Delta t_{1-4} = \frac{2DF'}{M'} \tag{2.18}$$

The model takes Δt_{1-4} as an effective period in determining the depth and time steps. Taking limb darkening into account (Allen 1963, p. 169) the fraction f of the total solar flux incident on the surface is then:

$$f = 1 \text{ if } DT' < (1 + R'_{\oplus})$$

$$f = 0 \text{ if } R'_{\oplus} < (1 + DT')$$

otherwise,

$$f = \frac{2}{\pi} \int_{\odot}^{1} LD(r) \; (\pi - \phi(r)) \; dt \tag{2.19}$$

where

$$\theta = \sin^{-1}(r)$$

$$LD(\theta) = (1.0-U-V+U\cos(\theta)+V\cos^2\theta)/(1-U/3-V/2)$$

$$U = 0.84$$

$$V = -0.20$$

$$\phi = 0 \text{ if } DT' < (r + R'_{\oplus})$$

$$\phi = \pi \text{ if } R'_{\oplus} < (r + DT'), \text{ otherwise}$$

$$\phi = \cos^{-1}\left[(r^2+(DT')^2-(R'_{\oplus})^2)/2rDT'\right]$$

The insolation S_E then becomes $S_E = Sf$ where S is described by equation (2.1)

In this way the needed eclipse parameters are found.

Consistent with the previous section on lunations, in the eclipse case (it is noted that the above solutions are valid for a penumbral and partial as well as total eclipse), the solution for the given point of interest x and desired Gamma is taken through four lunations and halted at the proper diurnal phase angle, that is time T_x at which first contact takes place. The program then switches into its eclipse mode where the above parameters are made use of, continuing the solution for Δt_{1-4} + 30 minutes, with the newly determined time and depth steps. The added time is to allow the surface to cool back to its pre-eclipse value.

As noted in the introduction this portion of the program was originally written in 1968 for the two eclipses of that year which were both clouded out in the infrared at the O'Brien Observatory. Since that time there have been two useful partial eclipses only. David Allen obtained some data on the first one during the night of February 21, 1970. The second one took place on August 17, 1970 but was too low in the sky in Minnesota to cope with the cirrus about on that night (-20° in declination and 3 hours over). Preparations were also made for the total eclipse of February 10, 1971, but again clouds.

The only useful eclipse data obtained at the O'Brien Observatory since 1968 is that obtained during the partial eclipse of February 21, 1970 (Allen 1970a, p. 46). But even here due to a heavy frost and ice on the mirror, only the measurements coming out of eclipse proved useful for comparison with the homogeneous model. The measurements were taken close to the South pole of the Moon (SSLAT = -80°, SSLONG = -11°) in a region lacking previous eclipse anomalies. In this region, the umbral phase lasted 40 minutes. The computed circumstances of this eclipse are given in table 2.12. Figure 2.13 depicts a comparison of the measurements with the homogeneous model at 12 microns.

It is evident that the early penumbral data agree closely with a surface Gamma = 1400, and that the late penumbral period behaves as Gamma = 1000. Here the model used a step size of 0.78 minutes, and the thermal wavelength was 0.31 cm for Gamma = 800, 0.24 cm for Gamma = 1000, 0.20 cm for Gamma = 1200, and 0.17 cm for Gamma = 1400, with the depth step again being 0.05 thermal wavelength. The data was not extended beyond that shown due to high extinction so comparison cannot be made for the final stage of warming back to the pre-eclipse temperature of 250°K. The high value of Gamma = 1400 during the umbral and early penumbral phase, as opposed to Gamma = 800 obtained at 12 microns during the lunar night is undoubtedly due to the changing bulk modulus of the near surface, and a particulate, thermophysical model of the lunar soil like that of Winter and Saari (1969) is needed to obtain agreement between the Eclipse and Lunation case. However, rocks on the surface, the evidence of which it is seen is strong, must also account for the observed change in Gamma throughout the eclipse. The 3% rock found from a color analysis of this eclipse by Allen (1970a, p. 47) remaining essentially at its pre-eclipse temperature of 250°K as one would expect from its high thermal inertia, necessarily means that the actual dust, measured to be 130°K, must have possessed a Gamma higher than 1400 so that the composite solution with rock could be lowered to 1400 at 12μ. In fact 3% rock at 250°K maintains a temperature of 145°K alone for the duration of the umbral period. The model gives 149°K at the end of totality at Gamma = 1400. The data upon which this argument rests is too uncertain to warrant further analysis. Clearly more multi-wavelength data and a detailed thermophysical model including the wide distribution of surface rocks are needed to clarify the above comments.

In preparation for the eclipse of February 10, 1971 which had a magnitude 1.313 one test run has been made at Gamma = 800, 1000, 1200, 1400 for SSLAT = SSLONG = 0. Here a step size of 1.63 minutes was used, and the thermal wavelength was 0.44 cm for Gamma = 800, 0.35 cm for Gamma = 1000, 0.29 cm for Gamma = 1200, and 0.25 cm for Gamma = 1400. The computed parameters of this eclipse are listed in table 2.13, and the cooling curves appear in figure 2.14. They are included here as an example of the typical behavior of the lunar surface during a full eclipse.

Table 2.12

Computed Partial Eclipse Parameters for February 21,1970

Solar selenographic latitude of x	$SSLAT_x$	-80.0°
Solar selenographic longitude of x	$SSLONG_x$	-11.0°
Motion of the Sun in primed system	M'	1.767 $R'_\odot$/hr
Radius of the Earth in primed system	$R'_\oplus$	3.413 $R'_\odot$
Distance of closest approach seen from x	D'_x	2.392 $R'_\odot$
Duration first to fourth contact seen from x	Δt_x	4.197 hr
Time of first contact at x	T_x	6^h13^m UT

Table 2.13

Computed Total Eclipse Parameters for February 10,1971

Solar selenographic latitude of x	$SSLAT_x$	0.0
Solar selenographic longitude of x	$SSLONG_x$	0.0°
Motion of the Sun in primed system	M'	1.699 $R'_{\odot}$/hr.
Radius of the Earth in primed system	$R'_{\oplus}$	3.363 $R'_{\odot}$
Distance of closest approach seen from x	D'_x	0.919 $R'_{\odot}$
Duration first to fourth contact seen from x	Δt_x	5.021 hr
Time of first contact at x	T_x	5^h16^m UT

2.E - The Integral Temperature of the Moon.

In anticipation of integral measurements to be made on the Moon by Thomas Murdock for the purpose of intercomparing the integral fluxes of the Moon and Mercury with phase to ascertain surface roughness, the results of section 2.B are here integrated over the visible hemisphere for the total, bright side, and dark side integral brightness temperature with phase in the manner described in section 3.C. A 20° grid over the surface is employed.

For the day side integral temperatures, the results for Gamma = 1000 are used. The exact Gamma and contribution of rocks on the surface is not important here as the diurnal period of the Moon is such that the sunlit surface is close to the equilibrium temperature, within 1°K for the model except for large phase where small differences between waxing and waning appear as seen in figure 2.15. Here the 3.5 micron and 12 micron integral, day side brightness temperatures are plotted as a function of phase. Also, in general, the 8.5 micron curve is 1°K above the 12 micron curve, and the 20 micron curve 1°K below. The curves become inaccurate for high phase where the integral is weakest, and where the influence of rocks can no longer be ignored.

The integral dark side 'color' temperature also explained in section 3.C is tabulated in table 2.14 as a function of Gamma. The integral 'color' temperature obtained by combining various fractions of Gamma=20 and Gamma=1000 material appear in table 2.15. It will be of interest to see how the integral measurements compare with the previous lunation result of 0.15% rock and the eclipse result of 3.0% rock, although variations with cooling time and the like are lost in the integral

Table 2.14

Lunar Integral Dark Side Color Temperature(°K)With Gamma

Gamma	15	20	25	30	35	600	800	1000	1200	1400
Temp	234	224	216	209	203	113	106	101	97	94

Table 2.15

Lunar Integral Dark Side Color Temperature(°K)With Rock-Dust Fraction

%Rock	0.1	0.2	0.3	0.5	1.0	2.0	3.0	4.0	5.0
Temp	102	102	103	104	105	111	115	119	122

Chapter III - The Homogeneous Model Applied to Mercury.

3.A - General Considerations.

The homogeneous model is applied to the planet Mercury to obtain both diurnal cooling curves, and integral hemispherical brightness and color temperatures for all phases and a variety of Gamma. These results are then compared with the available observational infrared data (more properly datum in this case) to determine the mean surface value of Gamma and the percentage of rock on the surface.

Mercury is the nearest planet to the Sun, and thus subject to the highest insolation. The planet is in an elliptical orbit with an eccentricity of 0.2056, having a perihelion distance of 0.3075 AU and an aphelion distance of 0.4667 AU. Mercury's rotational period is coupled to its orbit period in the ratio 2/3. This coupling results in a diurnal period that is twice the orbit period of 88 days, or 187 days long (Dyce et al., 1967; Carmichel and Dolfus, 1968). Observations show the rotation to be direct with the axis perpendicular to the orbit plane which is inclined 7° to the ecliptic. Faint surface features are barely observable on the disk, the diameter of which is 6.7 arc sec at 1 AU. As a result very little is known about the surface of the planet, and only integral fluxes may be observed.

However, the visual albedo, phase curves, and polarization are remarkably similar to the moon, and from this it may be surmised that the surface characteristics are also similar. The very slight atmosphere of approximately 3 gm/cm^2 that may or may not exist around the planet (Moroz 1967, p. 81) certainly is transparent at infrared wavelengths. It is then quite clear that we receive thermal emission from Mercury, making it a prime candidate to compare with this homogeneous model. Although its actual Bond emissivity is 0.94, a value of 0.93 is used to minimize the number of parameters changed from the lunar case. The infrared emissivity is also set at 0.93. The planetocentric coordinates used set MLAT = MLONG = 0 as the subsolar point at perihelion, with MLONG increasing in a clockwise fashion.

The ellipticity of the orbit results in a 'sundance' for an observer situated on Mercury's surface. The Sun traverses the sky at a variable rate. An observer at MLONG = 0° sees retrograde motion when the Sun is at zenith, while at the same time an observer at MLONG = 270° sees two successive sunsets due to the same motion (Soter and Ulrichs, 1967). The variation of the subsolar temperature for these two locations is from 710°K to 512°K. The severity of this variation necessitates its inclusion in any calculation of the surface thermal history, even during the night.

Fortunately a given point on the surface experiences the same insolation from one diurnal period to the next, making it possible to tie the solutions to the planetocentric coordinate system. The insolation at MLONG = ψ is furthermore equal to that of $\phi + 180°$, also reducing the number of solutions necessary.

3.B - Diurnal Cooling Curves.

The following equations are employed to obtain the insolation at the surface S:

$$(3.1) \quad S = \frac{\text{solar constant} \cos(\text{MLAT})}{R^2} \cos(\eta-\phi-\text{MLONG})$$

where

ψ = solar angle from perihelion

$= (2e-1/4\ e^3)\sin(\varepsilon)+(5/4e^2-11/24\ e^4)\sin(2\varepsilon)$
$\quad + 13/12\ e^3\sin(3\varepsilon)+103/96\ e^4\sin(4\varepsilon) + \varepsilon$

$\eta = 2\pi$(time from perihelion)/spin period

$\varepsilon = 2\pi$(time from perihelion)/orbit period

e = eccentricity

a = semi-major axis

$R = a(1-e^2)/(1+e\cos(\psi))$

Trial solutions showed that a time step size,

$$\Delta t = \frac{\text{diurnal period}}{720} = 352 \text{ minutes;}$$

was needed to properly handle the extreme temperature variation that occurs on the surface of Mercury. This time step is one half that used on the Moon. The depth step remained the same as before at $\Delta x = 0.05$ (thermal wavelength). Also each solution was carried through four diurnal periods where it was determined that the solution varied by $<\pm 1°K$ from the solution carred to ten diurnal periods at any point in the period.

Using the above parameters and the homogeneous model, diurnal cooling curves were obtained for the cases listed in Table 3.1 for a range in Gamma consistent with the idea of a surface comprised of a mixture of rock and dust in anticipation of their use in determining the integral surface temperatures described in section 3.C. Table 3.2 lists the associated thermal wavelengths.

Table 3.1

Mercurian Cooling Curves Calculated

Gamma	15	20	25	30	35	500	600	800	1000	1200
MLONG	0	20	40	60	80	100	120	140	160	
MLAT	0	20	40	60	80					

Table 3.2

Associated Thermal Wavelengths λ

Gamma	15	20	25	30	35	500	600	800	1000	1200
λ(cm)	244	183	147	122	105	14.7	12.2	9.2	7.3	6.1

As it would take a minimum of 45 plots containing 11 graphs each to depict all the data prepared for the integral solutions, only a representative sample described in table 3.3 is included in this thesis. The complete data are available on magnetic tape.

Table 3.3

Description of Mercurian Cooling Curves

Figure	Description
3.1	All Gamma, MLAT = 0, MLONG = 0
3.2	All Gamma, MLAT = 0, MLONG = 100
3.3	All MLAT, MLONG=0, Gamma=600
3.4	All MLAT, MLONG=100, Gamma=600

Figures 3.1 - 3.4 speak for themselves, showing the wide temperature fluctuations found on the surface of Mercury, and give an idea of how the particular insolation affects the surface temperature. Table 3.4 gives Mercury's bottom temperature as a function of Gamma and longitude for MLAT = 0. Table 3.5 does the same for MLAT = 40.

Table 3.4
Mercury Bottom Temperatures [°K] For Latitude 0°

Gamma	0	20	40	60	80	100	120	140	160
20	409	406	397	382	356	355	383	398	407
500	347	345	337	323	299	298	323	338	345
600	345	342	335	320	297	296	321	335	343
800	341	339	331	317	293	293	317	331	339
1000	338	336	329	314	291	290	315	329	337
1200	336	334	327	312	289	288	313	327	335

Table 3.5
Mercury Bottom Temperatures [°K] for Latitude 40°

Gamma	0	20	40	60	80	100	120	140	160
20	387	384	376	362	337	336	363	377	385
500	327	325	318	305	282	282	305	318	326
600	325	323	316	302	280	279	303	316	323
800	321	319	312	299	276	276	299	312	320
1000	319	317	310	296	274	274	297	310	317
1200	317	315	308	294	272	272	294	308	315

3.C - Integral Temperatures of Mercury.

The main focus of this chapter is the compilation of integral, hemispherical temperatures from the homogeneous model to compare with the infrared data available for Mercury. To this end a 20° x 20° grid is established over the entire planet, and a diurnal cooling curve is obtained at each point as described in section 3.B. Making use of the existing symmetries in longitude and latitude this involves 45 cooling curve solutions for each Gamma as listed in table 3.1. The following integral form is then evaluated numerically over the hemisphere visible from Earth to obtain the total, day side, and dark side flux $TF_\lambda(t)$, coming from the geometrically visible hemisphere for a given phase, wavelength λ, and time t reckoned from perihelion.

$$(3.2)\quad TF_\lambda(t) = 2\int_0^{90°} d\theta \int_{\substack{\text{sub-Earth MLONG}-90°,\ \text{sunset}\\ \text{MLONG, sunrise MLONG}}}^{\substack{\text{sub-Earth MLONG }+90°,\ \text{bright}\\ \text{limb, dark limb}}} d\phi\, F_\lambda(T(\theta,\phi,t))\cos\phi\,\cos^2\theta$$

where, λ = 3.8, 8.5, 12, 20 microns.

$T(\theta,\phi,t)$ = homogeneous model temperature for t at

MLAT = θ; MLONG = ϕ.

$F_\lambda(T)$ = black body brightness flux using equation 2.3.

The proper apparent brightness integral temperatures are then derived from $TF_\lambda(t)$'s making use of the inverse of equation 2.3 after dividing by the correct areas.

The above integral assumes that the sub-Earth point is always on the Mercurian equator, where in fact Mercury's orbit is inclined some 7° to the ecliptic which allows the sub-Earth point to wander to extremes of + 16° in MLAT. Such extremes only occur when superior or inferior conjunction coincide with aphelion or perihelion. In the superior conjunction case the variation is only $\pm$ 5° in MLAT while it will be seen from figure 3.5 that the integral solution is flat over a wider range of phase than this. This variation may then be neglected. The possible variation of $\pm$ 16° results in an ever present crescent at inferior conjunction, and reliable nighttime data is simply not obtained when this crescent is larger than a few degrees in phase. Thus this problem is to a large degree avoided, and further lessened by subtracting out the effect of the small crescent when the data is reduced to an integral nightside temperature. From the point of view of the model, the dark side integral temperature is found to be flat for $\pm$ 10° either side of phase = 180. Thus it is felt that neglect of the inclination of Mercury's orbit produces an error of <0.5°K to the computed integral temperatures at any given time.

In performing the integration, the 45 grid point diurnal solutions spaced 20° apart for a given Gamma are used. A second degree interpolation is then performed on the diurnal solution at each grid point to determine $T(t,\psi,\theta)$ for the desired time from perihelion t. For a given Gamma and t this has only to be done once. The integral of equation (3.2) is then evaluated making use of the above preset grid. To obtain $T(t,\psi,\theta)$ at any step in the integration, the grid point closest to the desired $MLAT_x$, $MLONG_x$ is first found. Next the eight grid points surrounding this one are also determined. Then a second degree interpolation is made at each grid latitude in longitude for the desired $MLONG_x$. A fourth second degree interpolation is then performed in latitude using these three interpolated values for the desired $MLAT_x$ to obtain the needed temperature. For MLAT> 80° an extrapolation is used with the MLAT 40°, 60° and 80° grid points. It is felt that this more nearly approximates the surface temperature at high latitudes where surface roughness plays an important part. Special precautions are also made in interpolating in the neighborhood of the sunset, sunrise terminators where the temperature variations are extreme.

The integration is performed at a spacing of 2° in MLAT and MLONG, for which internal convergence is within 0.1°K for a given set of conditions. The integral solution is limited only by the 20° grid, and the homogeneous model itself. A finer grid in latitude is not necessary. It is found that a finer grid in longitude is necessary for a detailed study of the region $< \pm 10°$ in longitude of the sunset or sunrise terminator as will be seen. Such fine grids are expensive in computer time and not justified using the homogeneous model as the three dimensionality and size distribution of rocks, especially near the limb, also play an important role in this region and must be included in any such detailed study. The present model breaks down for day time solutions at a phase greater than 170°, and for night time solutions for phase less than 10°. However, in the case of dark side solutions only phase 180° is included in this thesis as it is not possible to measure integral dark side temperatures at other than this phase and difficult enough in this case. In this way then the program determines the integral day time, dark side, and total flux coming to the Earth for any desired wavelength, phase, time from perihelion, and Gamma.

Finally the integral flux is divided by the proper area. For the integral day time flux this is DA where

$$\text{(3.3)} \qquad DA = \frac{\pi}{2} \ (1 + \cos \text{(phase)}).$$

The corresponding dark side area, NA, is simply: $NA = \pi - DA$, while the total area TA is π. The inverse black body equation, the inverse of equation 2.3, is used to convert back to the desired apparent integral brightness temperature of Mercury.

Figure 3.5 provides the integral, day side, brightness temperature for Gamma = 600 as a function of phase at mean distance (19.22 days from perihelion). Here the 3.8 and 12 micron solutions are plotted. The 8.5 micron solution is approximately 1°K above the 12 micron solution and the 20 micron case one below. It is noted that the variation between the waning and waxing solution is <0.5°K, and further that the solution is identical to better than 0.5°K to the equilibrium black body solution at that distance out to a phase of 160°. The integral equilibrium solution is obtained by substitution of the equilibrium surface black body temperature T_b (ψ,θ) into equation 3.2 where,

$$(3.4) \quad T_b(\phi,\theta) = [\frac{\text{solar constant}}{\sigma\ R^2} \cos\theta \cos\phi]^{1/4}$$

The comparison is made with the emissivity equal to one in the black body equilibrium case, illustrating that plotting the actual surface temperature with $\varepsilon_B = \varepsilon_{IR} = 0.93$ in the model as is done throughout this work and described in section 1.B results in the same surface temperature as the case with $\varepsilon_B = \varepsilon_{IR} = 1$ in the model. As explained in section 1.B, this shows the offsetting effects of ε_B and ε_{IR}. The above comparison is made primarily to check the integral solution. It also shows that if one is dealing with the sunlit portion for phases less than 160° it is perfectly adequate, much simpler, and saves a great deal of computer time, to use the integral black body sunlight equilibrium solution. One also sees that the day side solution is then independent of Gamma given a surface with Gamma = 500 or higher. All this is due to the slow rotation period of 176 days. It is seen in section 2.D that divergence from the equilibrium case starts to appear with the lunar rotation period. In chapter IV large deviations are observed where the rotation period is reduced to hours.

The 3.8 micron data of Thomas Murdock (1970) of the integral brightness day side temperature of Mercury with phase is also plotted. The forward peaking of this data by 50 percent in flux over the present model is apparent, and is a measure of the inability of the present model with its Lambertian surface to adequately cope with the sunlit case. As Murdock shows, this increase is most certainly due to surface roughness which seems to play a more important role on Mercury than on the Moon where the corresponding increase is only 10%. A detailed surface roughness model is needed to further develop this difference.

Now that the model has proved reliable by comparison to the equilibrium case above it is applied to the dark side of Mercury, a region where a simple equilibrium solution does not exist, with some confidence. As the integral solution progresses across the surface in increasing planetocentric longitude from the sunrise terminator on the West limb toward the sunset terminator on the East limb, the integral solutions for 8.5, 12 and 20 microns all stay within 1°K of each other to within 10° of sunset in longitude. At this point first the 8.5 micron integral temperature, followed closely by that at 12 microns, increase anywhere from 5°K to 30°K above the 20 micron integral temperature by the time the solution has reached the sunset terminator. The 20 micron increase is 1°K over this last 10° in longitude. This spread from 5°K to 30°K depends on the time from perihelion at which the solution is being made. If Mercury is in a position in its orbit where its angular rotation is large, the area just coming into view over the sunset terminator is warmer than usual, not having time to cool significantly. It is here the large increases in the integral 8.5 and 12 micron temperatures are observed. If the angular rotation happens to be slow, more cooling of this area has taken place, and the increase is only 5°K.

At this point the method of reducing the one integral measurement that has been made of the Mercurian dark side temperature to date during the inferior conjunction of September 29, 1969, measured by Murdock and Ney (1970), needs to be reviewed. Measurements were made at 3.75, 4.75, 8.6 and 12 microns. The average dark side temperature was found to be 111 ± 3°K, and the crescent 205 ± 3°K. First scattered sunlight was removed, then it was assumed that all 8.6 micron emission was thermal emission from the crescent, and all 12 micron emission was from the dark side. The black body overlap of the resultant two brightness temperatures considered as color temperature was then adjusted by a method of successive approximations to obtain the above two 'color' temperatures for the crescent and dark side.

What this does in effect is to assign any dark side region with a temperature greater than 140°K (the point at which significant increase in 8.5 micron flux is noted in the integral solution) to the crescent. As this represents an area within 10° in longitude of the sunset terminator on the limb, the resultant change in projected area is negligible, as is the change in the temperature of the crescent. However, it does mean that the resultant dark side measurement more nearly compares with the model solution at the point where the 8.5 micron flux becomes significant, and the 8.5, 12, and 20 micron solutions are still within 1°K of each other. As this point is also within 1°K of the full hemispherical integral temperature at 20 microns for phase 180°, the 20 micron results are here used to represent the 'color' temperature of the dark side to compare with the above measurement. The results for various Gamma are plotted in Figures 3.6 and 3.7.

Figures 3.6 and 3.7 clearly show a sinusoidal like variation in the dark side 'color' temperature with an amplitude of 5°K as a function of days from perihelion. It is necessary then to include the eccentricity of Mercury's orbit in the solution, even for the night side, rather than assuming a constant mean rotation at mean distance. The one dark side data point gives a best fit to a surface with Gamma = 575 ± 50. This value of Gamma is also in agreement with the computations of Morrison and Sagan (1967). More data is awaited to see how real the above sinusoidal variation is. A Gamma = 1000 (dust) surface is combined with a Gamma = 20 (rock) surface in Figure 3.9 to determine that a surface containing 3% rock also fits the data point. A dark side 20 micron measurement would be useful to evaluate this point. This increase in percentage rock as compared to the value of 0.15% obtained for the Moon is not inconsistent with the increase in surface roughness compared to that of the Moon.

Chapter IV - The Homogeneous Model Applied to Exterior Objects.

4.A - General Considerations.

In order to complete this survey of the homogeneous model, cooling and integral temperature curves are computed for the remaining objects in the Solar system for which infrared data is obtainable that may be representative of thermal surface emission. The objects are Mars, Vesta, Ceres, Io, Europa, Ganymede, Callisto, Titan and Triton. These nine objects are grouped together because of the small amount of data presently known about their surface properties, and because the terminology and methods used to generate the curves are adequately covered in the preceding chapters. In the case of the asteroids, Ceres and Vesta are taken as representative. The orbits of Pallas and Juno are close enough to that of Ceres, for their data, when corrected to the proper distance to be compared to the results given here for Ceres. In addition to the determination of surface cooling curves and integral brightness temperatures, integral eclipse cooling is also included for the Jovian satellites. The orbital information used for the above objects is given in table 4.1 along with their Bond emissivities, radii and maximum visible phase. The observational evidence is discussed with the results of section 4.B.

Table 4.1

Exterior Objects Parameters

Object	Mean Dist [AU]	Inc to Ecl [0]	Rot Per	Object Radius [km]	Max Phase	Bond Emis.
Mars	1.52	0	24^h37^m	3380	45	0.84
Vesta	2.36	0	5^h20^m	300	25	0.88
Ceres	2.77	0	9^h05^m	350	22	0.97
IO	5.20	0	$1^d18^h29^m$	1670	12	0.46
Europa	5.20	0	$3^d13^h18^m$	1460	12	0.51
Ganymede	5.20	0	$7^d04^h00^m$	2550	12	0.71
Callisto	5.20	0	$16^d18^h05^m$	2360	12	0.85
Titan	9.54	0	$15^d23^h15^m$	2440	6	0.80
Triton	30.07	0	$5^d21^h03^m$	2000	2	0.79

The calculations are made for mean distance in each case, and all objects are considered to have their spin axes perpendicular to the ecliptic. In the case of Mars this represents a sizable known error as the spin axis is inclined 24° to the orbit plane. For the cooling curves this results in MLAT = 0° behaving more like MLAT = 20°. The integral solutions are not seriously affected.

Since the phase functions for the above objects are uncertain, the Bond albedos and thus the Bond emissivities are also not well known. The emissivity used should be lowered somewhat from the Bond emissivity to allow for increased reflection in the infrared. However, there are so many unknowns here that the Bond emissivities as derived from the measurements of Harris (1961) are used unaltered, except for the following. That of Ceres is close, and thus set equal to the value of 0.93 used for Mercury and the Moon. Vesta is treated as a special case. Solutions are also obtained for the Jovian satellites with $\varepsilon_b = 0.93$ for purposes of comparison as will be found tabulated in tables 4.9 and 4.10. The surface infrared emissivity is held constant at 0.93.

Mars, whose atmospheric pressure is known to be less than 20 mb, is taken to be transparent in the infrared; any atmospheres of the other bodies are also neglected in the calculations. The small effect of radiation from the planet Jupiter at 137°K (Aurmann et al., 1969) is also neglected in the solution for JI–JIV, as is Saturn, Neptune for Titan, Triton respectively.

The step sizes found best suited to the solutions are equal to those used for the Moon:

$$\Delta t = \frac{\text{diurnal period}}{360}$$

$$\Delta x = 0.05 \text{ thermal wavelength.}$$

The thermal wavelengths and Δt are found in table 4.2.

Table 4

Thermal Wavelength λ[cm] and Δt [Min]

Gamma	20	50	100	200	300	400	500	600	800	1000	1200	Δt
Mars λ	14.00	5.60	5.60	2.80	1.87	1.40	1.12	0.93	0.70	0.56	0.47	4.10
Vesta λ	6.51	2.61	2.61	1.30	0.87	0.65	0.52	0.43	0.33	0.26	0.22	0.89
Ceres λ	8.50	3.40	3.40	1.70	1.13	0.85	0.68	0.57	0.43	0.34	0.28	1.51
JI λ	18.38	7.35	7.35	3.68	2.45	1.84	1.47	1.23	0.92	0.74	0.61	7.08
JII λ	26.04	10.42	10.42	5.21	3.47	2.60	2.08	1.74	1.30	1.04	0.87	14.20
JIII λ	36.97	14.79	14.79	7.39	4.93	3.70	2.96	2.46	1.85	1.48	1.23	28.62
JIV λ	56.46	22.58	22.58	11.29	7.53	5.65	4.52	3.76	2.82	2.26	1.88	66.76
Titan λ	55.18	22.07	22.07	11.04	7.36	5.52	4.41	3.68	2.76	2.21	1.84	63.78
Triton λ	33.50	13.40	13.40	6.70	4.47	3.35	2.68	2.23	1.68	1.34	1.12	23.51

Again, a specific heat of 0.2 cal/gm°K is used throughout, as is ρ=3.0 gm/cm^3 for Gamma <100, and 1.5 gm/cm^3 for Gamma $\geq$100. For each body, using the above parameters, diurnal cooling curves are obtained for the following values.

Table 4.3

GAMMA	20	50	100	200	300	400	500	600	800	1000	1200
MLAT	0	20	40	60	80						

Following this, integral curves are obtained by numerical integration using a basic grid of diurnal solutions placed 20° apart in planetocentric MLAT, MLONG as explained in detail in section 3.C. Total, day side, and dark side integral brightness temperatures as a function of phase for 3.8, 8.5, 12 and 20 microns and the Gammas listed in table 4.3 are calculated.

Table 4.4 describes the diurnal and integral temperature model results included in this thesis. The 8.5, 20 micron integral solutions fall approximately 2° above and respectively below that of the 12 micron curves depicted in figures 4.9 - 4.17. Calculations below 8 microns are not included, as the data in this region represents scattered sunlight rather than thermal emission.

Table 4.4

Description of Exterior Object's Model Results

FIGURE		DESCRIPTION
	4.1	Mars, MLAT = 0°, 40°, all Gamma.
	4.2	Vesta, MLAT = 0°, 40°, all Gamma.
	4.3	Ceres, MLAT = 0°, 40°, all Gamma.
	4.4	Io, MLAT = 0°, 40°, all Gamma.
	4.5	Europa, MLAT = 0°, 40°, all Gamma.
	4.6	Ganymede, MLAT = 0°, 40°, all Gamma.
	4.7	Callisto, MLAT = 0°, 40°,all Gamma.
	4.8	Titan, Triton, MLAT = 0°, 40°, all Gamma.
	4.9	Mars, integral 12 micron temp,all Gamma, all phase.
	4.10	Vesta, integral 12 micron temp, all Gamma, all phase.
	4.11	Ceres, integral 12 micron temp, all Gamma, all phase.
	4.12	Io, integral 12 micron temp, all Gamma, all phase.
	4.13	Europa, integral 12 micron temp, all Gamma, all phase.
	4.14	Ganymede, integral 12 micron temp, all Gamma, all phase.
	4.15	Callisto, integral 12 micron temp, all Gamma, all phase.
	4.16	Titan, integral 12 micron temp, all Gamma, all phase.
	4.17	Triton, integral 12 micron temp, all Gamma, all phase.

Table 4.4 (continued)

Table 4.5

Bottom Temperature for 0° MLAT

Gamma	Mars	Vesta	Ceres	JI	JII	JIII	JIV	Titan	Triton
20	234	193	178	109	112	121	127	94	52
50	232	193	178	109	111	120	126	94	52
100	227	192	177	109	111	120	124	93	52
200	221	192	177	108	110	119	122	93	52
300	216	190	176	108	110	118	120	92	52
400	212	188	173	108	109	117	118	92	52
500	210	186	171	107	109	115	117	91	52
600	207	184	170	107	108	114	115	90	52
800	203	181	167	106	107	112	113	89	51
1000	201	179	165	106	106	111	112	88	51
1200	198	177	164	105	105	110	111	87	51

Table 4.6

Bottom Temperature for 40° MLAT

Gamma	Mars	Vesta	Ceres	JI	JII	JIII	JIV	Titan	Triton
20	219	180	166	102	104	113	119	88	48
50	218	180	166	102	104	113	118	88	48
100	214	179	166	102	104	113	117	88	48
200	209	179	165	102	104	112	115	87	48
300	204	179	165	102	103	111	113	87	48
400	201	177	164	102	103	110	112	87	48
500	198	176	162	101	103	109	110	86	48
600	196	174	161	101	102	108	109	85	48
800	193	172	158	100	101	106	107	84	48
1000	190	170	156	99	100	105	106	83	48
1200	188	168	155	98	99	104	105	82	48

Table 4.7

Integral Dark Side Color Temperature

Gamma	Mars	Vesta	Ceres	JI	JII	JIII	JIV	Titan	Triton
20	210	185	171	109	112	121	127	94	52
50	205	184	170	108	110	118	122	91	52
100	190	182	167	107	108	112	113	88	52
200	179	175	161	105	105	107	104	85	52
300	168	168	155	102	101	102	98	82	52
400	160	162	149	100	97	98	94	80	52
500	153	158	145	97	95	95	90	78	52
600	148	154	141	95	93	92	88	76	51
800	140	147	135	92	89	88	83	73	51
1000	134	142	130	89	86	85	81	70	50
1200	129	138	127	87	84	82	77	68	50

Table 4.8

Integral 12μ Temperature at Phase Zero

Gamma	Mars	Vesta	Ceres	JI	JII	JIII	JIV	Titan	Triton
20	230	185	171	109	112	121	127	94	52
50	236	188	175	111	115	124	130	96	52
100	248	197	183	113	118	128	135	98	53
200	261	203	188	115	119	131	140	100	53
300	267	206	191	116	120	134	144	102	53
400	270	209	194	116	121	136	146	104	54
500	272	212	196	117	123	138	147	106	54
600	273	214	198	119	124	139	148	107	54
800	275	217	201	120	126	141	150	109	54
1000	276	219	203	122	128	142	151	110	54
1200	276	221	205	123	129	143	151	111	55

Table 4.9

Integral Dark Side 'Color' Temperature
JI-JIV, $\varepsilon_B = 0.93$

Gamma	JI	JII	JIII	JIV
20	126	126	126	126
50	123	123	120	119
100	120	120	115	112
200	116	114	110	106
300	113	110	106	99
400	111	107	102	95
500	109	104	98	91
600	106	101	95	89
800	102	96	91	84
1000	98	93	87	81
1200	95	90	84	78

Table 4.10

Integral 12μ Temperature at Phase zero
JI-JIV, $\varepsilon_B = 0.93$

Gamma	JI	JII	JIII	JIV
20	126	126	126	126
50	127	129	130	131
100	130	133	135	138
200	134	137	140	144
300	138	141	146	148
400	141	144	147	150
500	143	146	149	151
600	145	148	151	152
800	147	150	152	153
1000	149	151	153	154
1200	150	152	153	154

4.B - Diurnal and Integral Cooling Curves.

The effects of rotation are clearly visible in all of the curves where the waxing, waning temperature difference is substantial whereas for Mercury this difference is zero. As the rotation increases so does the maximum temperature lag zero phase, and the amplitude of the temperature extremes diminish, falling progressively below the instantaneous equilibrium with sunlight surface temperature. In the cases of Gamma=20 a near constant temperature solution is reached such that the flux radiated at a given latitude equals the incident solar flux. This constant equilibrium temperature is given by equation 4.1 since for Gamma in the range considered here, lateral flux diffusion may be neglected. In Figures 4.9-4.17 the upper curve marked $\text{EQUIL}^{\text{MAX}}$ represents the instantaneous equilibrium condition, and the bottom curve also marked $\text{EQUIL}^{\text{MIN}}$ represents the equation 4.1 temperature.

$$T = \left(\frac{\text{Solar Flux } \varepsilon_B}{R^2 \pi \sigma \varepsilon_{IR}} \times \cos\ (\text{MLAT}) \right)^{1/4} \tag{4.1}$$

In this region of low Gamma and substantial spin, it is also noted that convergence for the first time became a problem. One cannot simply take the bottom temperature to be the average of the surface temperature over the first diurnal period as has been done previously. This results in solutions in error by as much as 20°K toward higher temperatures unless successive relaxation and recalculation of the bottom temperature is performed over fifty or more diurnal periods. However, solutions to $\pm$ 2°K are obtained within the four diurnal periods used, if the bottom temperature is initially set to that of equation 4.1. This is done in the curves presented here in these cases.

Numerous data have been amassed on the Red Planet in the past few decades, especially with the advent of the Mariner series (Michaux, 1967). A great deal more will be known when the Mariner 1971 and Viking 1975 missions are complete. However, to date observational infrared data from the ground is lacking. The observations made by Sinton and Strong (1960) near opposition of July 20, 1954 have yet to be surpassed.

The data of Sinton and Strong, corrected to mean distance, are plotted in figure 4.1 where they are seen to best fit a Gamma = 170 $\pm$ 50 surface. This compares favorably with the original estimate of Gamma = 100 - 250 by Sinton and Strong who also found that the planet's dark areas are 8°K warmer than the light areas (a variation in Gamma of 100 for a surface in the range of Gamma = 200). Morrison et al. (1969) have recently reworked this data to obtain a near dawn temperature of 180°K and a -60° MLAT temperature of 161°K. Making allowance for a greenhouse effect, they also found a Gamma = 200. The present model obtains for Gamma = 170, 176°K predawn and 219°K at -60°MLAT in comparison. This difference is explained by part of Sinton and Strong's beam at -60°MLAT including a polar CO_2 ice cap which theoretically should remain at the frost temperature of CO_2 under Martian pressure of 150°K. Neugebauer (1969) from measurements on board Mariner VI and VII obtains a value of 150°K for the polar cap in agreement with a CO_2 composition.

A working value of 234 ± 7°K seems to be accepted in the field of present ground work for the integral temperature of Mars from 5 - 100 microns (Aumann et al. 1969). As seen from table 4.8, this corresponds to a surface of Gamma = 20. The neglect of the polar caps at 150°K and the neglect of the polar axis tilt in the model should result in an integral error of less than 3°K in the direction of a lower temperature on the part of the model. In contrast one would expect the measured values to be from 2°K to 20°K high due to surface roughness as seen in table 4.11 where the measured temperatures and corresponding Gammas are tabulated for various percentages of forward peaked flux due to surface roughness. It is remembered that 50% forward peaking was found for Mercury and 10% for the Moon. 40% is in all cases assumed for deriving a surface value of Gamma with only phase zero integral measurements. Using the model, Gamma = 170, as found from the Sinton and Strong data, and 40% peaking, one arrives at a 12μ integral brightness temperature of 212°K. If anything, the Martian atmosphere would raise this value still higher. This is in contrast to the above measured value of 234°K.

On the opposite side, recent results at the O'Brien Observatory give a measured 12 micron integral brightness temperature of 270 ± 10°K (Murdock, private communication) corresponding to a model Gamma of 170 for 35% flux peaking. This result then agrees closely with that of Sinton and Strong as compared by way of the model.

The above comments represent the present uncertainty in the thermal measurements of Mars. In light of Neugebauer's (1969) dark side measurement of 200°K from Mariner VI and Morrison's (1969) near dawn temperature of 180°K a surface for Mars with Gamma less than 100 is unlikely. From the ground it would be useful to measure the difference between the waning and waxing temperatures at maximum phase to help determine the value of Gamma for Mars. A reliable 20 micron measurement is also needed to determine whether or not the Gamma = 170 surface can be explained by a combination of rock (Gamma=20) and dust (Gamma=1000) as was done for the Moon. The above observations make this uncertain, so no attempt is made here to calculate the percentage rock in this way, nor is an attempt made in the remaining cases for the same reasons.

Table 4.11

Comparison of Measurements With Model for Various % Surface

Roughness Forward Peaking of Flux

	T_B	T_A	10%	20%	30%	40%	50%	60%
Mars	270	274 (700)	268 (330)	263 (230)	259 (180)	255 (150)	251 (120)	248 (100)
Ceres	199	201 (800)	198 (600)	195 (450)	193 (330)	190 (300)	189 (230)	187 (180)
JI	141	142 (none)	141 (none)	139 (none)	138 (none)	137 (none)	135 (none)	134 (none)
JII	132	133 (none)	132 (none)	131 (none)	129 (1200)	128 (1000)	127 (900)	126 (800)
JIII	143	144 (none)	132 (1200)	141 (800)	140 (700)	139 (600)	138 (500)	137 (450)
JIV	160	162 (none)	160 (none)	158 (none)	156 (none)	155 (none)	153 (none)	151 (1200)
Titan	125	126 (none)	125 (none)	124 (none)	123 (none)	122 (none)	121 (none)	120 (none)

where T_B = observed 12 micron integral brightness temperature.

T_A = corresponding model surface integral temperature with ε_{IR} = .93.

XX% = model surface temperature such that 1.XX its flux corresponds to T_A integral surface temperature °K (corresponding Gamma).

Vesta is included in this thesis at the suggestion of David Allen who used the results presented here to calculate the infrared diameter of this object, (Allen, 1970b). With an angular diameter of 0.5 arc sec, nothing visual is known about its surface features. That its surface is rough is known from the variations in its visible signal from which its rotational period is derived. Further, few measurements have been made of either its diameter or albedo. Based on an integral brightness 12 micron temperature of 220°K at mean distance derived from a consideration of the rotational effects seen from the model with a Gamma = 1000 surface, Allen obtains a diameter of 600 km, and a Bond albedo of 0.12 as compared to earlier accepted values of 380 km and 0.27 respectively. Since the infrared measurements to date have been coupled with this model to obtain a more reasonable diameter, they cannot then be used to obtain a surface value for Gamma until the uncertainty in Vesta's radius is settled. However, it is also possible to fit observational data to a value for Gamma by taking readings for both the waxing and waning cases at maximum phase, although this has not been done to date.

Ceres, used here as representative of the asteroids, being somewhat larger than Vesta, has less uncertainty connected with the measurements of its radius and albedo. Nothing is known of its surface features other than that they are rough. The Bond albedo is

0.03; however, to minimize parameter changes whenever possible, a Bond emissivity of 0.93 is used, the error thus introduced being negligible and consistent with increased reflection towards the infrared. Measurements at Minnesota (Murdock, private communication) give an integral 12 micron brightness temperature of 199°K. The corresponding model surface value of Gamma is 300 $\pm$ 50 with 40% forward peaking as shown in table 4.11. Measurements with phase would also be useful here.

As in the case of the asteroids, the physical characterisitcs of the Jovian satellites are not well known. There is just enough variation in the visible brightness curves to show their rotation to be synchronous. Io, like Mars, is reddish in color. The albedo dependence with wavelength for Io and Callisto is not unlike that of Mars' central regions, while Europa and Ganymede resemble the spectrum of Mars' polar cap. However, theoretical estimates predict that any such polar cap would have dissipated during the lifetime of the solar system given the present measured surface temperatures (Moroz, 1968, p. 385). In addition Io possesses an anomalously high albedo at 3.5 microns while the others strongly absorb at this wavelength (Gillett, Merrill and Stein, 1970). The existence of an atmosphere on Io, Europa, and Ganymede could help to explain their high and variable albedo curves, but there is no concrete evidence for the presence of an atmosphere on any of them. Callisto, the largest, has the most lunar like characteristics.

The data used to compare with, and plotted on Figures 4.11 - 4.14 are those of Gillett, Merrill and Stein (1970). An examination of tables 4.8 and 4.11 show that the measured temperature for Io is higher by 12°K than a Gamma = 1000 surface given 60% forward peaking. Table 4.10 gives a fit to Gamma = 200-450 depending on the choice of forward peaking for $\varepsilon_B = 0.93$. Since increasing the present radius by the needed amount if unlikely, one is left to choose between the existence of an atmosphere and its corresponding increase in the temperature, and/or a highly non thermal surface. The Gamma = 20 hypothesis can be tested by observing Io in eclipse, although observationally this is difficult due to the closeness of Io to Jupiter. Jupiter itself may also be affecting this satellite.

Europa, as seen from table 4.8 and figure 4.12, compares favorably with a Gamma = 1000 $\pm$ 50 surface at 40% forward peaking. Table 4.10 shows it to fall below any reasonable Gamma estimate for $\varepsilon_B = 0.93$.

Ganymede, table 4.8 and figure 4.13, best fits Gamma = 600 $\pm$ 50 and also falls below any reasonable estimate for $\varepsilon_B = 0.93$.

Callisto, the one satellite that does not have an anomously high albedo, compares to Gamma = 1200 $\pm$ 50 at 60% forward peaking, and Gamma = 1000 $\pm$ 50 with 40% forward peaking with ε_B = 0.93.

The measured value for Titan is 125°K (Allen and Murdock, 1971). As seen from tables 4.8 and 4.11, this measurement even falls some 10°K above a high Gamma surface with 60% forward peaking. This is very similar to the result for Io, and again points to the existence of an atmosphere.

4.C - The Jovian Satellites in Eclipse.

The eclipses of the Jovian satellites is made more difficult than that described for the Moon in section 2.D in that an integral solution need be performed over the visible hemisphere in order to compare with observations. However, the uncertainties inherent in an integral solution allow the following approximations to be applied in determining the circumstances of the eclipses.

Firstly, it is assumed that the Sun and Jupiter are in the orbital plane of a given satellite, and that the minimum distance between the Sun and Jupiter at closest approach as seen from any position on the satellites be zero. This is valid as the radius of Jupiter is large with respect to that of the Sun for an observer located on one of the satellites. Secondly, the time in total eclipse for all satellites is set to approximately 150 minutes. As will be seen this is close to the maximum eclipse time possible for JI and JII. It is somewhat less than the maximum time for JIII and JIV. However, these satellites normally cut through the shadow in such a manner as to make their times in eclipse closer to the above value than to their maximum values. What is important here is that the major cooling takes place within the first 150 minutes, and the solution is not altered, other than being foreshortened, by the neglect of additional time in eclipse beyond this. Thirdly, the edge of Jupiter in obscuring the Sun is considered to be a sharp edge; that is, detailed effects of Jupiter's atmosphere are neglected. As is seen in section 2.D, the first order effect of the Earth's atmosphere is to increase the effective planet radius. Here since the radius is large, its exact size is not important. Undoubtedly, Jupiter's atmosphere plays a more important role in the circumstances of insolation during the penumbral phase; however, this phase is short with respect to the umbral period and thus such detailed effects may also be neglected. In fact, as is seen from the results of this section, one may simply consider the Sun to be instantaneously switched off and on, although in this study the formalism of section 2.D is used as it is already incorporated into the program. Finally, the phase throughout the event is considered to be zero for an observer located at the Earth. In the case of Io the phase variation is $\pm 10°$, however, as has previously been determined, the integral solutions are nearly flat within 10° of phase zero, thus this approximation is also reasonable.

With these approximations in mind, the following quantities are determined. The radius of Jupiter with respect to that of the Sun as seen from a given satellite is:

$$(4.1) \qquad RJ' = \frac{\text{radius of Jupiter}}{\text{satellite orbital radius}} \times \frac{\text{Sun-Jupiter distance}}{\text{radius of the Sun}}$$

The time duration for the entire satellite to enter the umbral shadow is:

$$(4.2) \qquad T_p = \frac{\text{radius of satellite x satellite orbital period}}{\pi \text{ satellite orbital radius}}$$

The time duration of the penumbral phase for an observer positioned on the satellite is

$$(4.3) \qquad T'_{12} = \frac{\text{radius of the Sun x satellite orbital period}}{\pi \text{ Sun-Jupiter distance}}$$

The maximum umbral period for an observer on the satellite is:

$$(4.4) \qquad T'_m = \frac{\text{satellite orbital period}}{\pi} \text{ x } \sin^{-1} \left[\frac{\text{radius of Jupiter}}{\text{satellite orbital radius}} \right].$$

As explained above and for computational reasons, the actual umbral period employed by the model is:

$$(4.5)\quad T'_a = 150 + 2\,(2.92 - T'_{12})\ \text{minutes.}$$

This is done to allow the total time of the event $T_t = T'_a + 2T'_{12}$ to remain constant for all satellites in order to facilitate graphical plotting.

Next, to use the results of section 2.D and equation 2.19 to determine the incident solar flux, the VELSUN there described is here calculated such that the Sun travels its diameter in the time interval T'_{12}. Since, being large, the exact size of Jupiter's radius is not important, an effective radius is calculated in order to make use of the equations of 2.D,

$$(4.6)\qquad RE' = \frac{1}{2}\,(T_t \times \text{VELSUN} - 2)$$

In this manner the circumstances of the eclipses are prepared for the homogeneous model solutions. The parameters are tabulated for each satellite in table 4.12.

From this point a calculation of the integral flux from the surface throughout the eclipse is performed in a manner similar to that described in

Table 4.12

Jovian Satellite Eclipse Parameters

	RJ'	RE'	T_p	T'_{12}	T'_m	T'_a	VELSUN
UNITS	$R'_{\odot}$	$R'_{\odot}$	min	min	min	min	$R'_{\odot}$/min
JI	191.14	111.20	3.68	0.72	137.96	154.40	1.44
JII	118.86	107.31	4.09	1.44	173.10	152.96	1.39
JIII	74.84	52.76	8.02	2.92	218.47	150.00	0.69
JIV	42.59	21.60	10.27	6.80	289.99	142.24	0.29

detail for Mercury in section 3.C, and used previously in this chapter. For a given satellite and Gamma, diurnal solutions are obtained for the following satellite positions.

MLONG=80,60,40,20,0,340,320,300,280

MLAT=0,20,40,60,80 .

The solutions are each carried through four diurnal periods, and in the fourth period halted with respect to MLONG = 0 at the following fractions of a period, F_p = 1 - MLONG/360.0, where MLONG = 0 is initially set to waxing phase equal to

$$\frac{180\ T_t}{\text{satellite orbital period}}\ \text{degrees}$$

to allow local noon for MLONG = 0 to occur at mid-totality. In this way the proper surface temperature, and temperature with depth is found at each of the 45 grid points immediately prior to initial contact. With this information the program switches into the eclipse mode of the program described in section 2.C for each grid point, and proceeds with the solution through the eclipse and for an additional 30 minutes where surface warming is taking place. As it takes the shadow T_p minutes to cross the satellite, a delay time

(4.7) $$DT = T_p(1 - \sin(\text{MLONG}))/2$$

is also here included such that DT = 0 for the East limb and DT = T_p on the West limb. This procedure then gives the same time to all of the solutions with respect to the initiation of the event on the East limb, making it a simple matter to integrate over the surface with respect to this one time. For a given satellite and Gamma at each grid point, the eclipse surface temperature solutions are then stored at intervals of $T_t/120$ in time. The values of Gamma (depth steps) used for each satellite are 500 (.02 cm), 1000 (.01 cm) and 1400 (.01 cm). The time step is 0.27 min.

Given the almost total lack of measurement of the Jovian satellites in eclipse it is felt that this range in Gamma under eclipse conditions is sufficient for the present.

Making use of equation 3.2, 121 12 micron hemispherical surface brightness integrations are performed for phase zero to obtain the desired complete integral eclipse solution with time for a given satellite and Gamma. The results of all this are found in figures 4.15 and 4.16.

In looking at the results one first notices that the curves closely resemble the discharge, charge voltage curve of a capacitor in a simple RC circuit. Secondly, one sees that the integral temperature is still some 10° less than its initial starting value thirty minutes after the end of the eclipse. That this is not an error of say the insolation function in the program was tested by carrying a test solution for an additional two hours where it was found that the warming curve as one would expect follows closely the inverse of the cooling curve, arriving at the original temperature some two hours after the termination of the event. The model then shows that eclipse cooling and subsequent warming is not instantaneous, even for Gamma = 1400. This effect is hidden by the long prenumbral period during lunar eclipses. The additional one and one half hours of warming are not included on the figures, as their path is clear and it is desired to show the slopes of the early cooling and warming portions of the graphs in a measurable fashion. In contrast to these model results, the smoothed 8-14 micron flux intensities obtained for the eclipse cooling of Ganymede on the night of December 12, 1963, by Murray et al. (1965), here normalized to the Gamma = 1000 case and converted to 12 micron brightness temperatures, are also plotted. Gamma = 1000 is chosen as the slope of the converted data most nearly fits this case for initial cooling, and final cooling if one is allowed to slide the data in temperature. Such a value of Gamma is consistent with the results of table 4.11 and the observed increase in Gamma for the lunar eclipse case. The converted, normalized data however clearly show a surface with a Gamma substantially higher than 1400. Because of the computer time involved this point is not pursued further, until such time when more Jovian satellite eclipse data are obtained.

References

Allen, C. W. 1963 Astrophysical Quantities, The Athlone Press, London.

Allen, D. A. 1970a, Infrared Studies of the Lunar Terrain, Astrophysics Report No. 5, School of Physics and Astronomy, University of Minnesota, (Ph.D. dissertation, University of Cambridge, July 1970).

Allen, D. A. 1970b, Infrared Diameter of Vesta, Nature 227, 158.

Allen, D. A. and Ney, E. P., 1969, Lunar Thermal Anomalies-Infrared Observations, Science 164, 419.

Alter, D. 1968, Lunar Atlas, Dover, New York.

Aumann, H. H., Gillespie, C. M. Jr., and Low, F. J., 1969, The Internal Powers and Effective Temperatures of Jupiter and Saturn, Astrophys. J. 157, L69.

Carmichel, H. and Dolfus, A., 1968, La Rotation et la Cartographie de la Planete Mercure, Icarus 8, 216.

Crank, J. and Nicholson, P. 1947, A Practical Method for Numerical Evaluation of Solutions of Partial Differential Equations of the Heat-Conduction Type, Phil. Soc. 43, 50.

Dyce, R. B., Pettengill, G. H., and Shapiro, I.I., 1967, Radar Determination of the Rotations of Venus and Mercury, Astron. J. 72, 351.

Gillett, F. C., Merrill, K. M., and Stein, W. A., 1970, Albedo and Thermal Emission of Jovian Satellites, I-IV, Astrophys. Letters 6, 247.

Harris, D., 1961, Planets and Satellites, Kuiper, G. P. and Middlehurst, B. M., ed., The University of Chicago Press, Chicago.

Hovis, W. A. and Callahan, W. R., 1966, Infrared Reflectance Spectra of Igneous Rock, Tuffs, and Red Sandstone from 0.5 - 22 microns, J. Opt. Soc. Am., 56, 639.

Kopal, Z., 1962, Physics and Astronomy of the Moon, Academic Press, New York.

Link, F., 1969, Eclipse Phenomena in Astronomy, Springer-Verlag, Berlin.

Linsky, J. L., 1966, Models of the Lunar Surface Including Temperature Dependent Thermal Properties, Icarus 5, 606.

Low, F. J., 1965, Lunar Nighttime Temperatures Measured at 20 Microns, Astrophys. J. 142, 806.

Michaux, C. M. 1967, Handbook of the Physical Properties of the Planet Mars, NASA SP-3030.

Mills, G. A. and Sudbury, P. V. 1968, Absolute Coordinates of Lunar Features, Icarus 9, 538.

Moroz, V. I., 1968, Physics of Planets, NASA TTF-515.

Morrison, D., 1970, Thermophysics of the Planet Mercury, Bull. Amer. Astron. Soc. 2, 238.

Morrison, D. and Sagan, C., 1967, The Microwave Phase Effect of Mercury, Astrophys. J. 150, 1105.

Morrison, D., Sagan, C. and Pollack, J. B. 1969, Martian Temperatures and Thermal Properties, Icarus 11, 36.

Murdock T., 1970, Infrared Observations of the Temperature of the Planet Mercury, Thesis, Master of Science, University of Minnesota.

Murdock, T., and Ney, E. P., 1970, Mercury: The Dark Side Temperature, Science 170, 535.

Murray, B. C., Westphal, J. A., and Wildey, R. L., 1965, The Eclipse Cooling of Ganymede, Astrophys. J. 141, 1590.

Neugebauer, G., et al., 1969, Preliminary Results of Infrared Radiometer Experiment On Board Mariner 7, 1969, Science 166, 98.

pet(1) 1969, Preliminary Examination of Lunar Samples from Apollo 11, Science 165, 1211.

Phinney, R. A., O'Keefe, J. A., Adams, J. B., Gault, D. E., Kuiper, G. P., Masursky, H., Collins, R.J. and Shoemaker, E. M., 1969, The Implications of the Surveyor 7 Results, J. Geophys. Res., 74, 6053.

Roelof, E. C., 1968, Thermal Behavior of Rocks on the Lunar Surface, Icarus 8, 138.

Sinton, W., and Strong, J., 1960, Radiometric Observations of Mars, Astrophys. J. 131, 459.

89
48
137

Smith, G. D., 1965, Numerical Solution of Partial Differential Equations, Oxford University Press, London.

Thekaekara, M. P., Kruger, R., and Duncan, C. H., 1969, Solar Irradiance Measurements from a Research Aircraft, Applied Optics 8, 1713.

Troitsky, V. S., Burov, A. B. and Alyoshina, T. N., 1968, Influence of the Temperature Dependence of the Lunar Material Properties on the Spectrum of the Moon's Radio Emission, Icarus 8, 423.

Wesselink, A. J., 1948, Heat Conductivity and Nature of the Lunar Surface Material, Bull. Astr. Inst. Netherlands, 10, 351.

Wildey, R. L, Murray, B. C. and Westphal, J. A., 1967, Reconnaissance of Infrared Emission from the Lunar Nighttime Surface, J. Geophys. Res., 72, 3743.

Winter, D. F., and Saari, J. M., 1969, A Particulate Thermophysical Model of the Lunar Soil, Astrophys. J. 156, 1135.

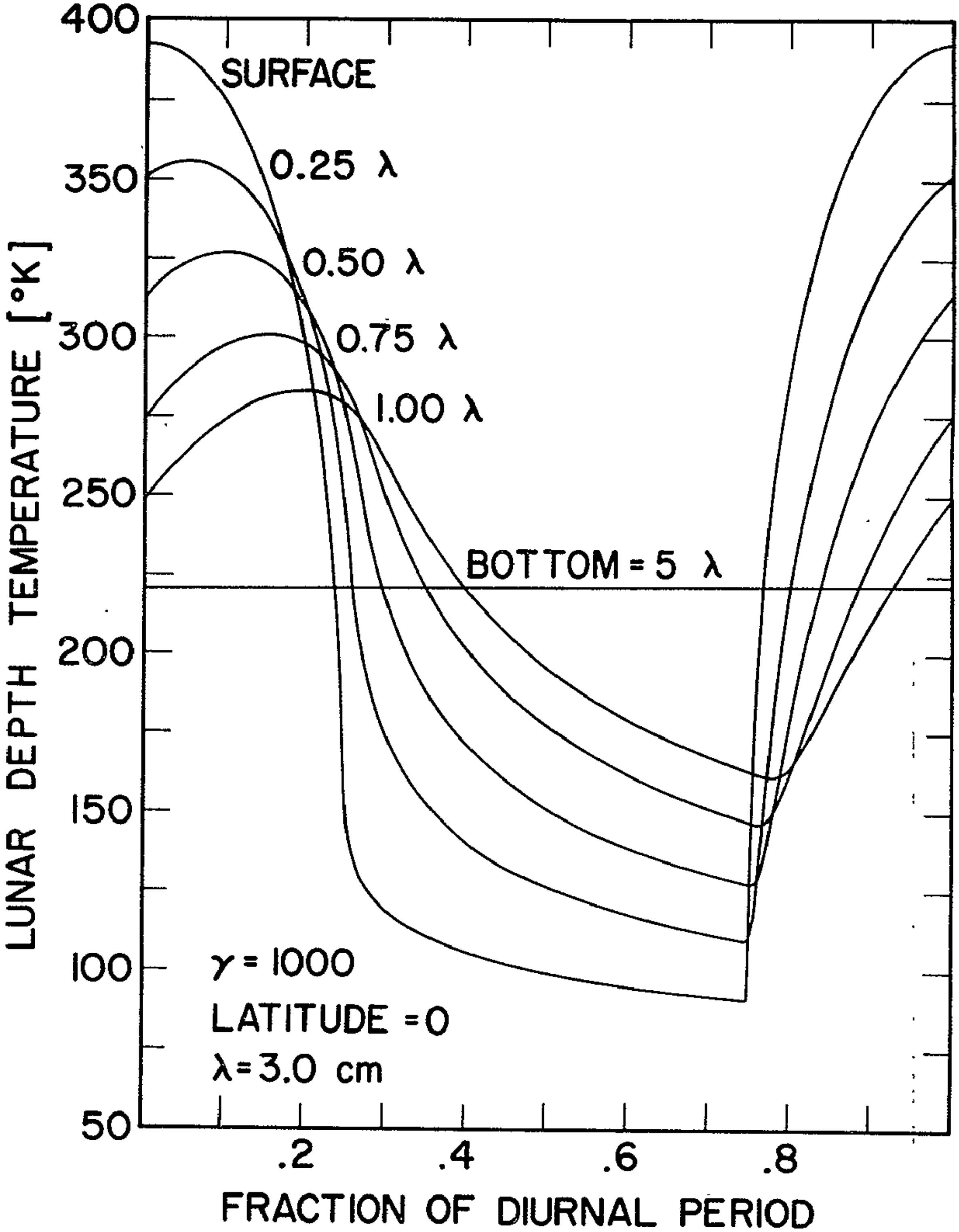

Figure 2.1. Lunation cooling solutions with depth for Gamma = 1000 and SSLAT = 0°. The five curves represent 0,.25,.50,.75,1.0, and 5.0 thermal wavelengths in depth, where the thermal wavelength is 3.0cm.

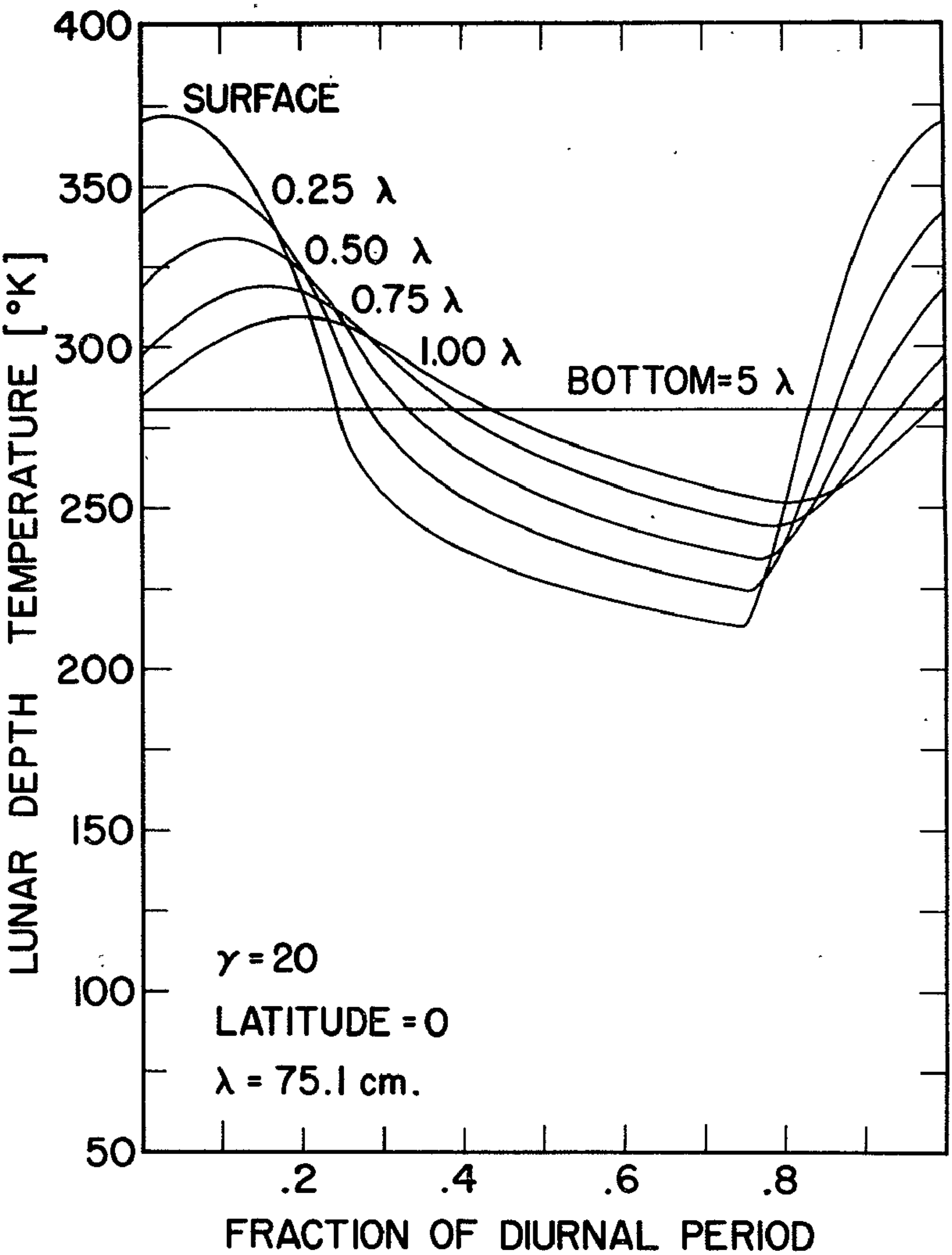

Figure 2.2. Lunation cooling solutions with depth for Gamma = 20 and SSLAT = 0°. The five curves represent 0,.25,.50,.75,1.0, and 5.0 thermal wavelengths in depth, where the thermal wavelength is 75.1cm.

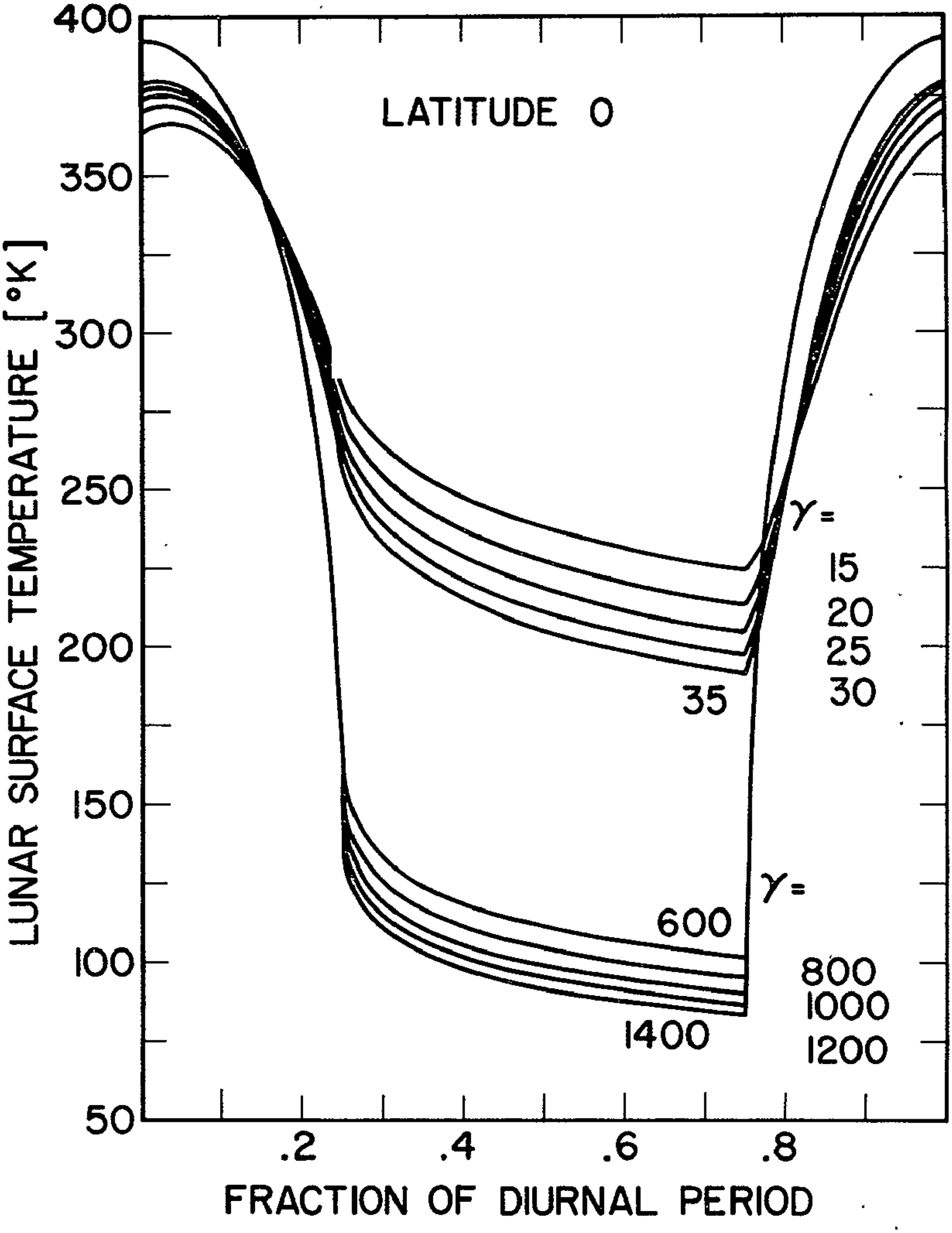

Figure 2.3. Lunation cooling solutions for SSLAT = 0°, and Gamma = 15,20,25,30,35,600,800,1000,1200, and 1400.

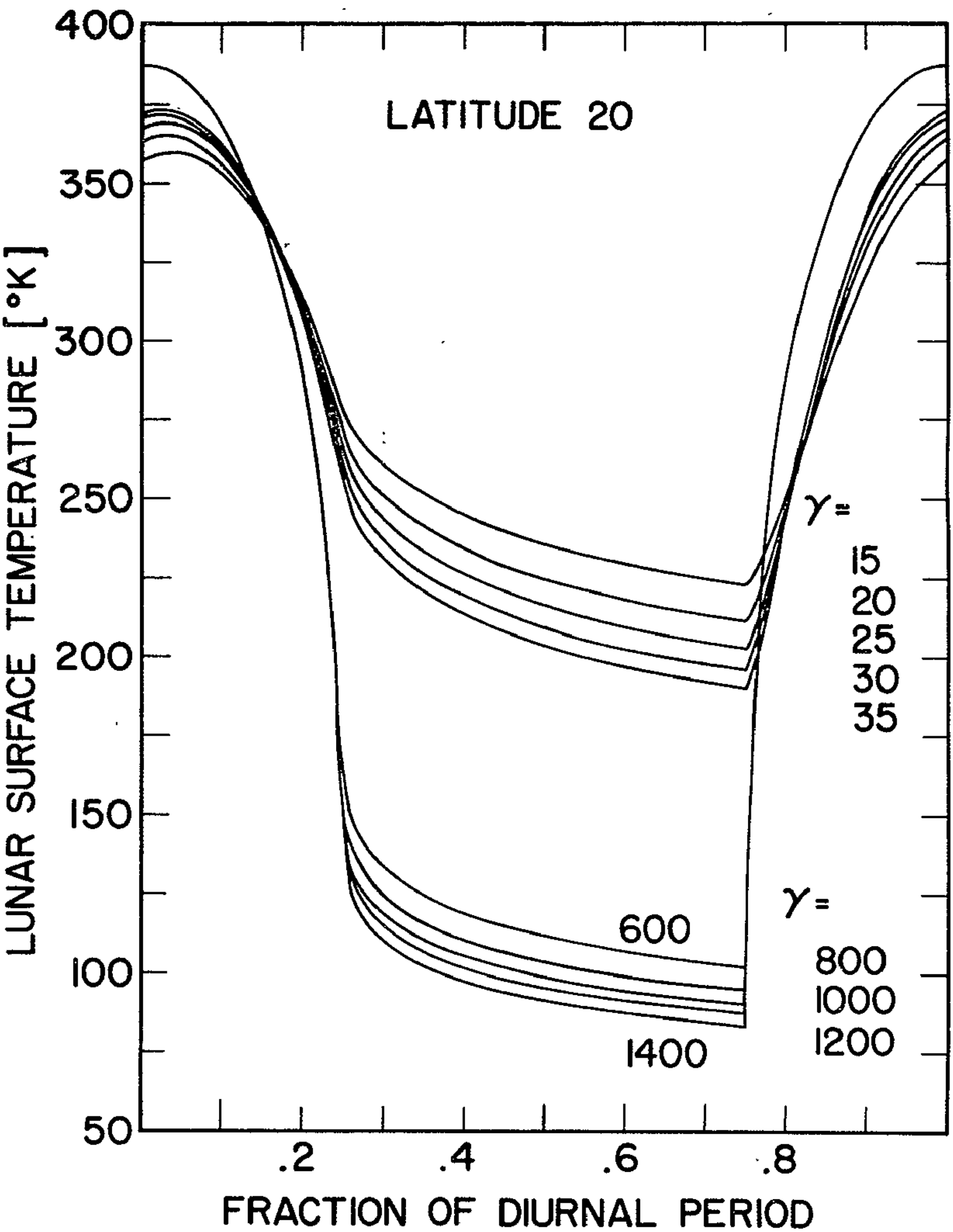

Figure 2.4. Lunation cooling solutions for SSLAT = 20°, and Gamma = 15,20,25,30,35,600,800,1000,1200, and 1400.

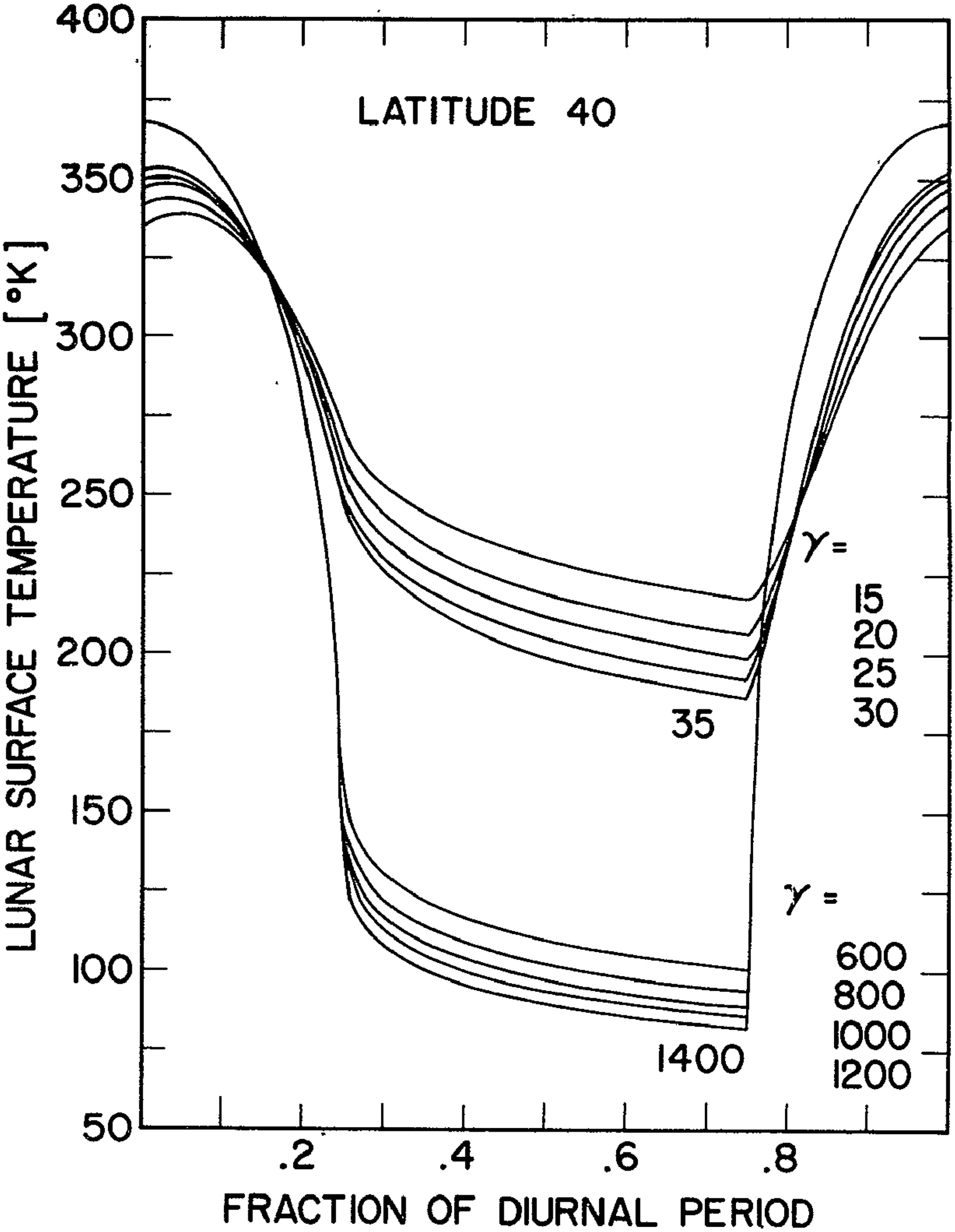

Figure 2.5. Lunation cooling solutions for SSLAT = 40°, and Gamma = 15,20,25,30,35,600,800,1000,1200, and 1400.

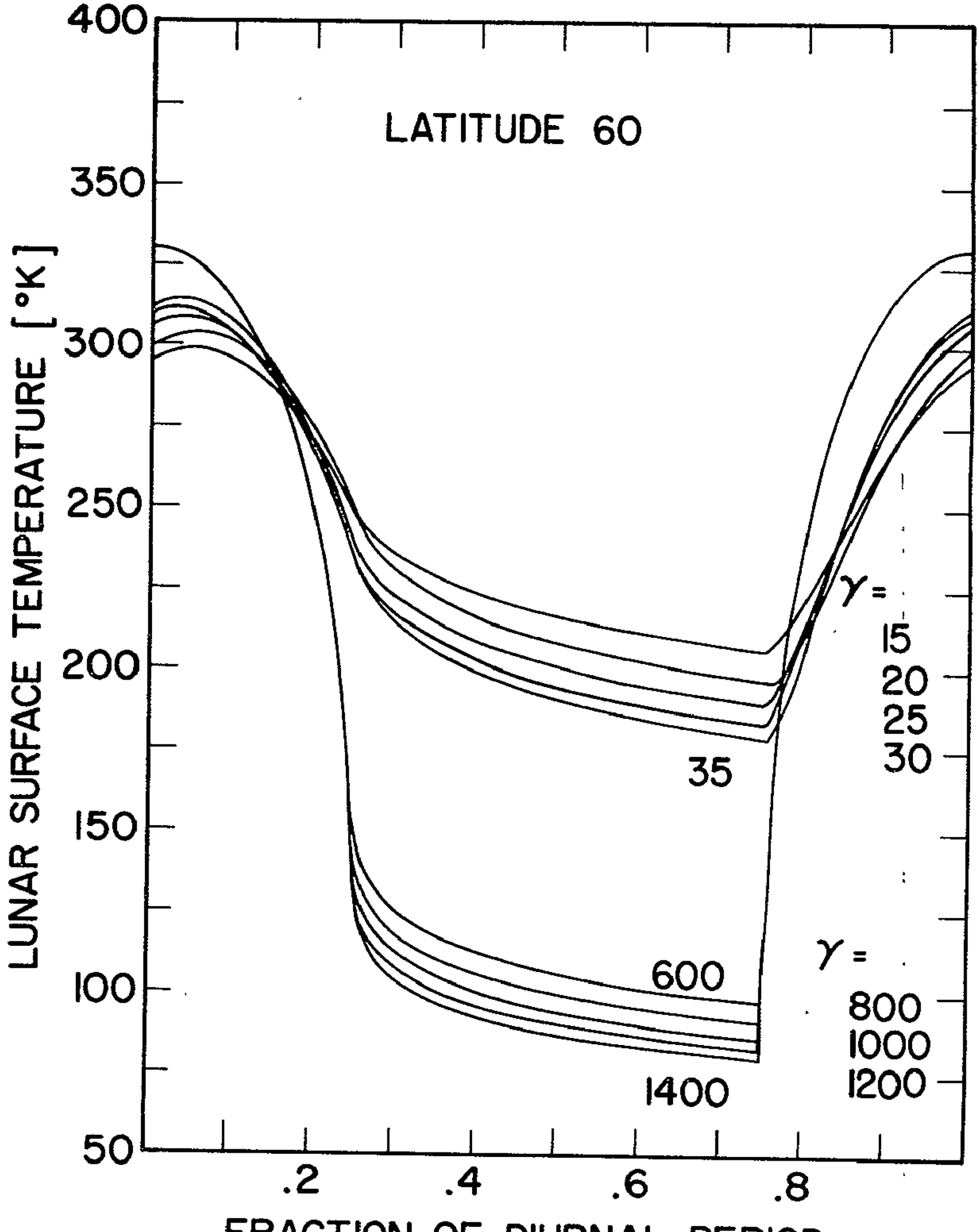

Figure 2.6. Lunation cooling solutions for SSLAT = 60°, and Gamma = 15,20,25,30,35,600,800,1000,1200, and 1400.

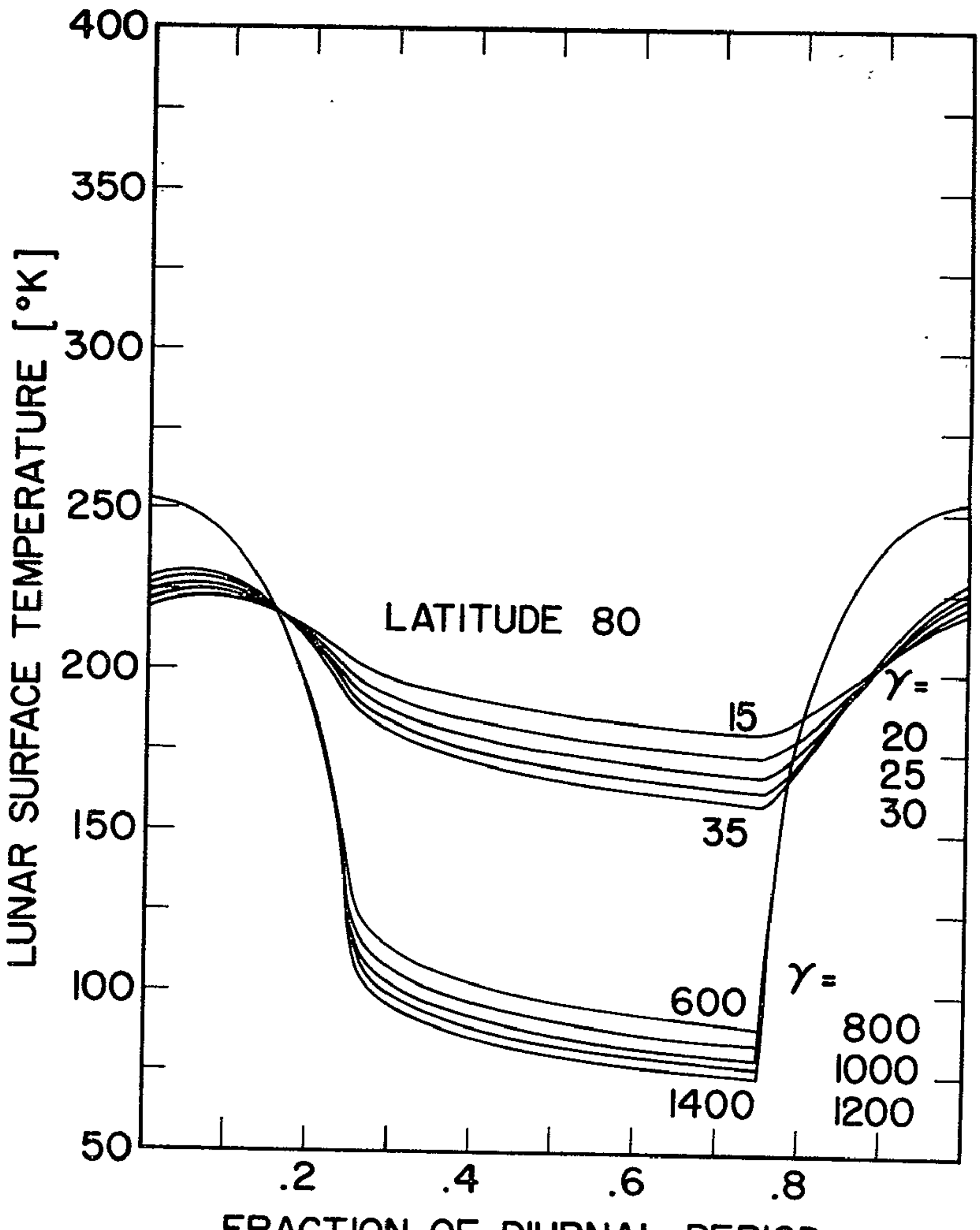

Figure 2.7. Lunation cooling solutions for SSLAT = 80°, and Gamma = 15,20,25,30,35,600,800,1000,1200, and 1400.

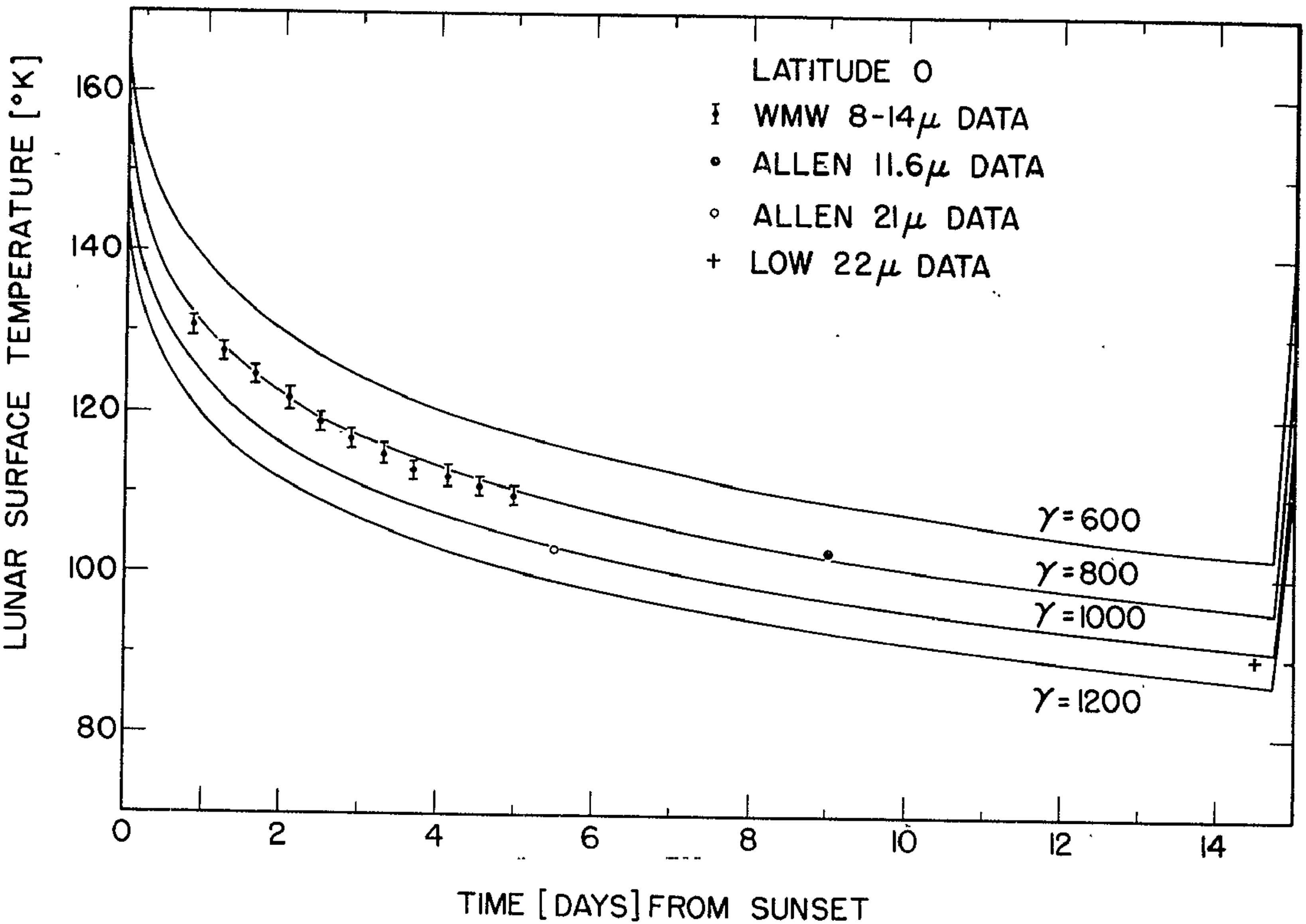

Figure 2.8. A comparison of nighttime cooling solutions for SSLAT = 0°, and Gamma = 600, 800, 1000, and 1200 with available infrared data.

Figure 2.8

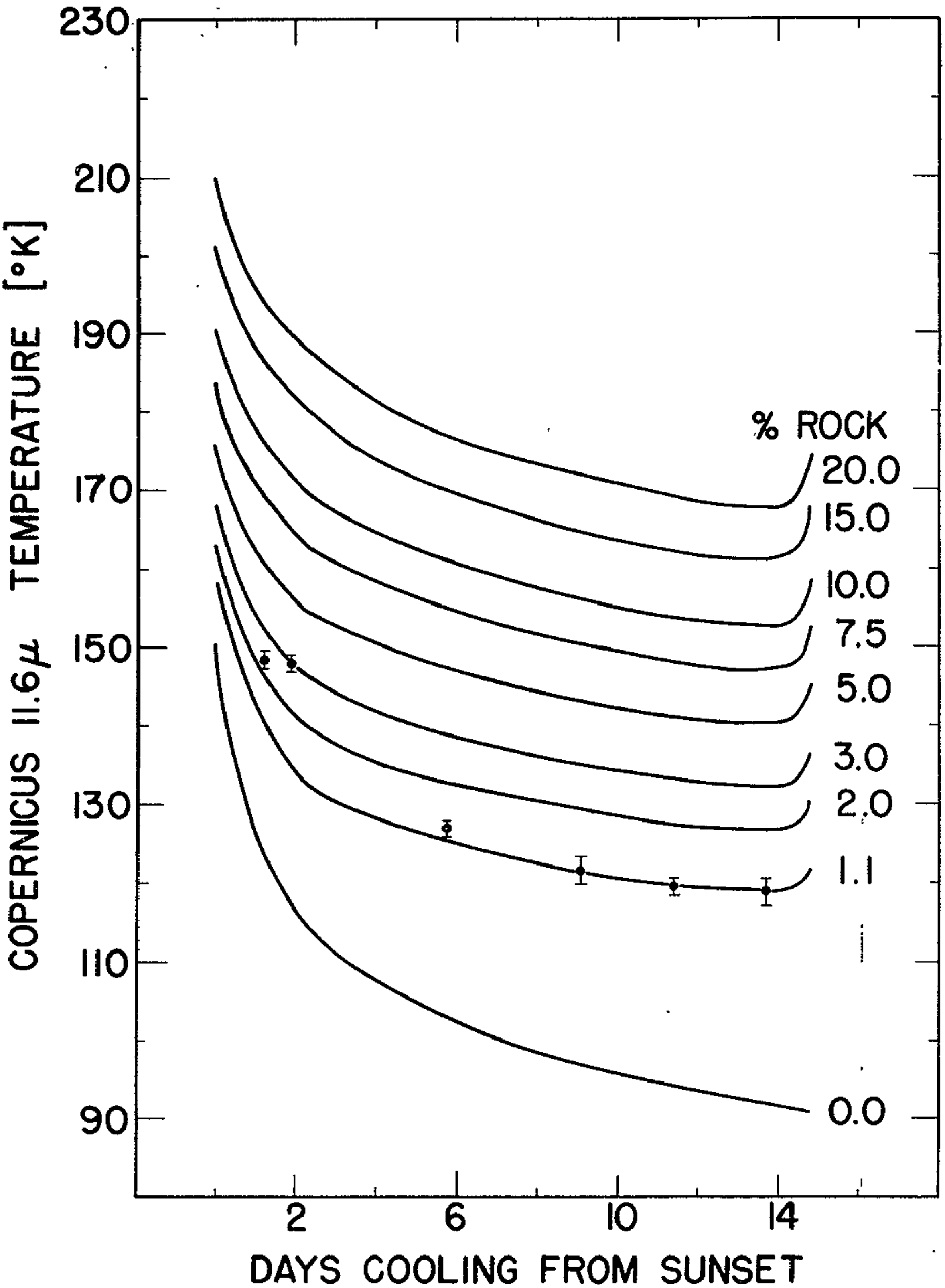

Figure 2.9. Copernicus crater model solutions compared to 12μ data of Allen and Ney.

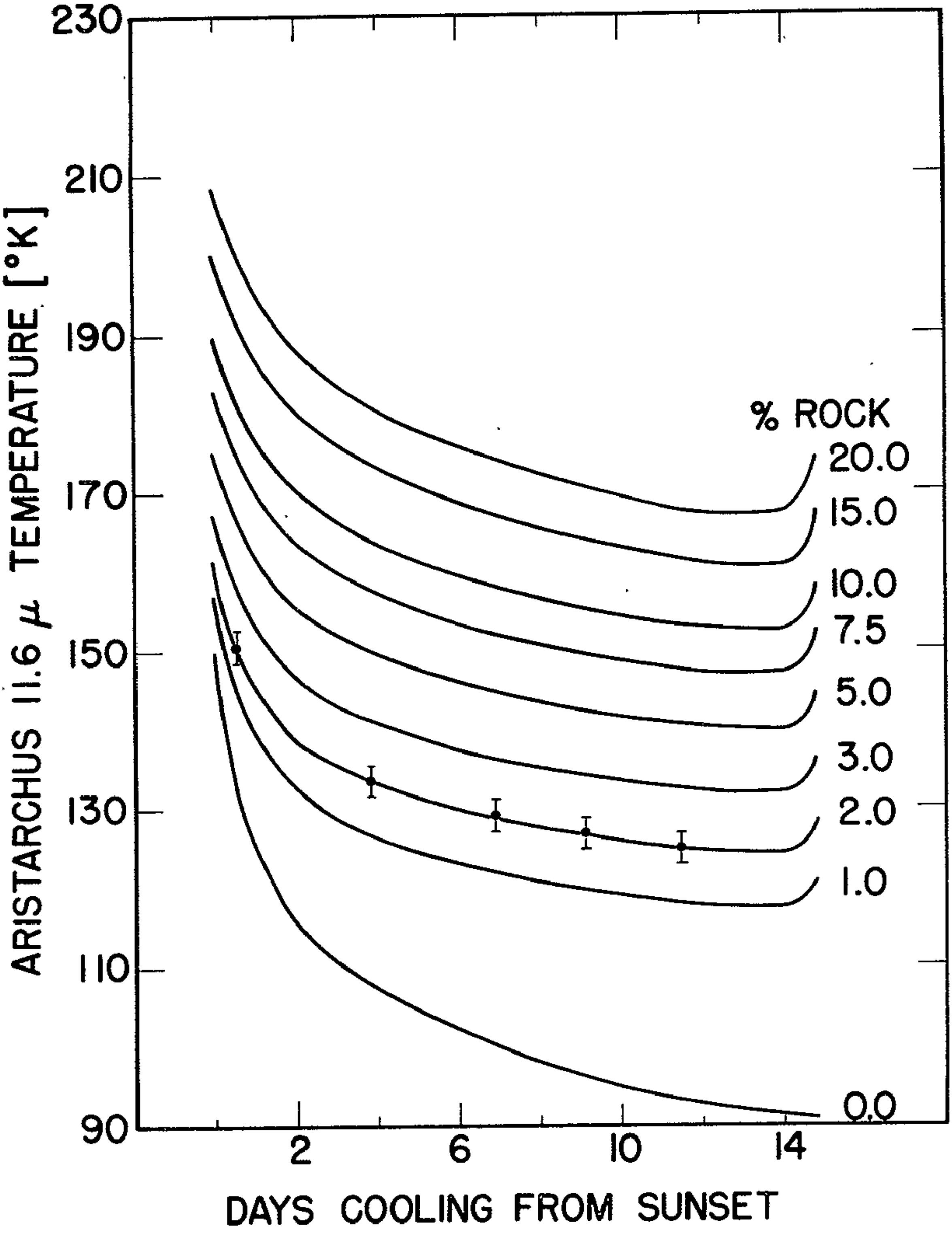

Figure 2.10. Aristarchus crater model solutions compared to the 12μ data of Allen and Ney.

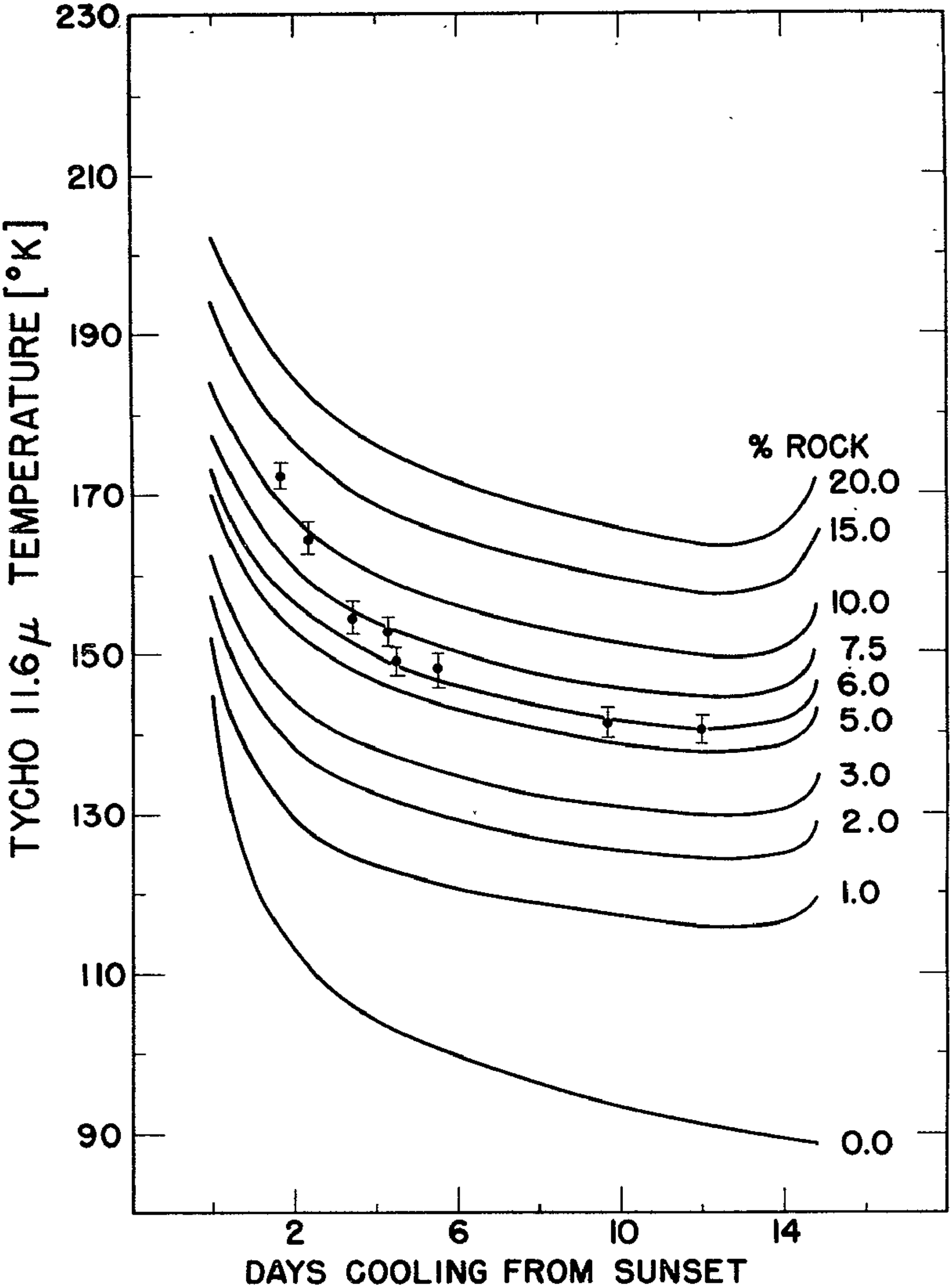

Figure 2.11. Tycho crater model solutions compared to the 12μ data of Allen and Ney.

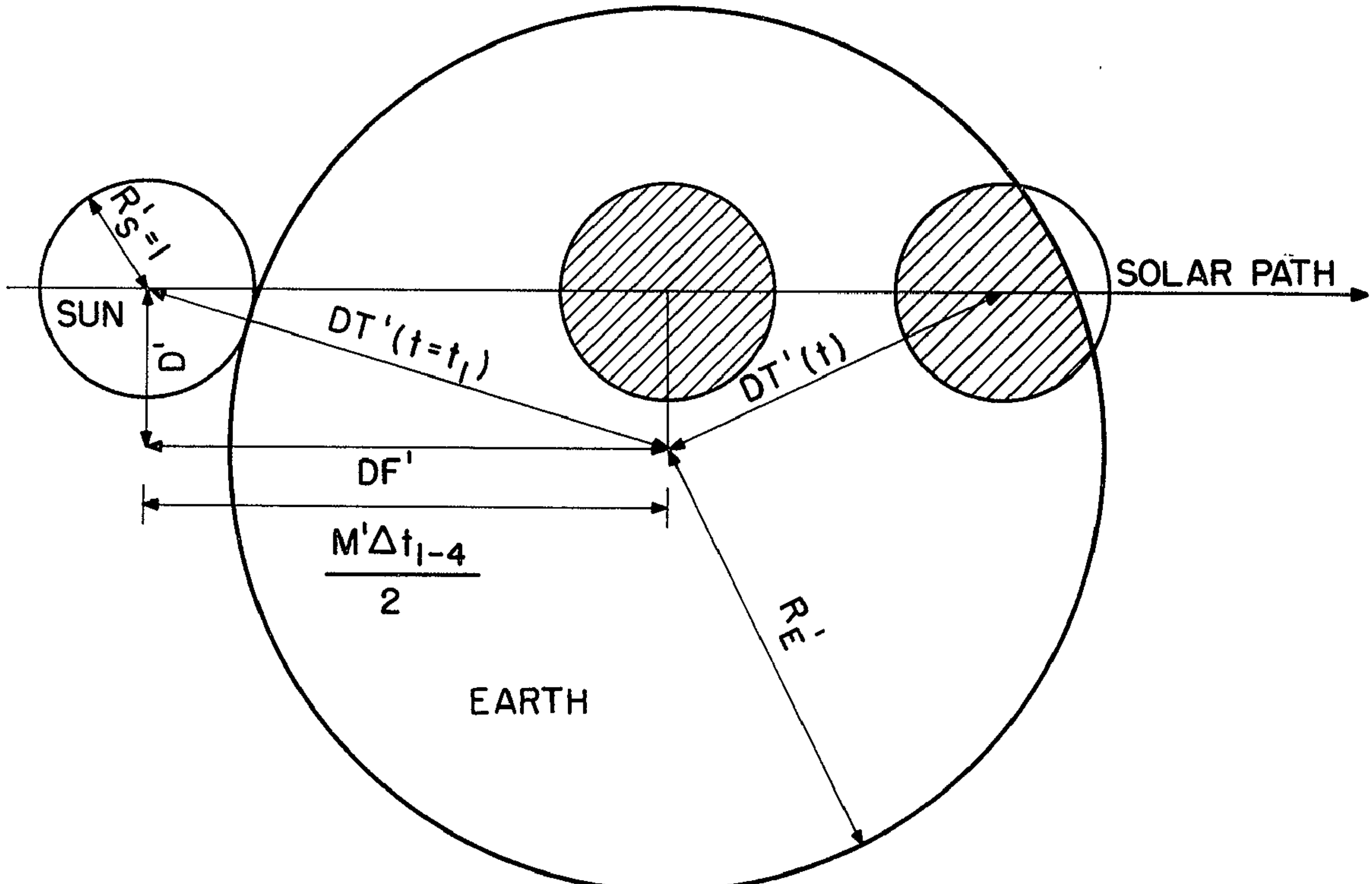

Figure 2.12. Lunar eclipse model.

Figure 2.12

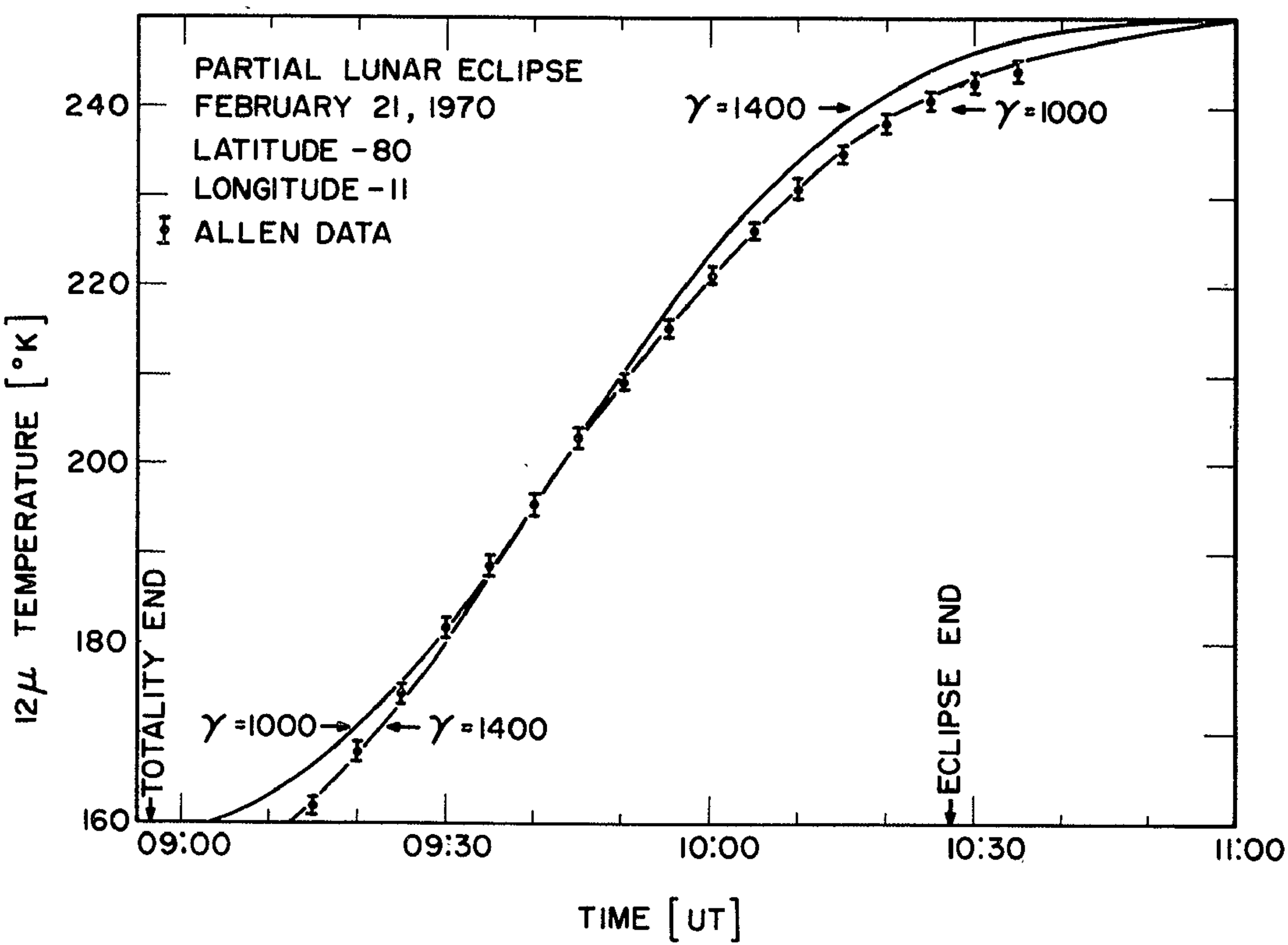

Figure 2.13. Partial lunar eclipse, February 21,1970, model solutions compared to the 12μ data of Allen.

Figure 2.13

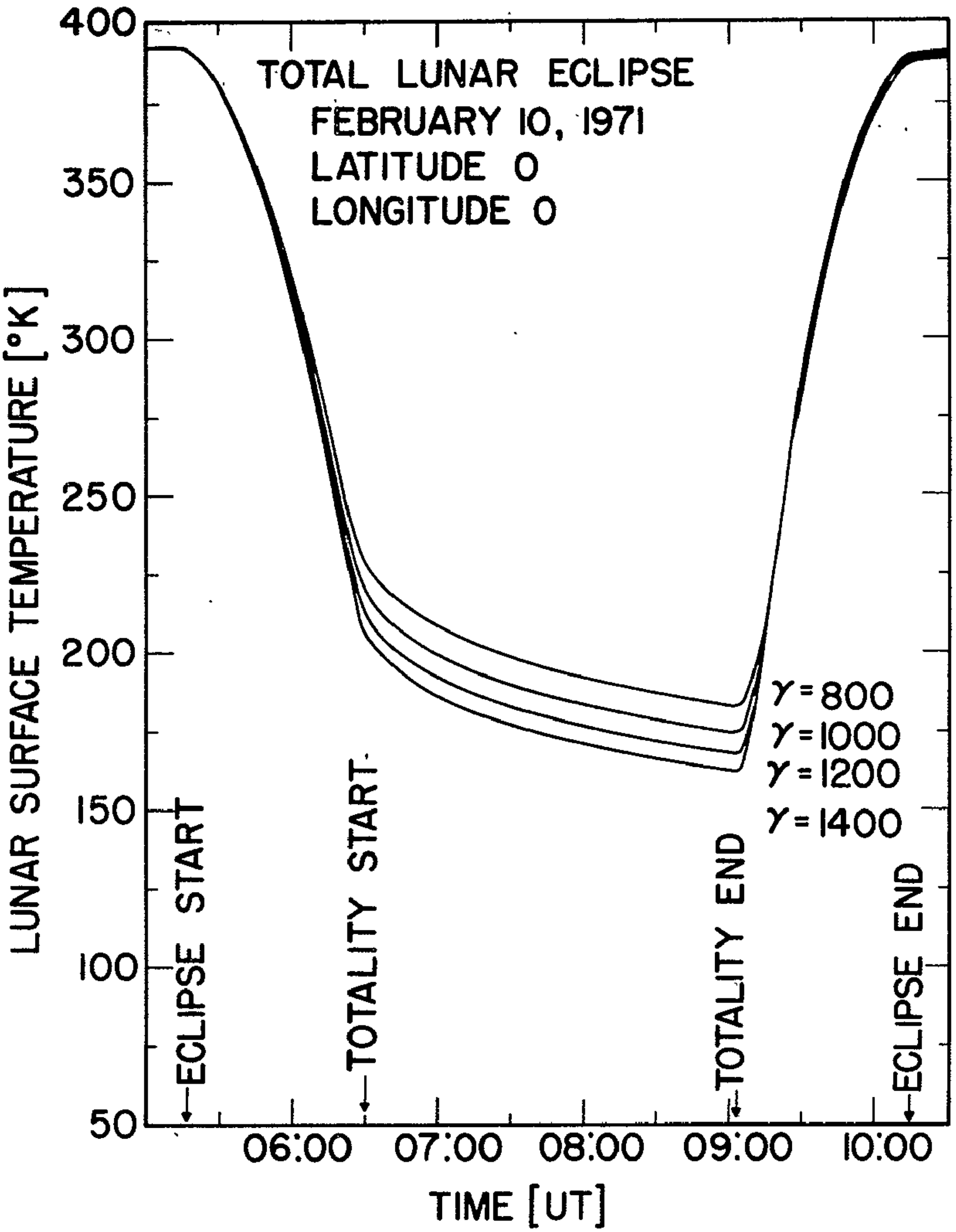

Figure 2.14. Total lunar eclipse, February 10,1971, central model solutions.

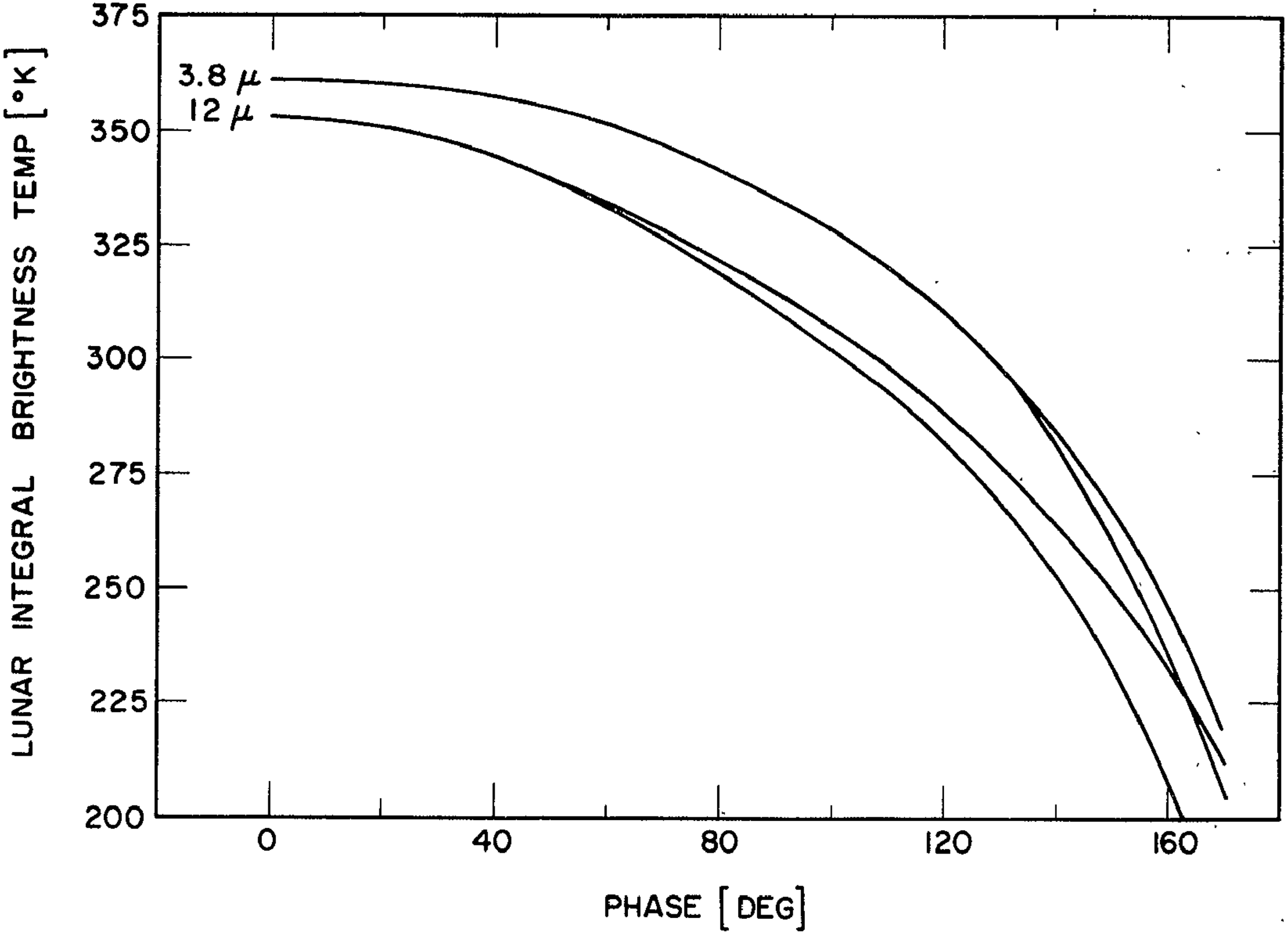

Figure 2.15. Day side lunar integral 3.8μ and 12μ solutions with phase.

Figure 2.15

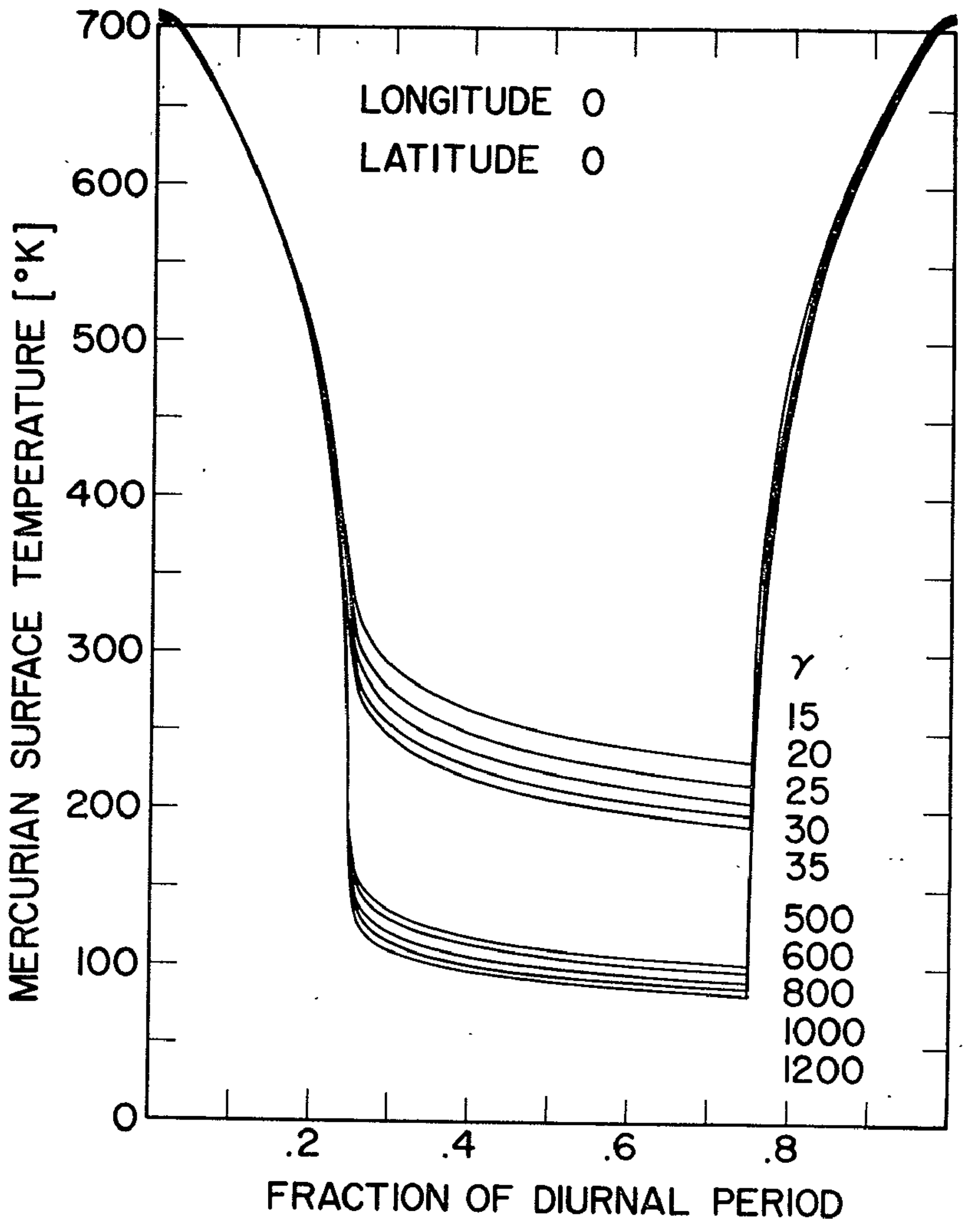

Figure 3.1. Mercurian diurnal cooling solutions for MLONG = 0°, MLAT = 0°, and Gamma = 15,20,25,30,35, 500,600,800,1000, and 1200.

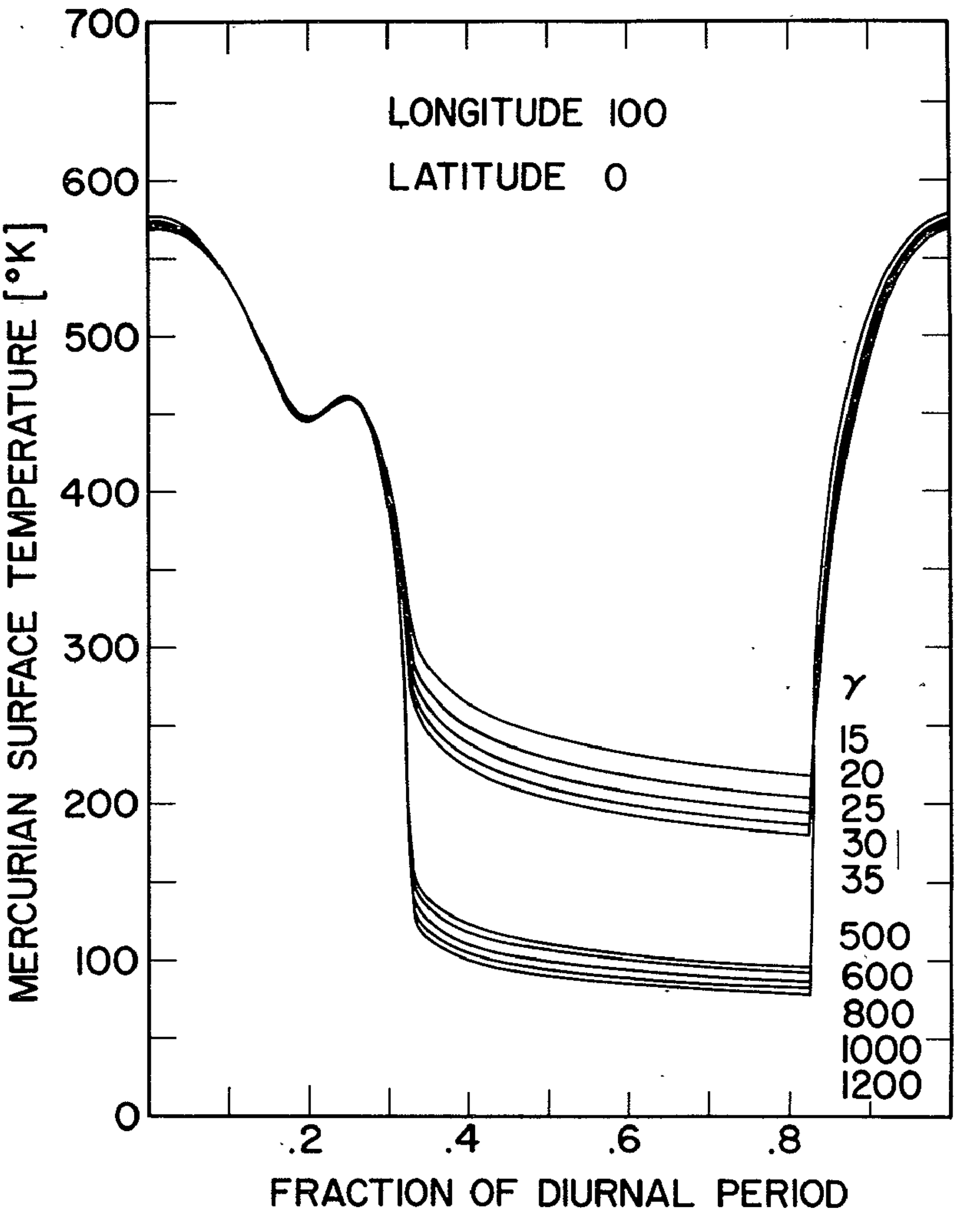

Figure 3.2. Mercurian diurnal cooling solutions for MLONG = 100°, MLAT = 0°, and Gamma = 15,20,25,30,35, 500,600,800,1000, and 1200.

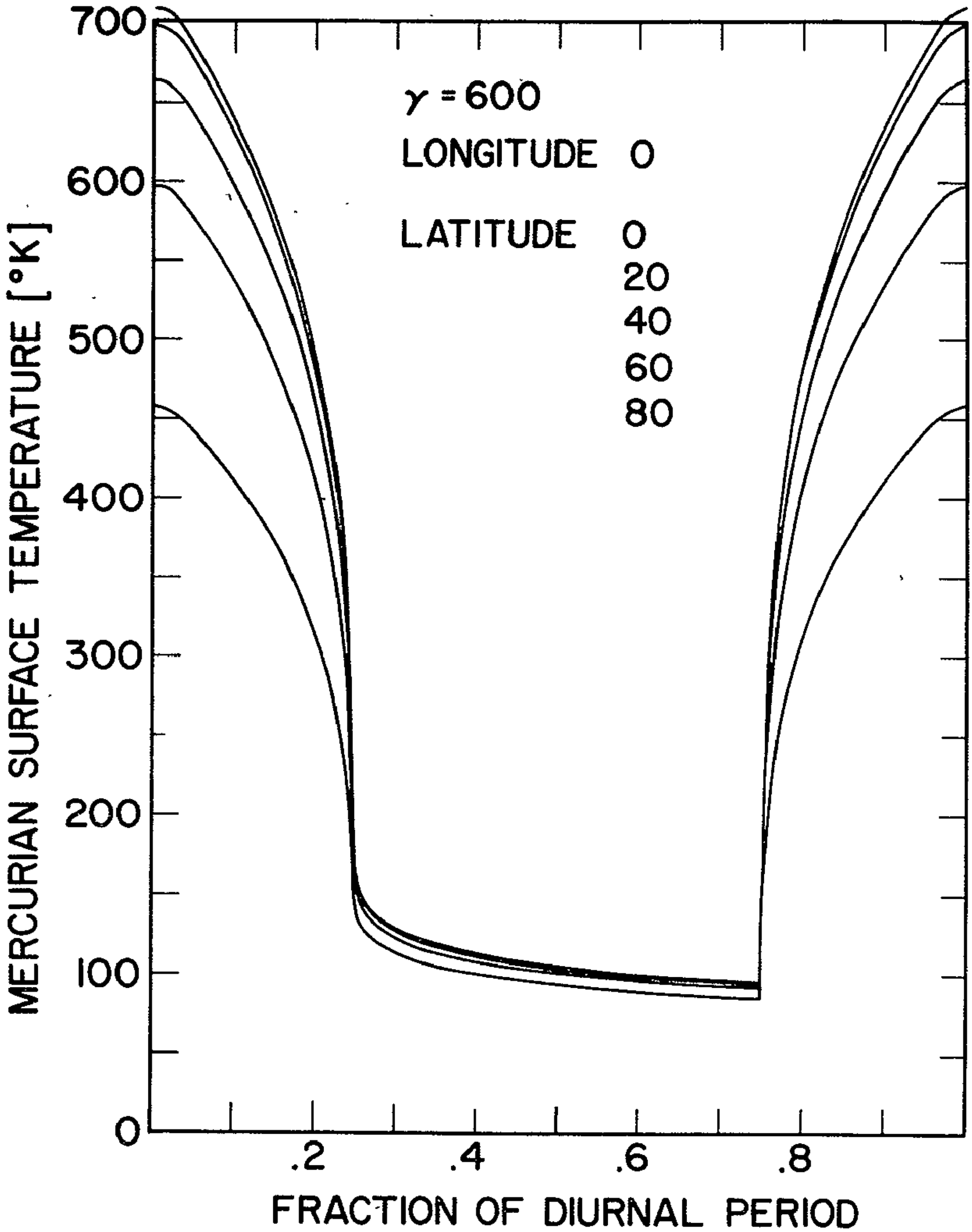

Figure 3.3. Mercurian diurnal cooling solutions for Gamma = 600, MLONG = 0°, and MLAT = 0°,20°,40°,60°,80°.

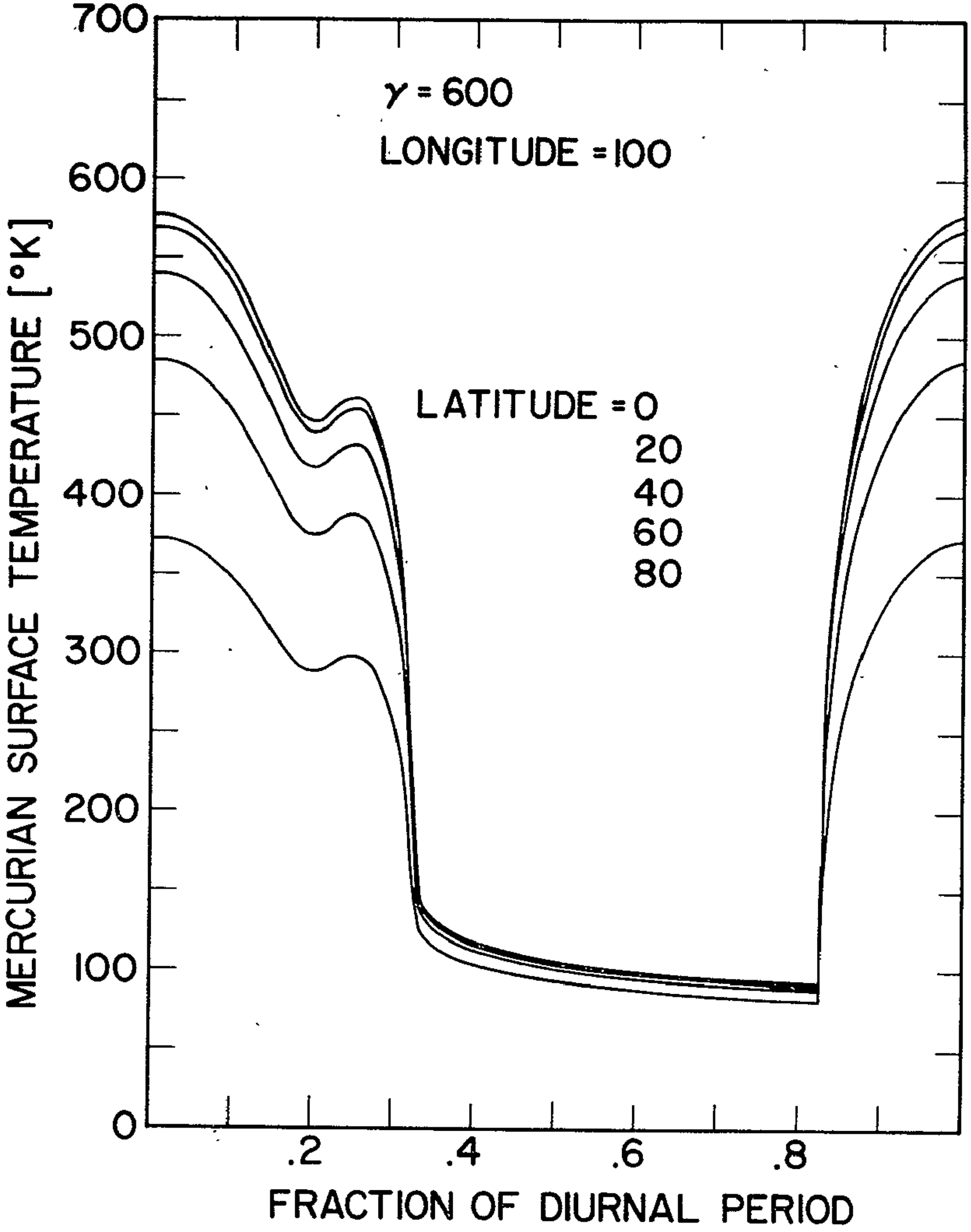

Figure 3.4. Mercurian diurnal cooling solutions for Gamma = 600, MLONG = 100°, and MLAT = 0°,20°,40°,60°,80.

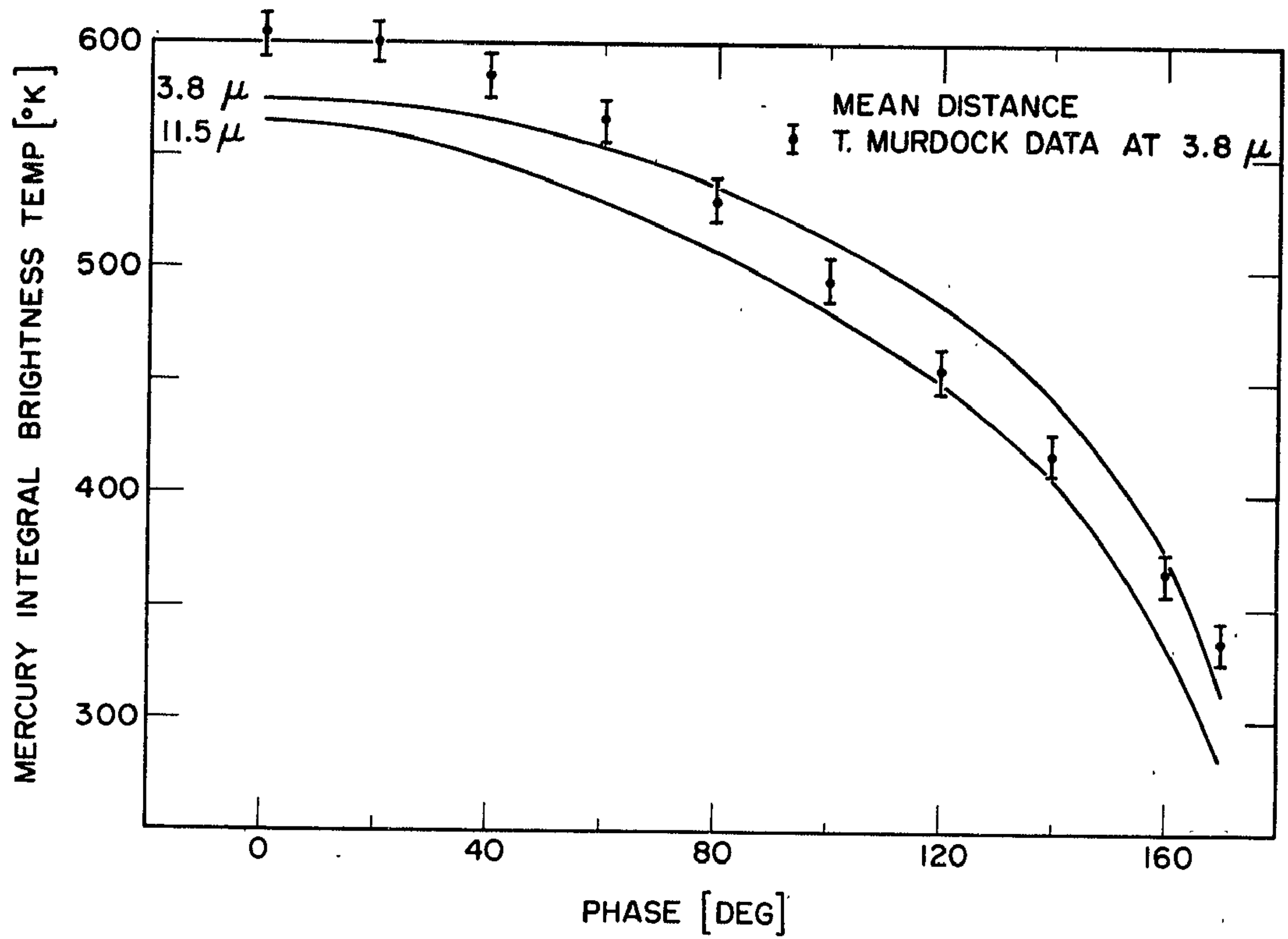

Figure 3.5. Day side mercurian integral 3.8μ and 11.5μ solutions with phase compared to the 3.8μ data of Murdock (1970) at mean distance.

Figure 3.5

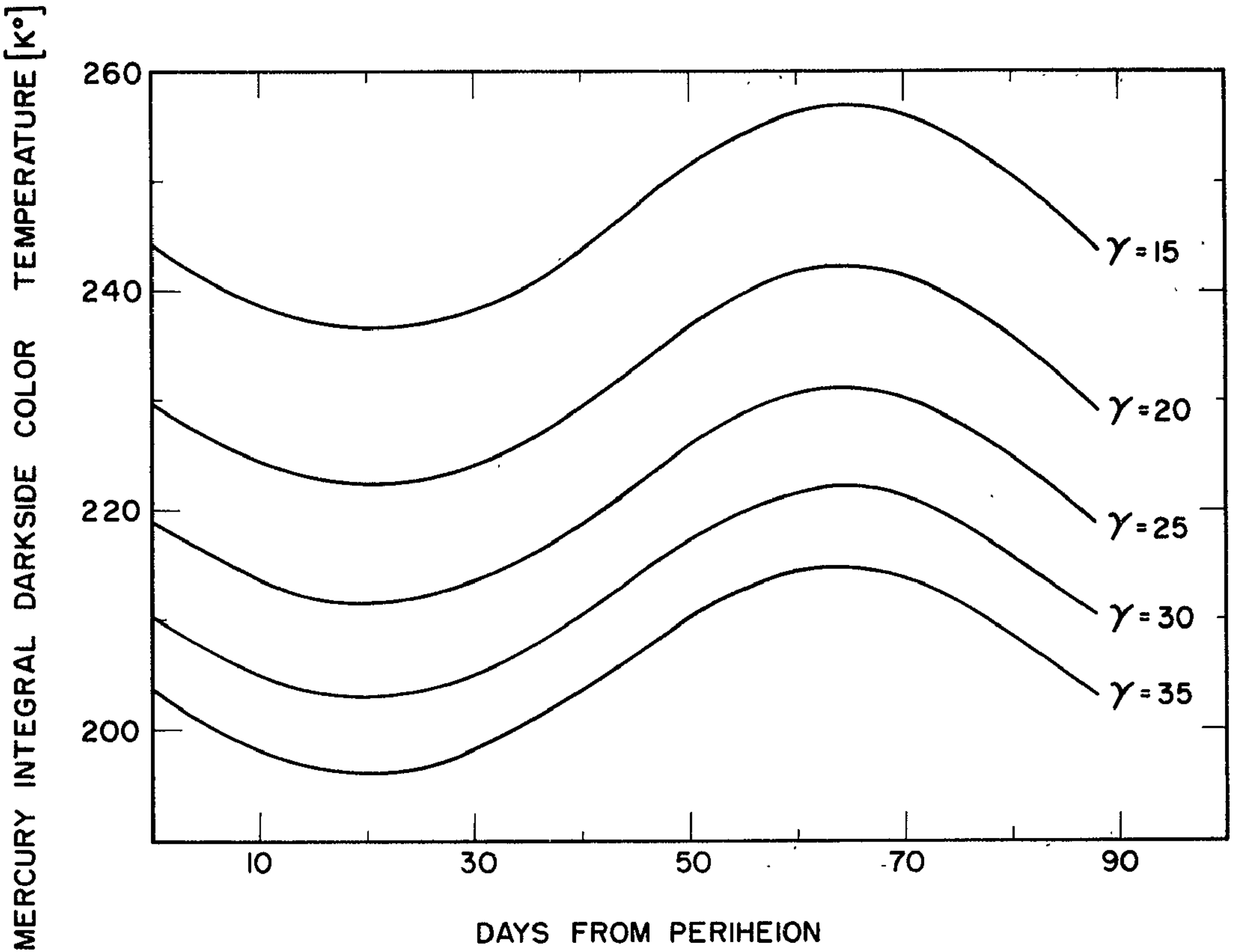

Figure 3.6. Mercurian dark side integral color temperature solutions for Gamma = 15,20,25,30, and 35 as a function of days from perihelion.

Figure 3.6

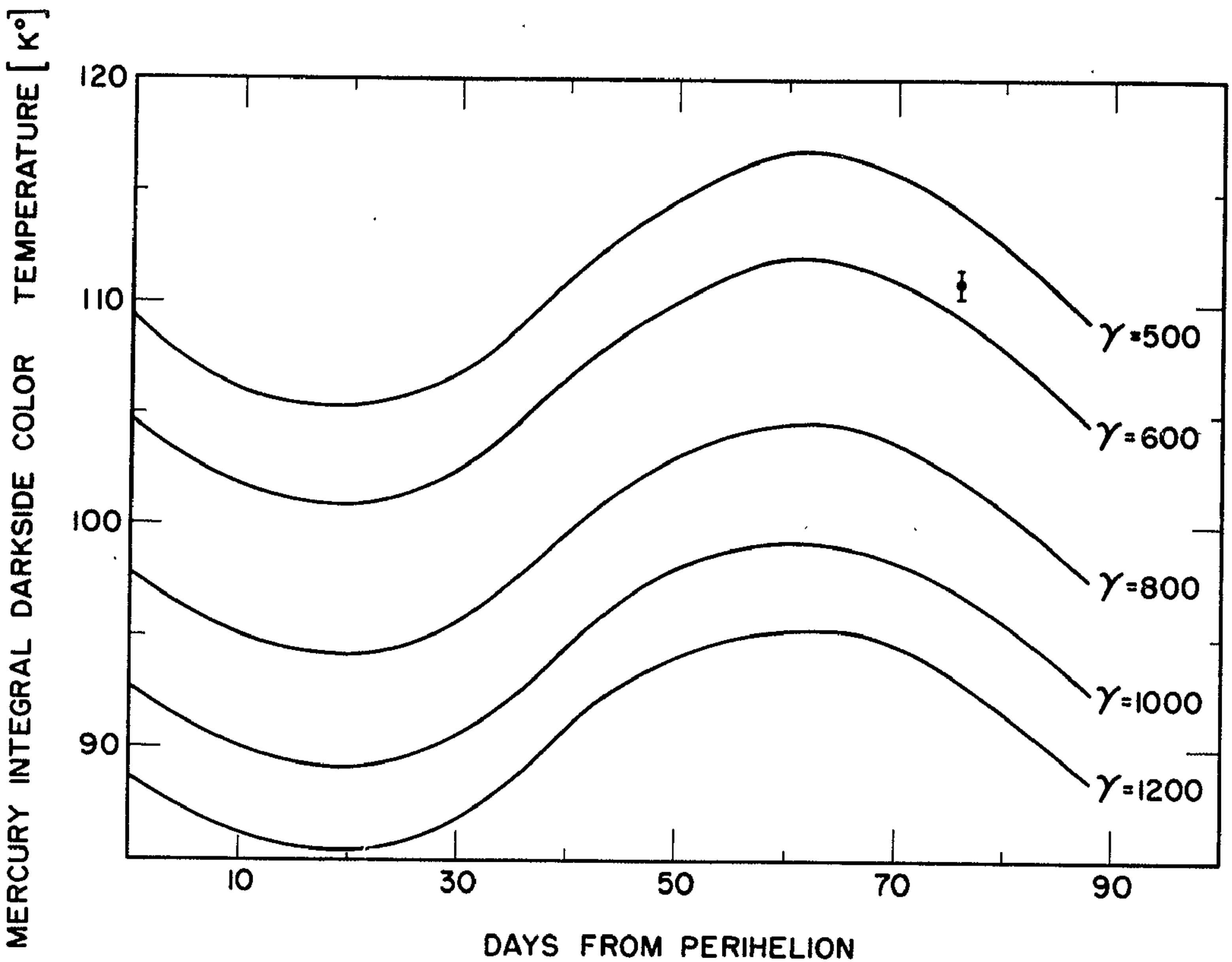

Figure 3.7. Mercurian dark side integral color temperature solutions for Gamma = 500,600,800,1000, and 1200 as a function of days from perihelion. Datum is that of Murdock and Ney (1970).

Figure 3.7

Figure 3.8

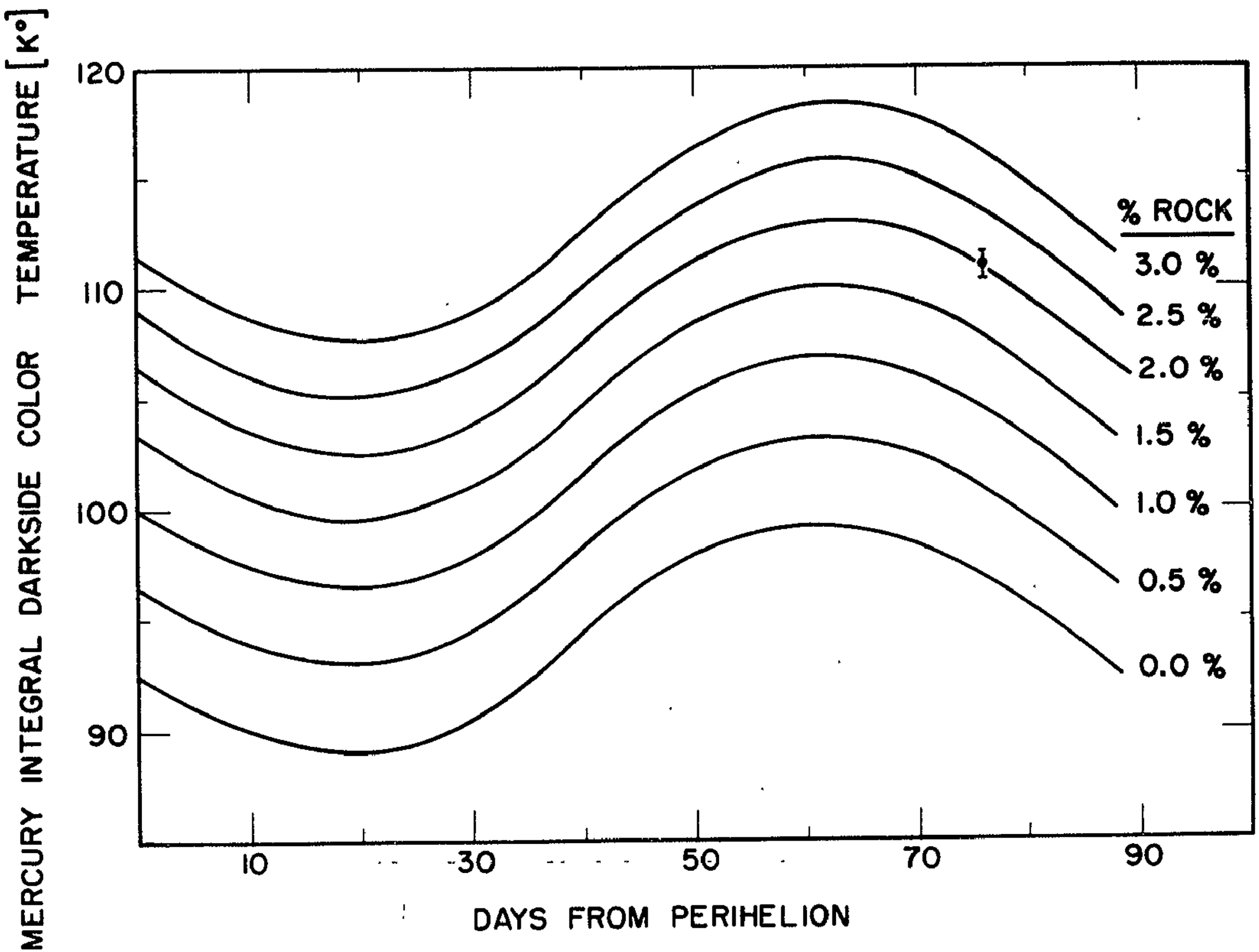

Figure 3.8. Mercurian dark side integral color temperature solutions for rock-dust model as a function of days from perihelion. Datum is that of Murdock and Ney(1970).

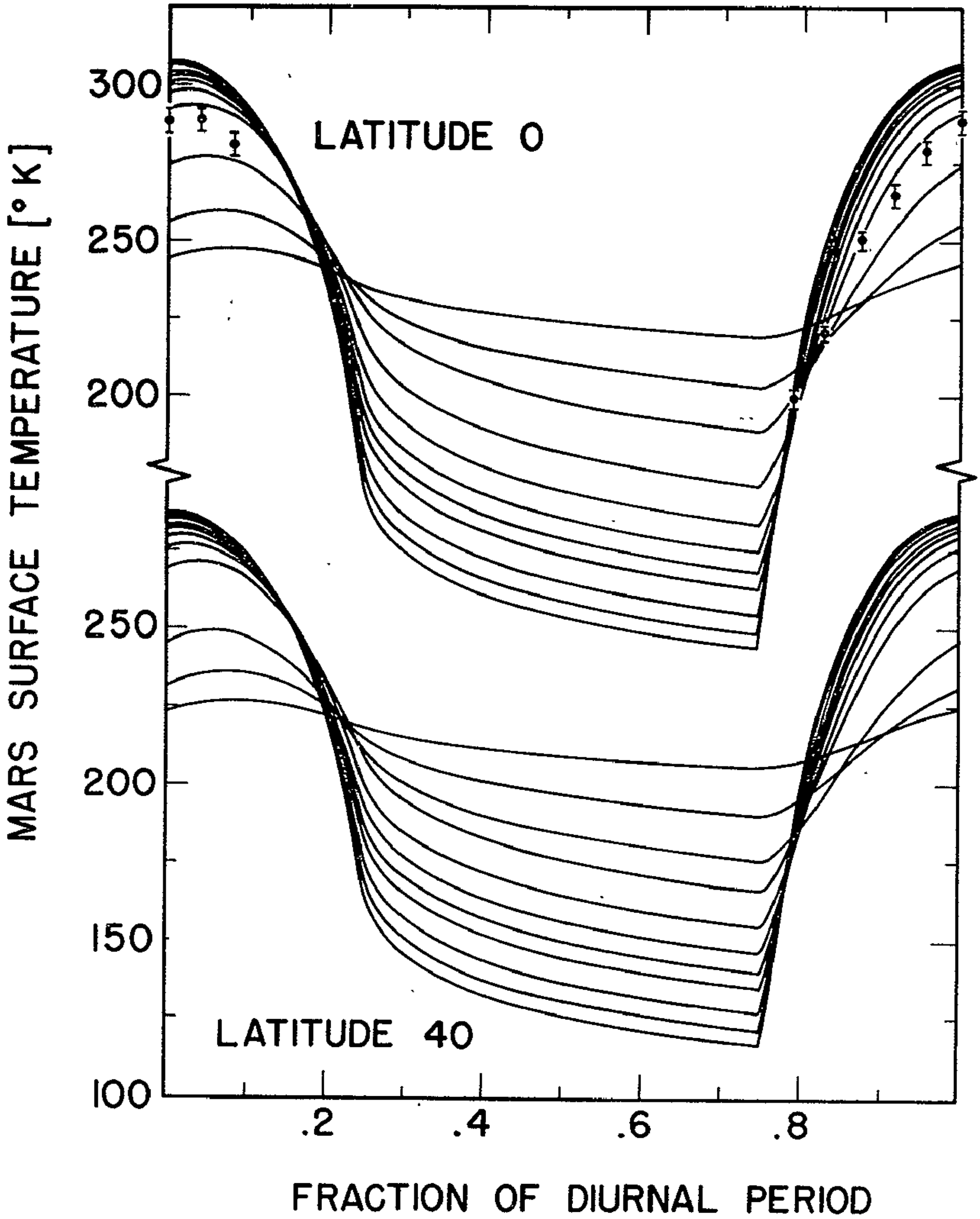

Figure 4.1. Mars diurnal cooling solutions for MLAT = 0°,40°, and Gamma = 20,50,100,200,300,400,500,600,800, 1000, and 1200. The data are those of Sinton and Strong (1960).

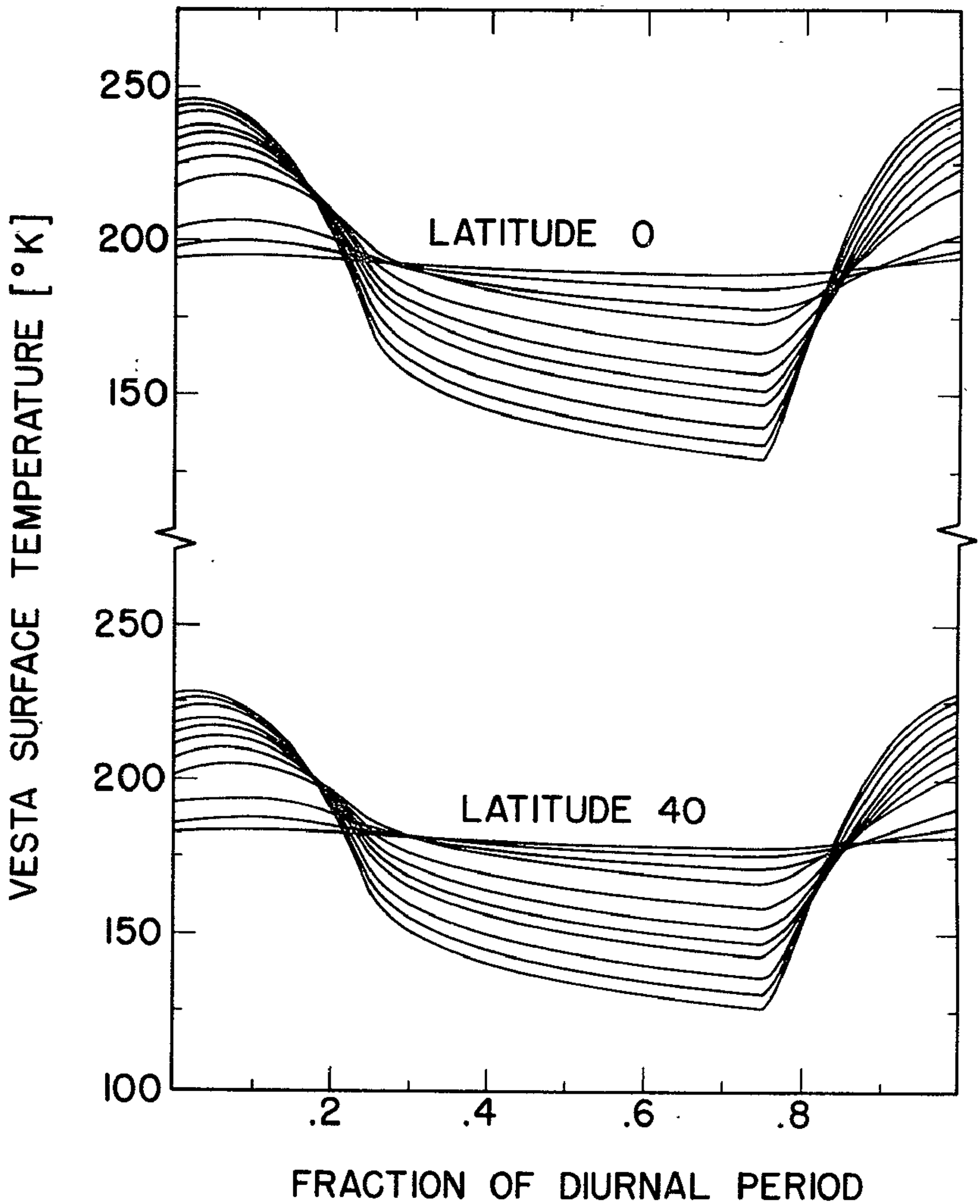

Figure 4.2. Vesta diurnal cooling solutions for MLAT = 0°,40°, and Gamma = 20,50,100,200,300,400,500,600,800, 1000, and 1200.

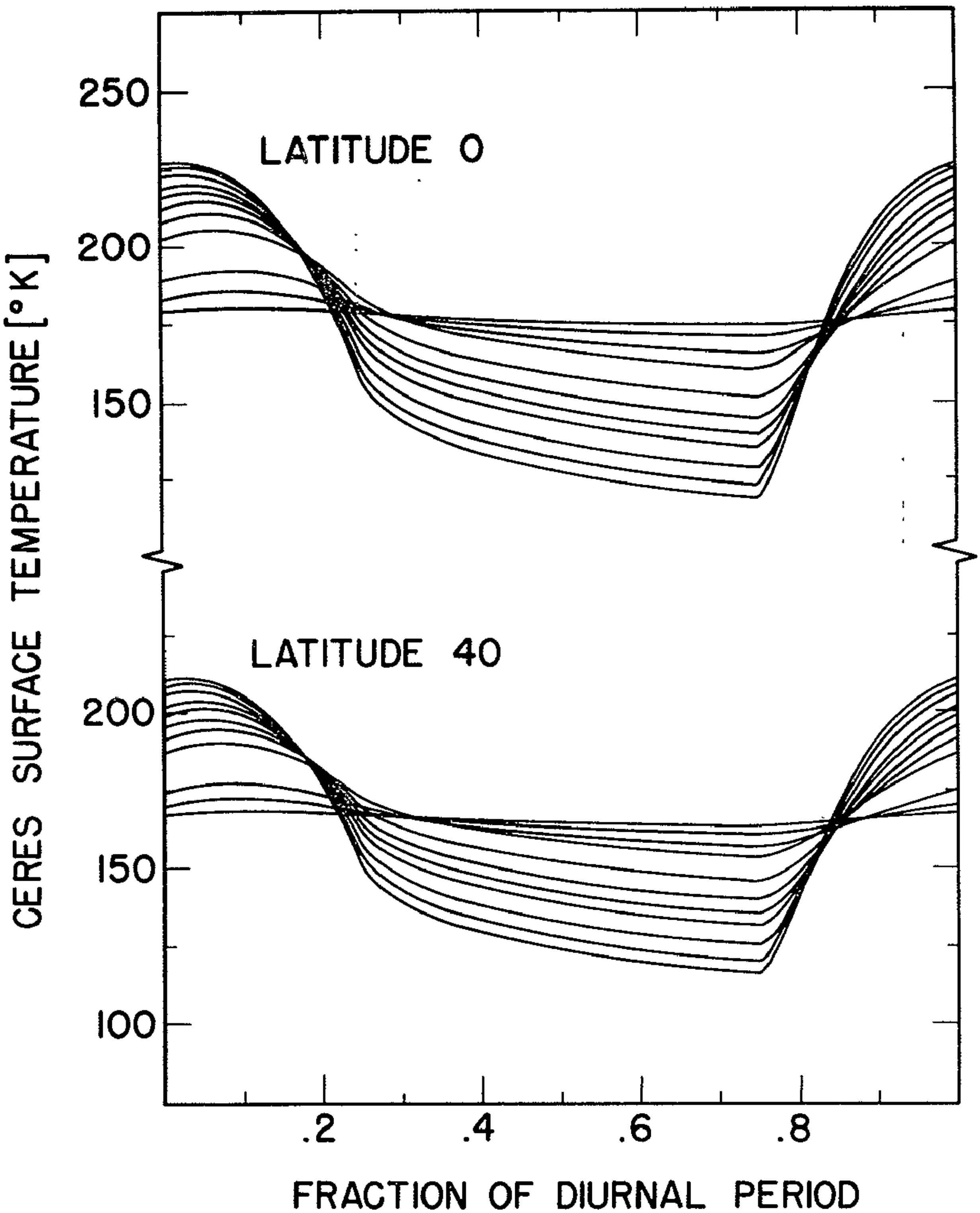

Figure 4.3. Ceres diurnal cooling solutions for MLAT = 0°,40°, and Gamma = 20,50,100,200,300,400,500,600,800, 1000, and 1200.

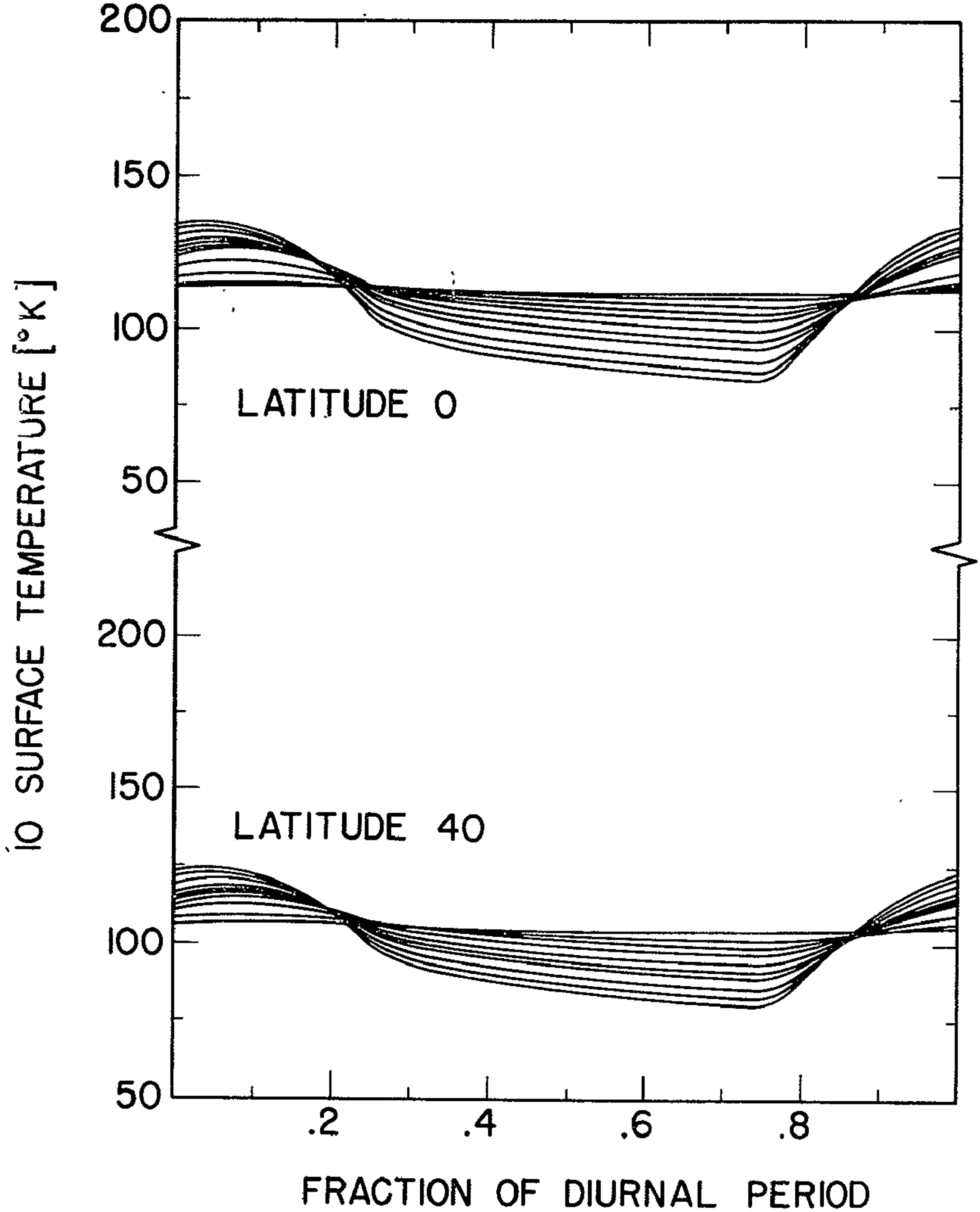

Figure 4.4. Io diurnal cooling solutions for MLAT = 0°,40°, and Gamma = 20,50,100,200,300,400,500,600,800, 1000, and 1200.

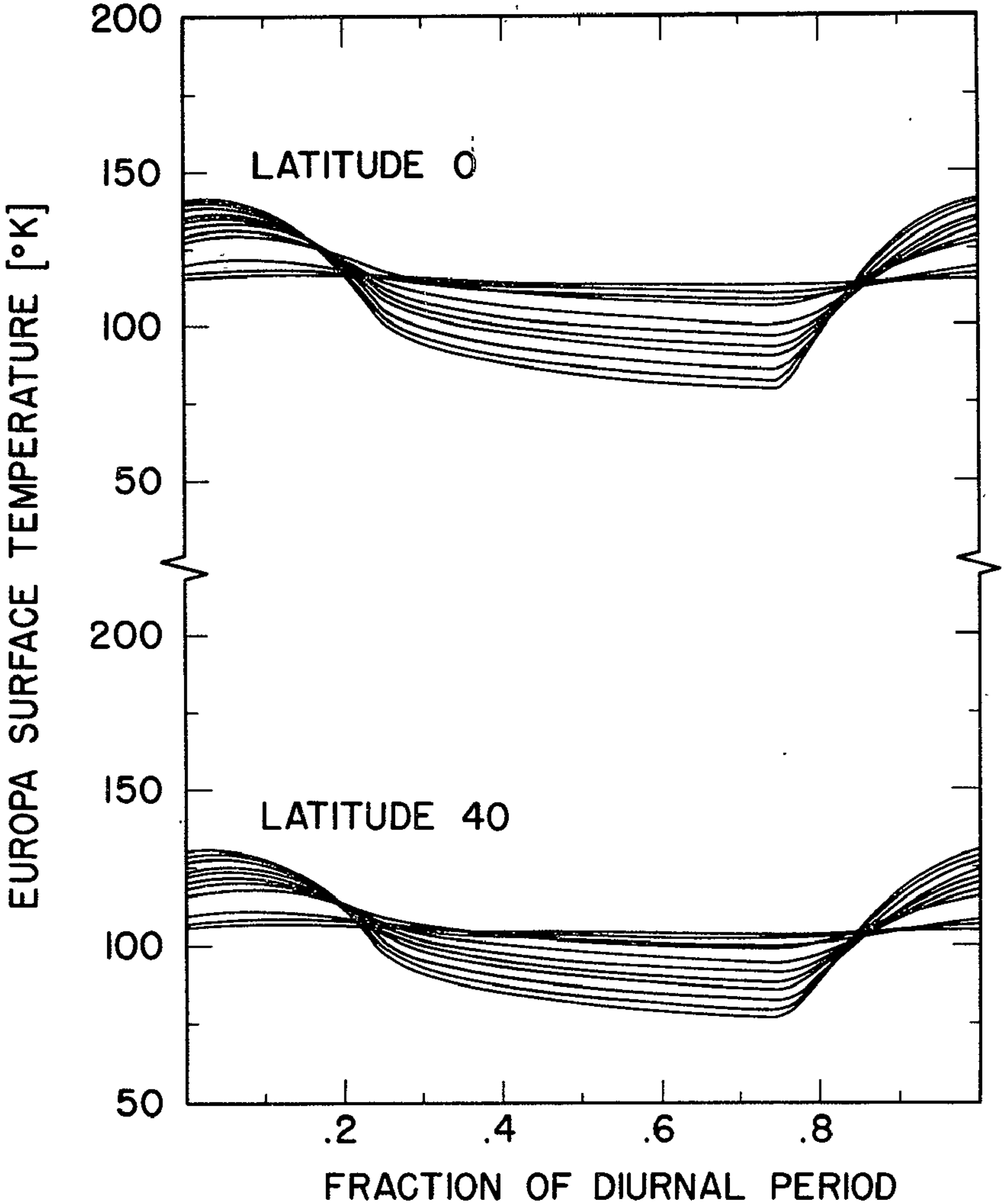

Figure 4.5. Europa diurnal cooling solutions for MLAT = 0°,40°, and Gamma = 20,50,100,200,300,400,500,600,800, 1000, and 1200.

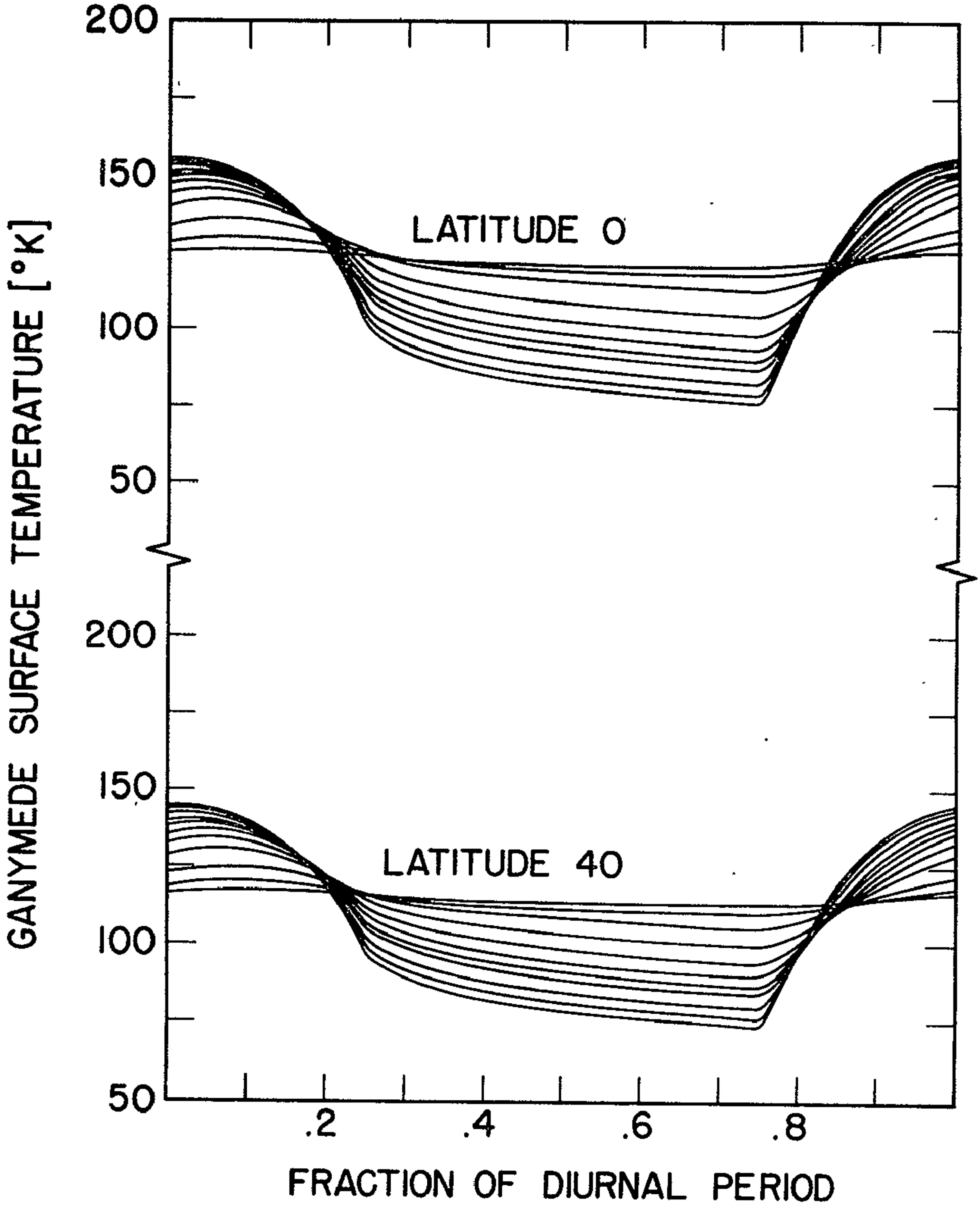

Figure 4.6. Ganymede diurnal cooling solutions for MLAT = 0°,40°, and Gamma = 20,50,100,200,300,400,500,600,800, 1000, and 1200.

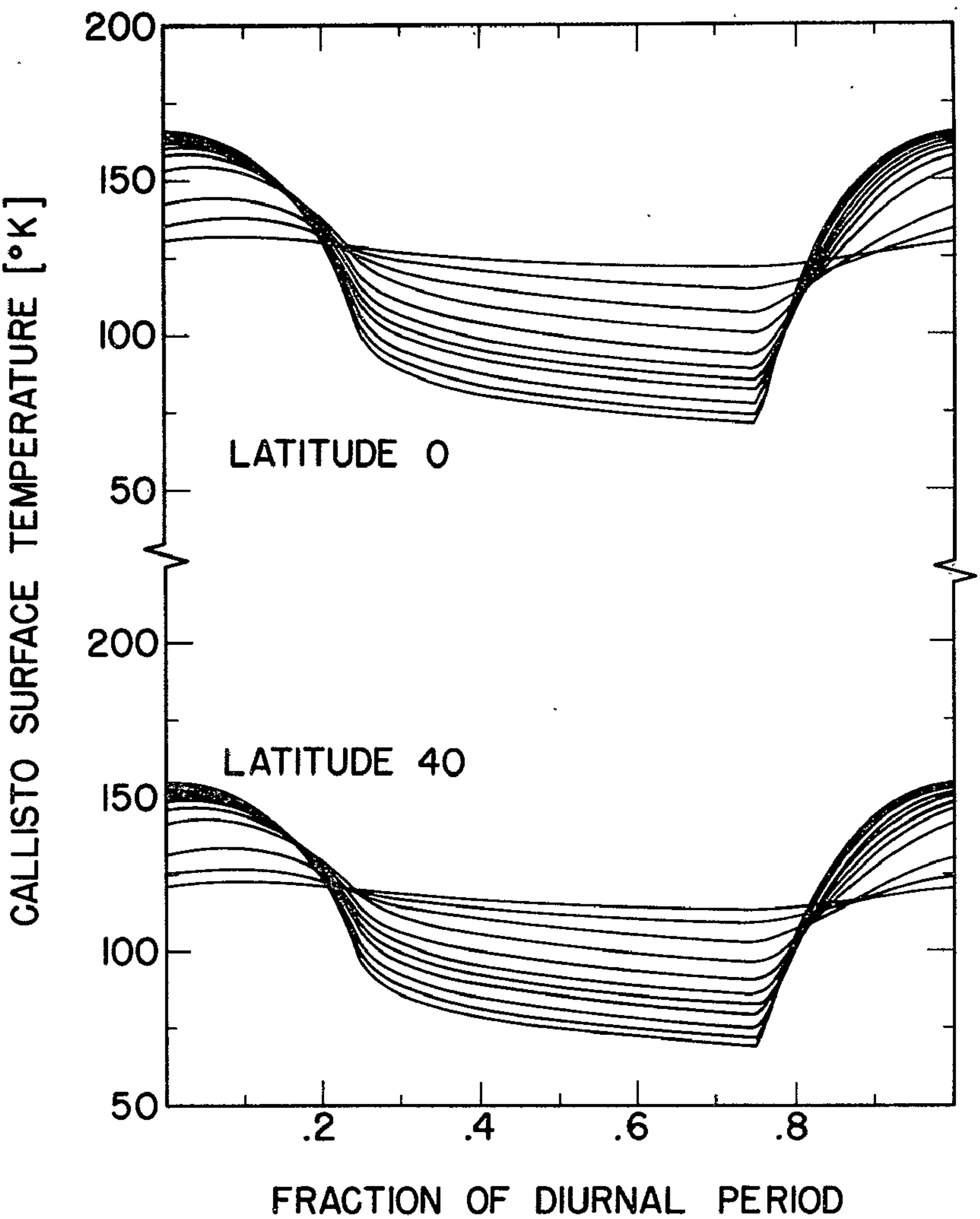

Figure 4.7. Callisto diurnal cooling solutions for MLAT = 0°,40°, and Gamma = 20,50,100,200,300,400,500, 600,800,1000, and 1200.

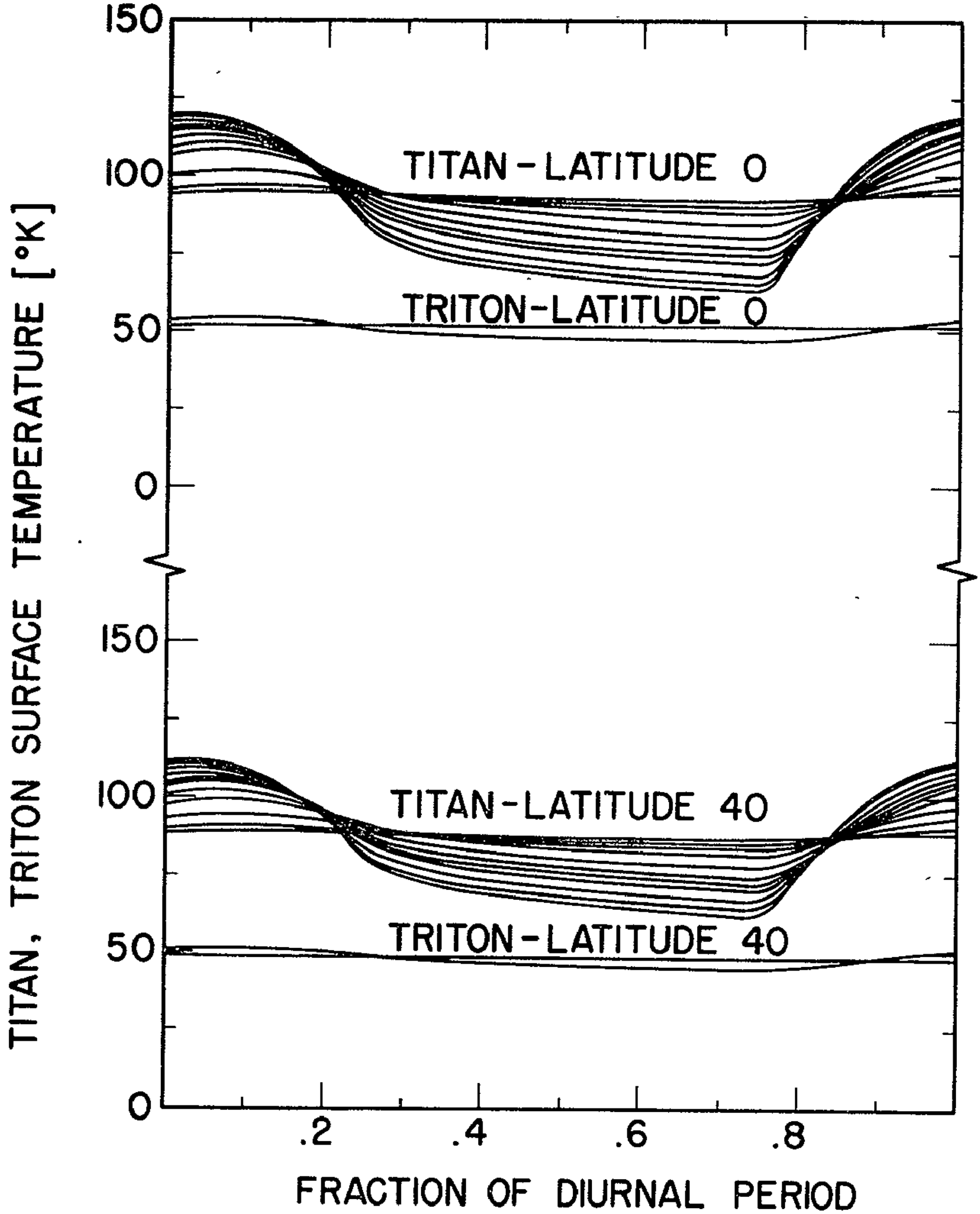

Figure 4.8. Titan, Triton diurnal cooling solutions for MLAT = 0°,40°, and Gamma = 20,50,100,200,300,400,500,600, 800,1000, and 1200.

Figure 4.9

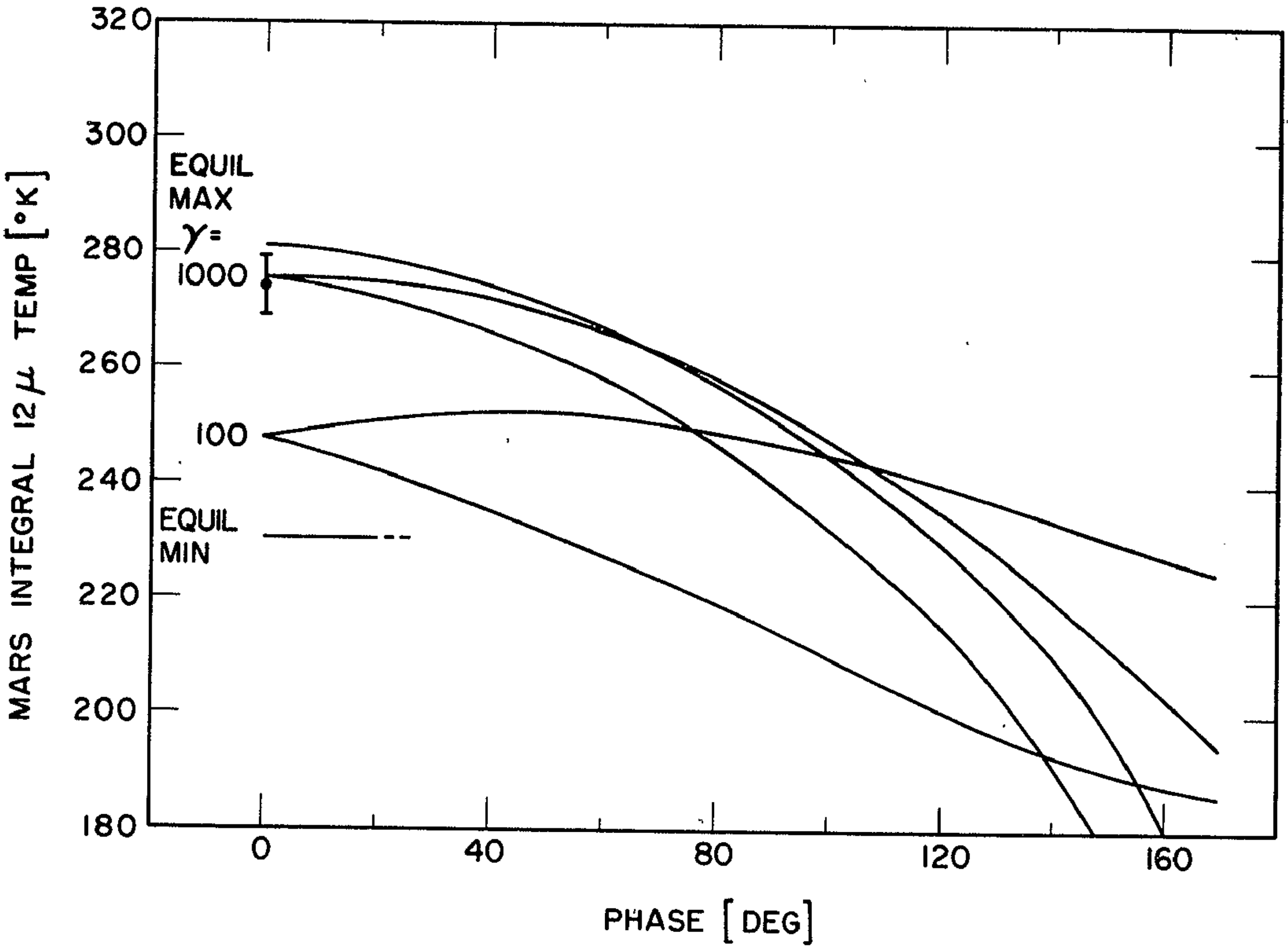

Figure 4.9. Mars day side integral 12μ solutions as a function of Gamma and phase. The datum is that of Murdock.

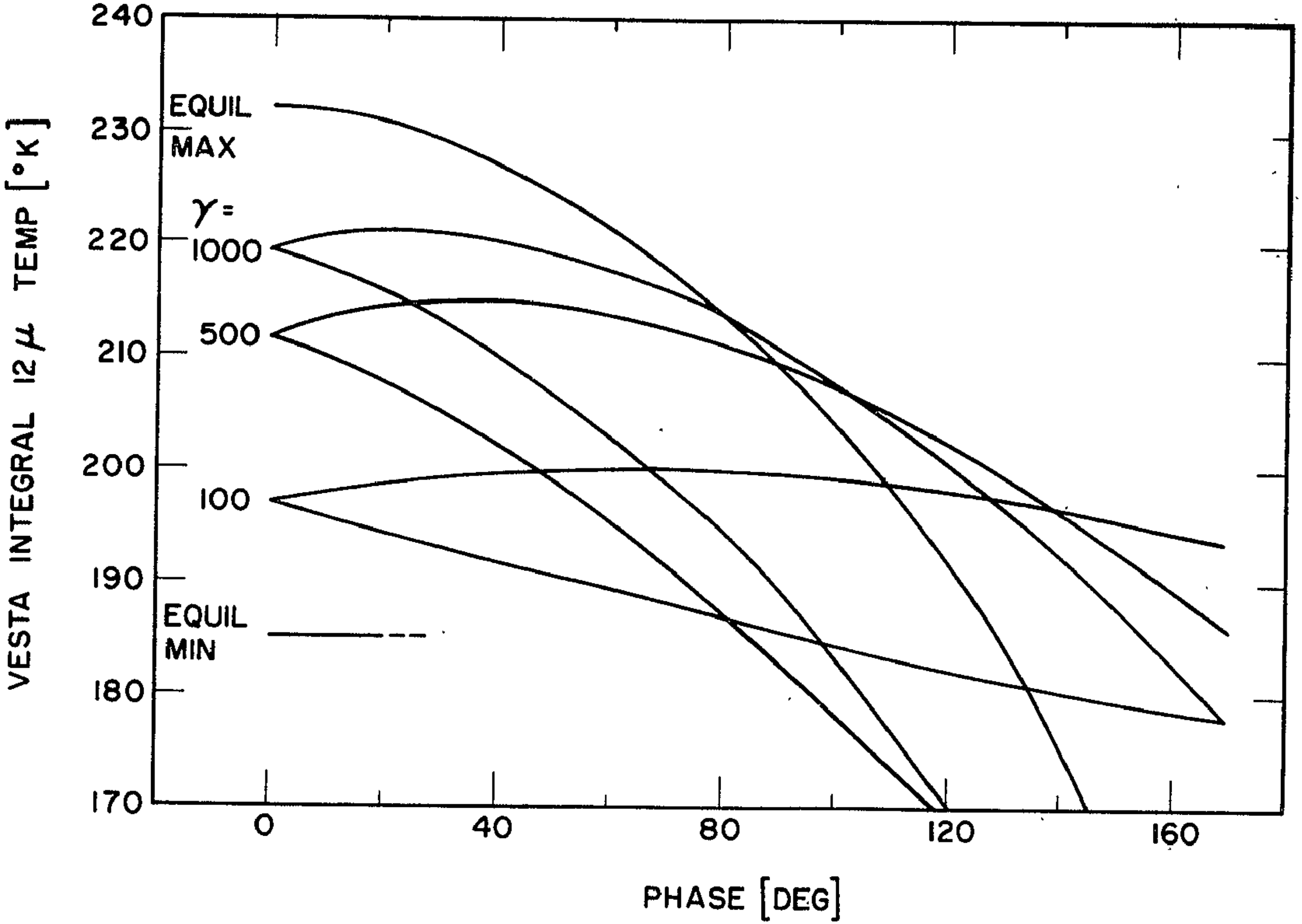

Figure 4.10. Vesta day side integral 12μ solutions as a function of Gamma and phase.

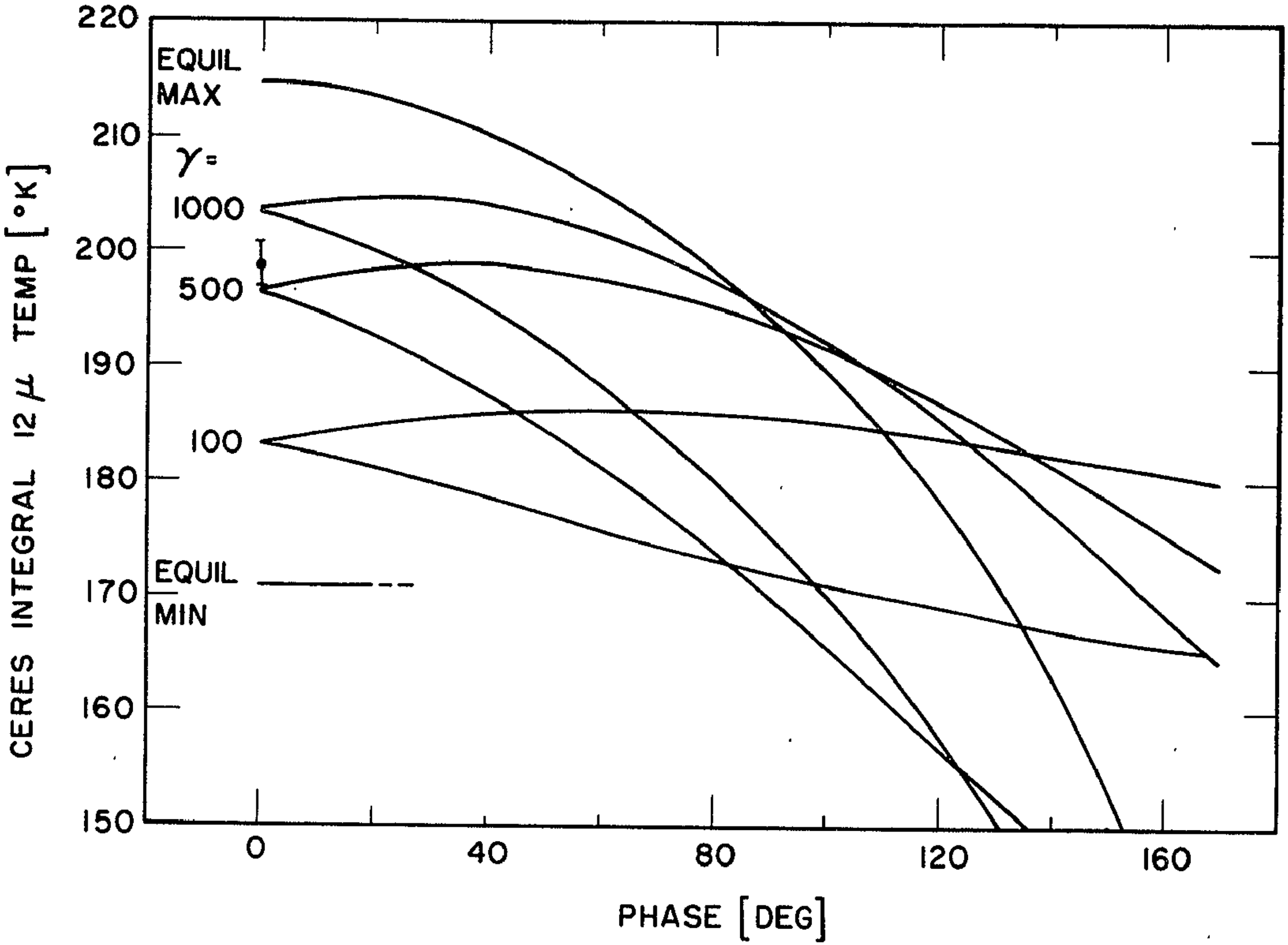

Figure 4.11. Ceres day side integral 12μ solutions as a function of Gamma and phase. The datum is that of Murdock.

Figure 4.11

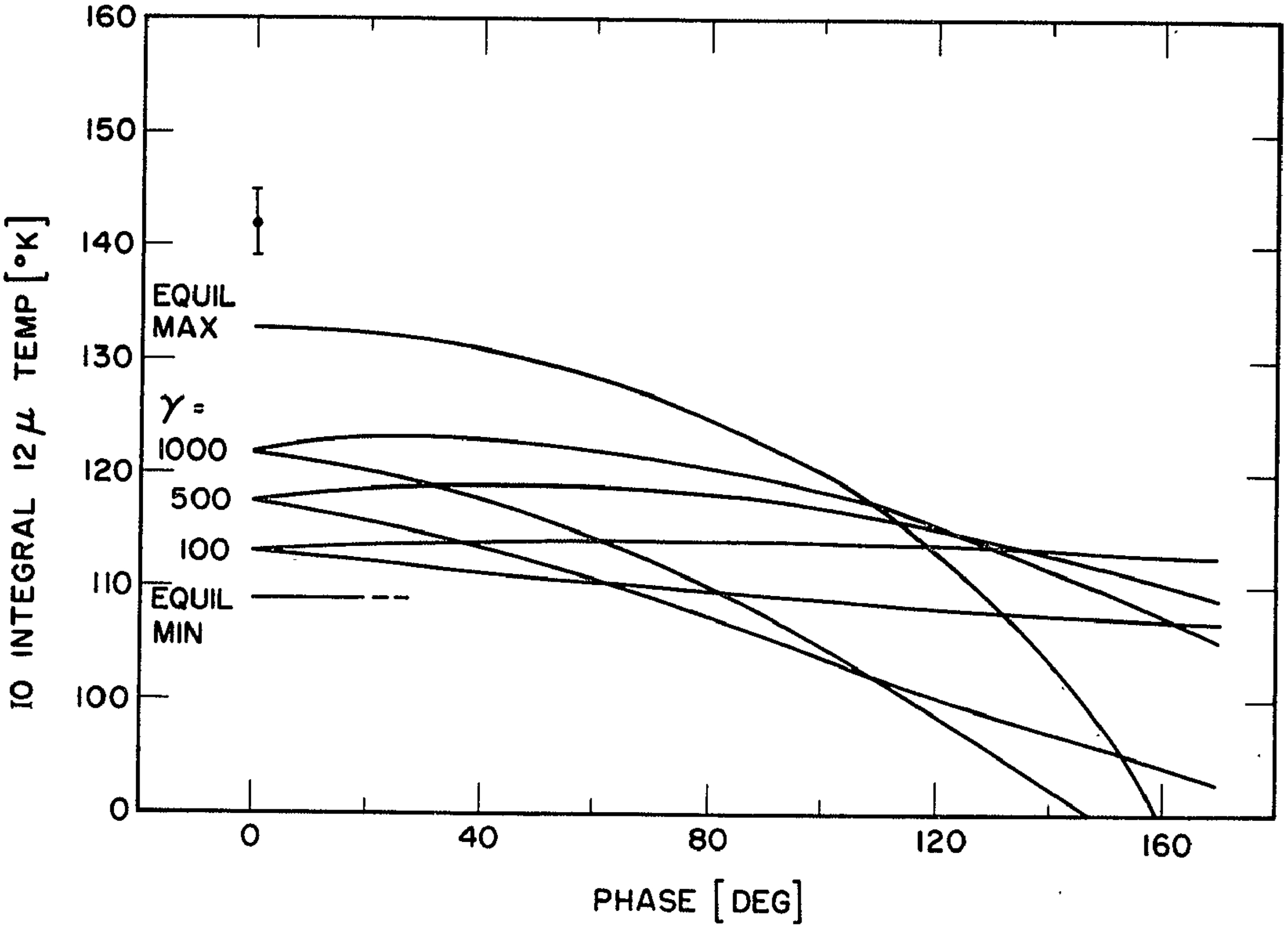

Figure 4.12. Io day side integral 12μ solutions as a function of Gamma and phase. The datum is that of Gillett et. al. (1970).

Figure 4.12

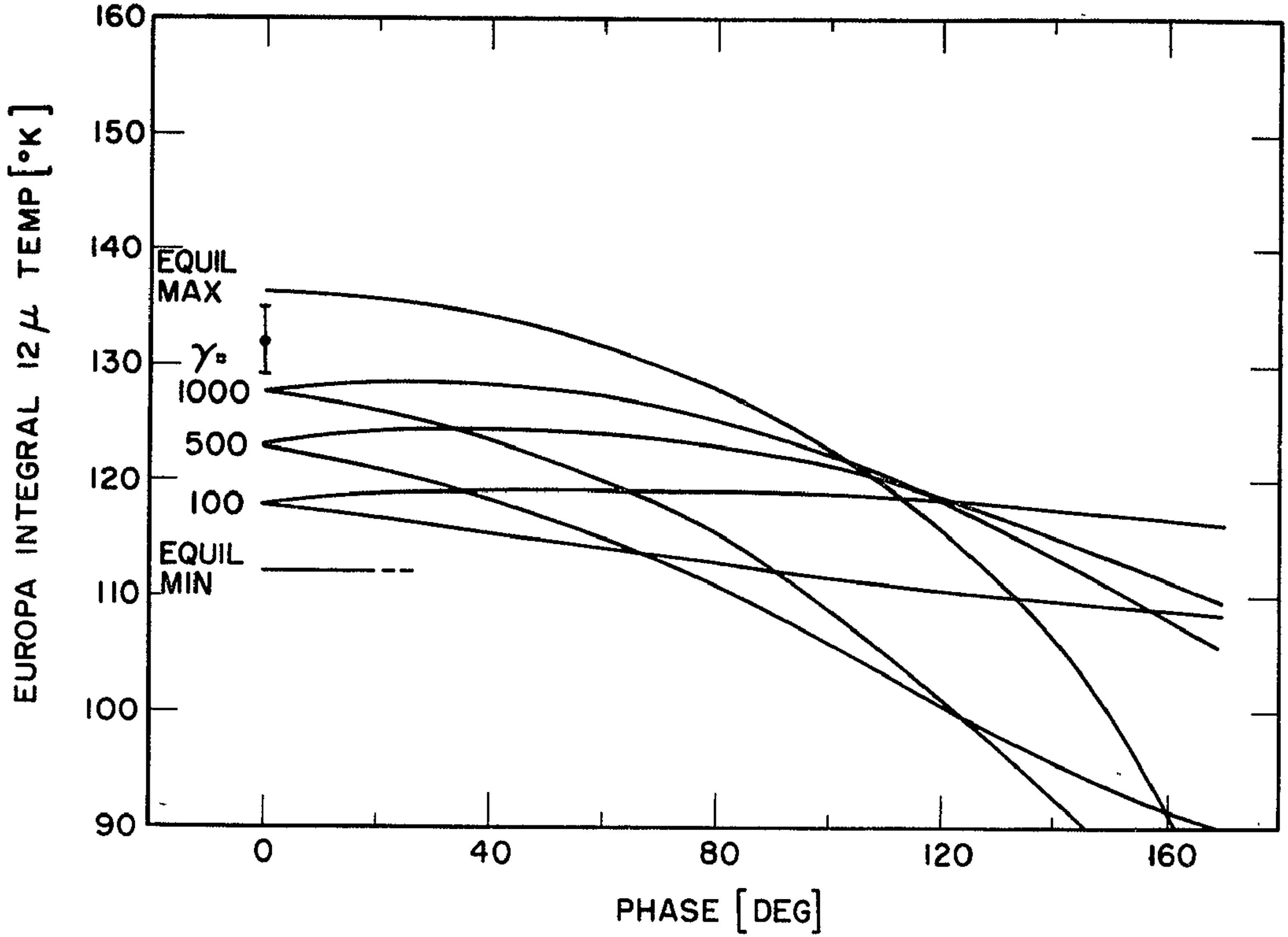

Figure 4.13. Europa day side integral 12μ solutions as a function of Gamma and phase. The datum is that of Gillett et. al. (1970).

Figure 4.13

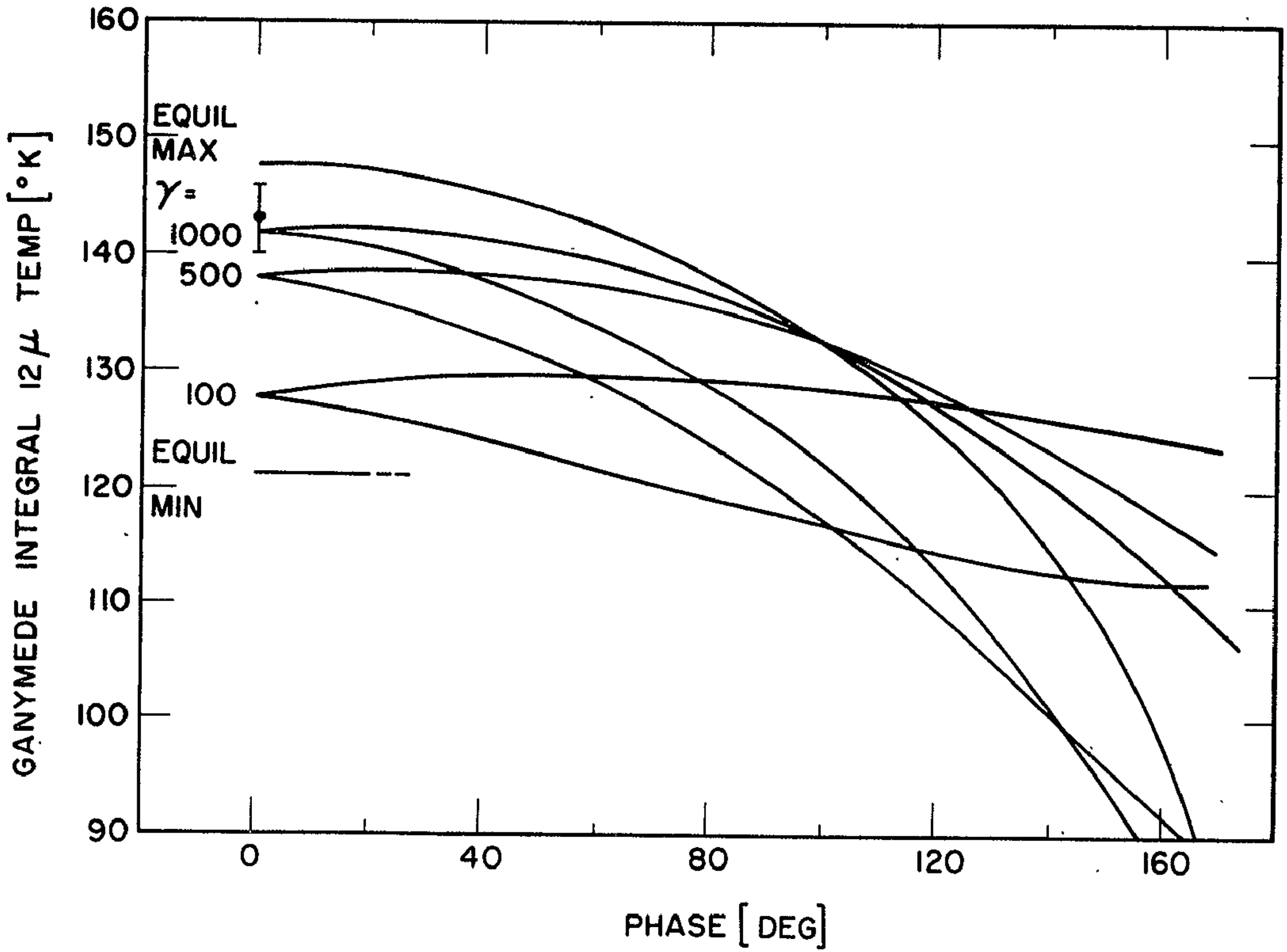

Figure 4.14. Ganymede day side integral 12μ solutions as a function of Gamma and phase. The datum is that of Gillett et. al.(1970).

Figure 4.14

Figure 4.15

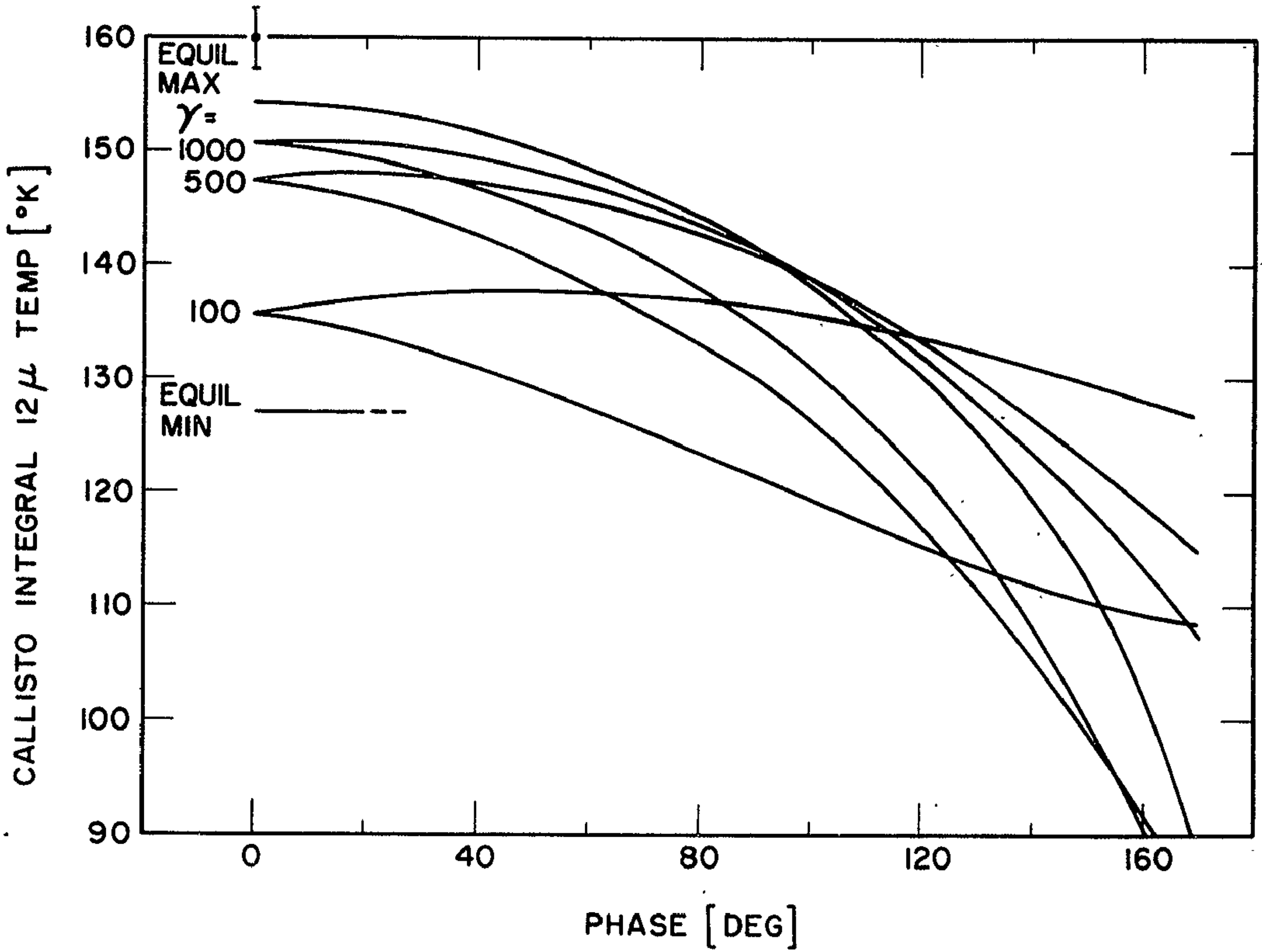

Figure 4.15. Callisto day side integral 12μ solutions as a function of Gamma and phase. The datum is that of Gillett et. al.(1970).

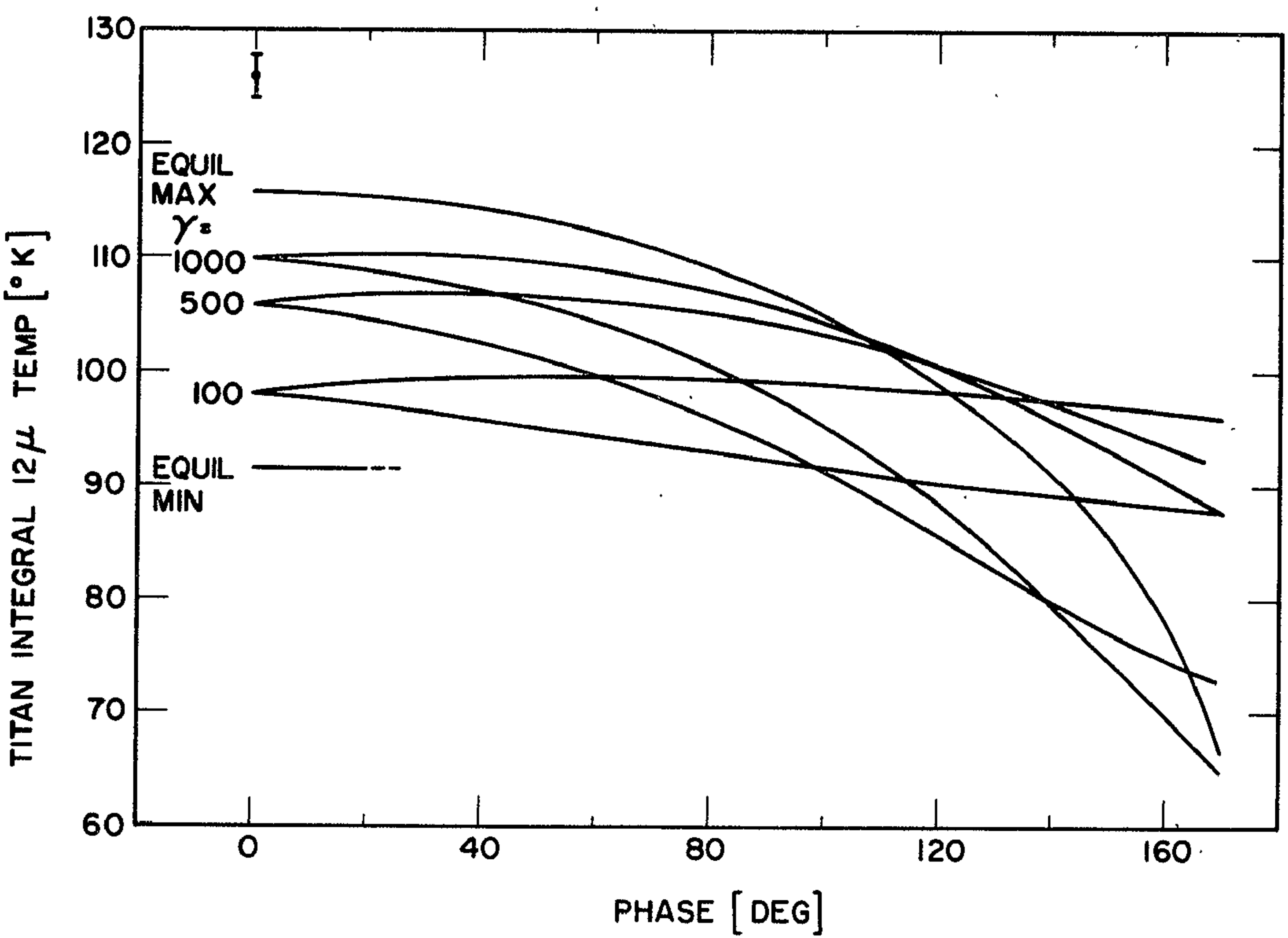

Figure 4.16. Titan day side integral 12μ solutions as a function of Gamma and phase. The datum is that of Allen and Murdock (1971).

Figure 4.16

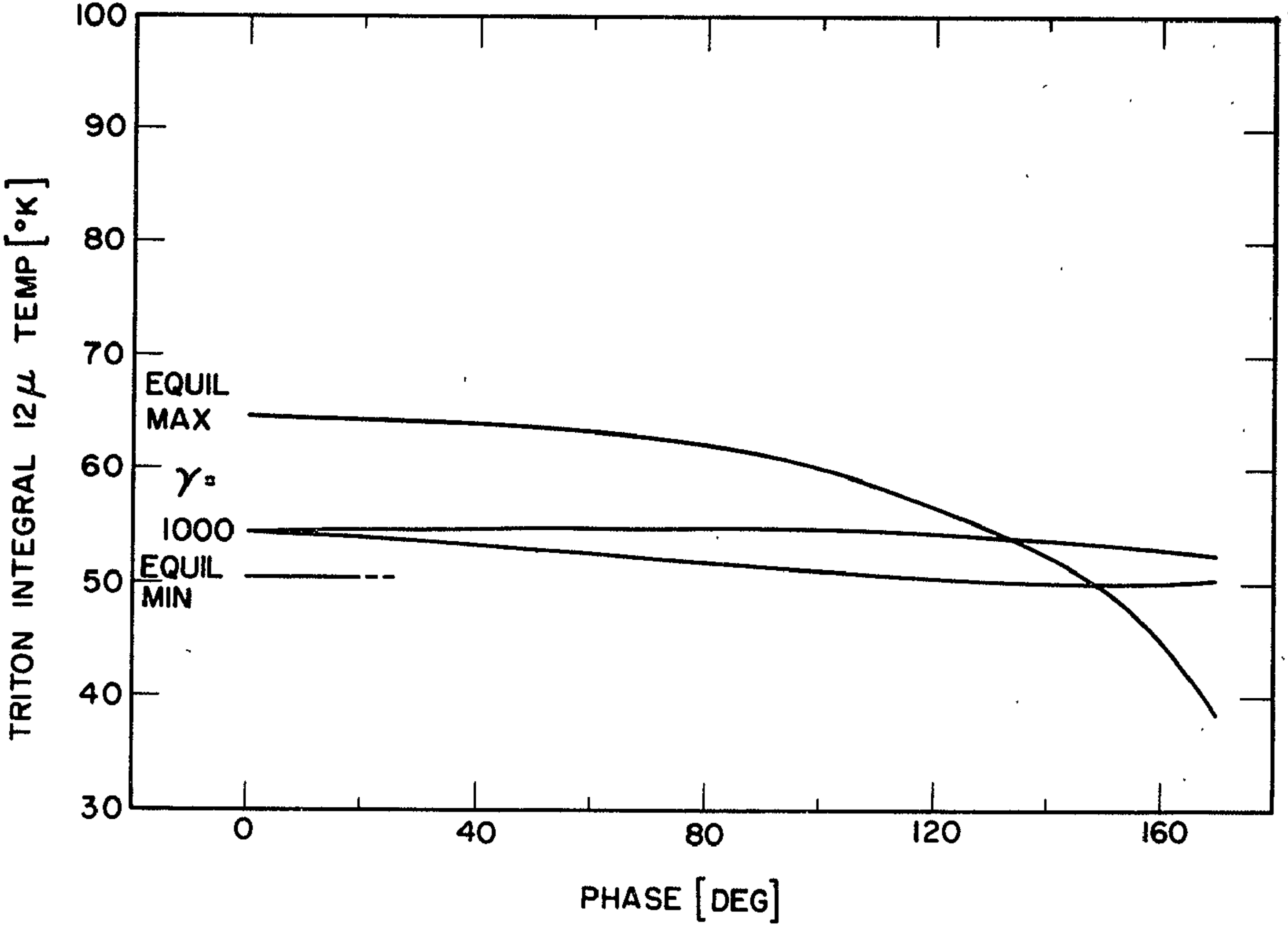

Figure 4.17. Triton day side integral 12μ solutions as a function of Gamma and phase.

Figure 4.17

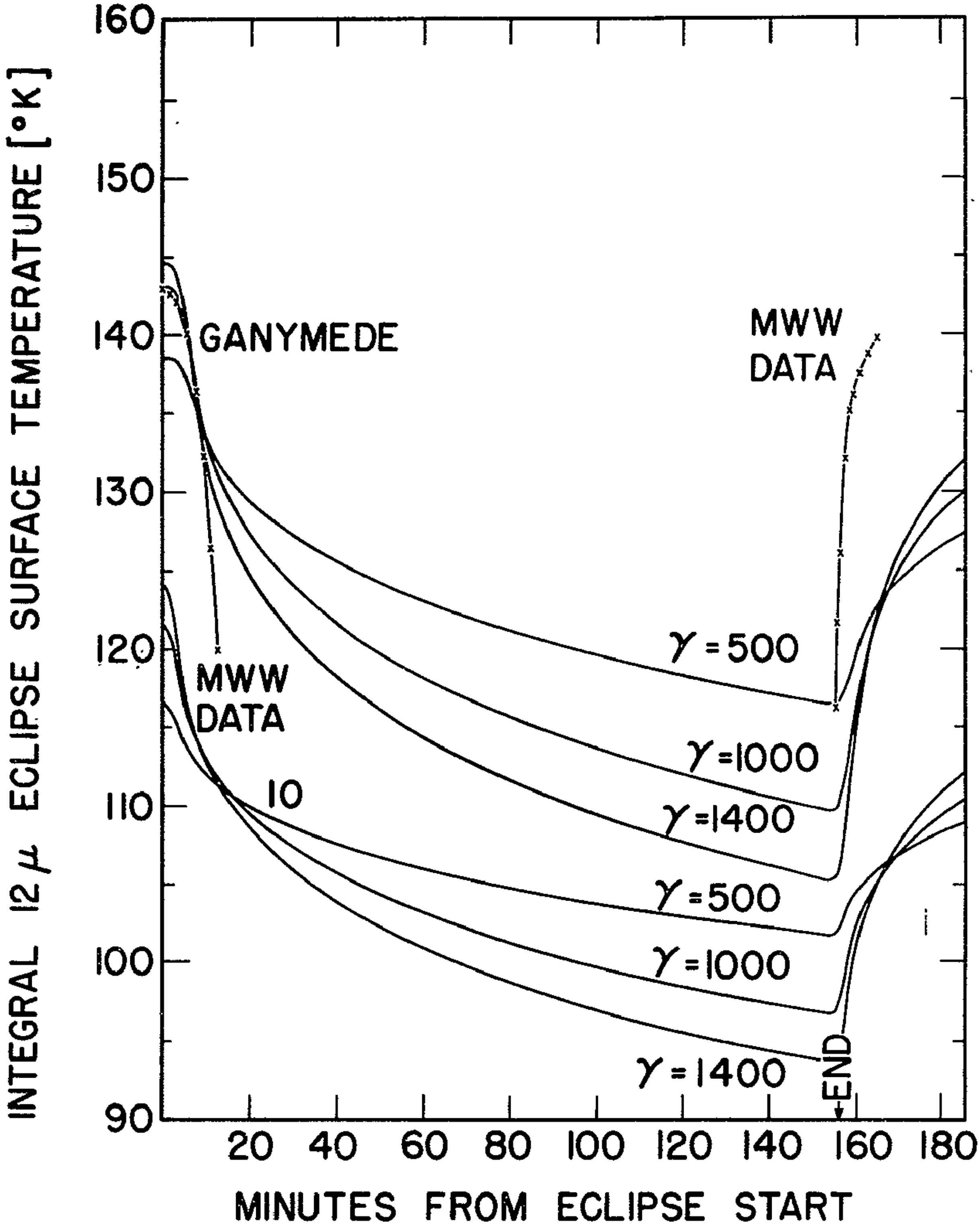

Figure 4.18. Io and Ganymede integral 12μ solutions in eclipse for Gamma = 500,1000, and 1400.

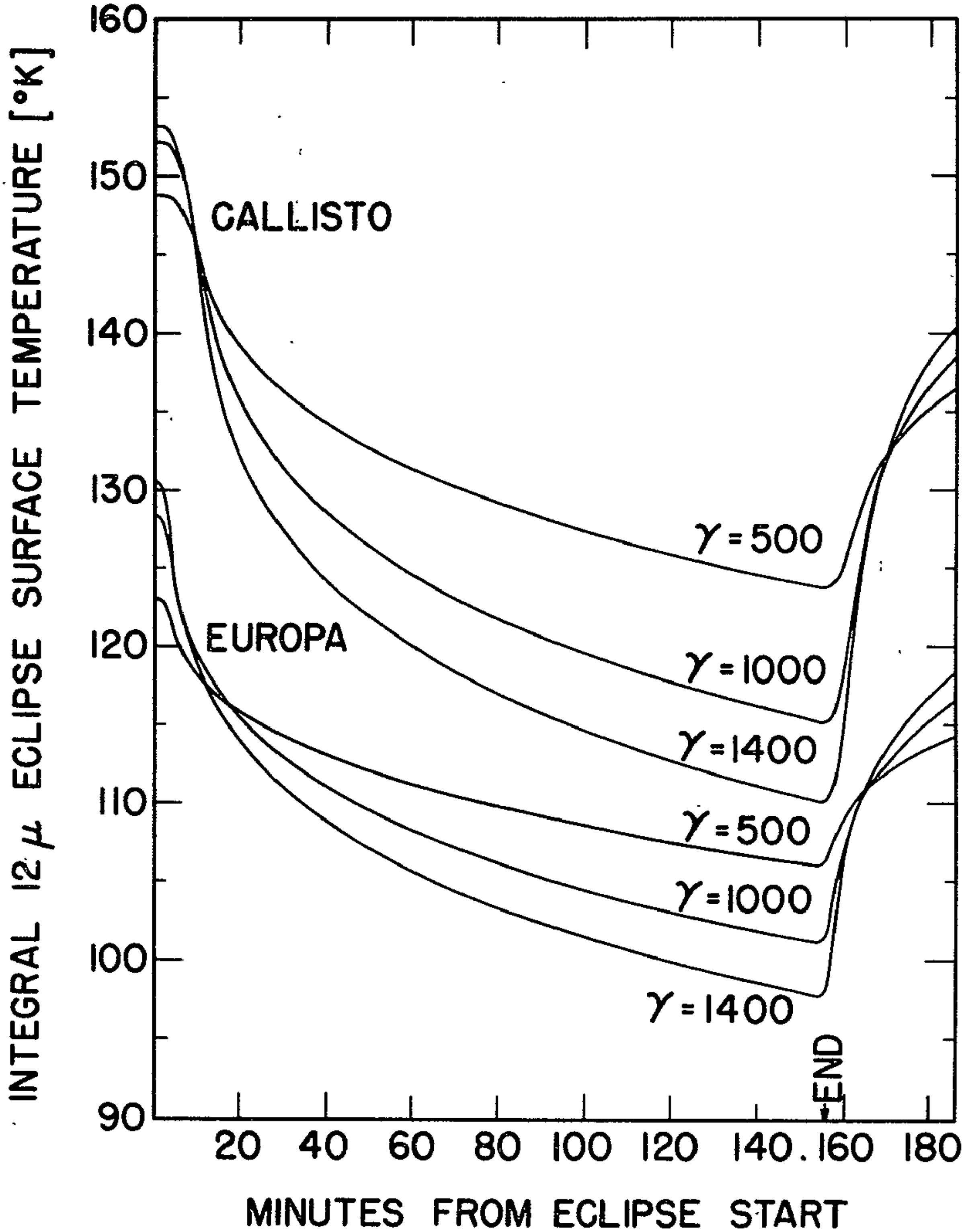

Figure 4.19. Europa and Callisto integral 12μ solutions in eclipse for Gamma = 500,1000, and 1400.

```
      PROGRAM BTEMP5(OUTPUT,PUNCH)
      DIMENSION UP(200),AL(200),AG(200),CM(200),SY(200),D(6)
      DIMENSION X1(121),IMAGE(2000),NX(3),NY(3),AXS(16)
      DIMENSION Y1(121),Y2(121),Y3(121),Y4(121),Y5(121),Y6(121)
      DIMENSION PLNAME(3),X2(121),THOLD(122,13),PSAVE(3,10)
      DIMENSION DX(5),A(5),A1(5),A2(5),A3(5),C1(5),C2(5),C3(5)
      DIMENSION FSUN(100),OUP(200),ODP(200),OX(3,12),IORD(13)
      DATA SIG/1.3543E-12/,PI/3.141592653/,PII/6.283185307/
      DATA DR/0.01745329252/,RD/57.295779518/,PSAVE/30*0.0/
      DATA SUNRAD/0.032533/,ICLIPSE/0/,NX/16,8,3/,NY/9,5,-1/
*
*     SETUP BATCH PROCESSING LOOPS HERE FOR PARTICULAR RUNS
*     RHO(SPECIFIC HEAT),XKAPA(THERM COND),XLONG,XLAT,AND
*     TEMPB(BOTTOM TEMP) MUST ALL BE DEFINED HERE IN CGS UNITS
*
*     JUMP TO DESIRED CELESTIAL OBJECT AND OBTAIN MODEL PARAMETERS
*
      GO TO (100,200,300,400,500,600,700,800,900) MBODY
*
*     MOON PARAMETERS
*
100   PLNAME(1)=10HLUNAR
      PLNAME(2)=10HTEMPERATUR $ PLNAME(3)=10HE
      JR=4 $ SPH=0.2 $  EMS=0.93 $ ALB=0.07 $ ICLIPSE=1
      FPER=1.0/(3.0*120.0) $ FWAVE=0.05 $ XWAVE=5.0
      PER=2.5514429E6 $ R=1.0 $ IORD(1)=0
      DO 18 I=2,9
18    IORD(I)=IORD(I-1)+50
      BTEMP=IORD(1) $ TTEMP=IORD(9) $ GO TO 50
*
*     MERCURY PARAMETERS
*
200   PLNAME(1)=10HMERCURIAN
      PLNAME(2)=10HTEMPERATUR $ PLNAME(3)=10HE
      OPER=87.9686 $ SPER=OPER*2./3. $ B=.387099 $ E=.205629
      JR=4 $ SPH=0.2 $ EMS=0.93 $ ALB=0.07 $ PER=1.52064E7
      FPER=1.0/(6.0*120.0) $ FWAVE=0.05 $ XWAVE=5.0
      TFP=TA $ XM=TFP*PII/OPER $ SA=TFP*PII/SPER
      V=(2.0*E-0.25*E**3)*SIN(XM)+(5.0*E*E/4.0-11.0*E**4/24.0)
     X*SIN(2.0*XM)+13.0*E**3*SIN(3.0*XM)/12.0+103.0*E**4
     X*SIN(4.0*XM)/96.0+XM
      R=B*(1.0-E*E)/(1.0+E*COS(V))
      IORD(1)=0
      DO 218 I=2,9
218   IORD(I)=IORD(I-1)+100
      BTEMP=IORD(1) $ TTEMP=IORD(9) $ GO TO 50
*
*     MOON ECLIPSE PARAMETERS
*
300   PLNAME(1)=PLNAME(1)
      PLNAME(2)=10HECLIPSE TE $ PLNAME(3)=10HMPERATURE
      MBODY=3 $ JR=1 $ ICLIPSE=0
      RE=3.363 $ DA=0.919 $ VELSUN=0.0004718
      US = 0.84 $ VS = -0.20
```

```
      RF = SQRT((1.0 + RE)**2-DA*DA)
      DO 320 I6=1,100
      PRAD=I6*0.01-0.005 $ THETA=ASIN(PRAD)
      DFLUX=(1.0-US-VS+US*COS(THETA)+VS*COS(THETA)**2)/
     X (1.0-US/3.0-VS/2.0)
 320  FSUN(I6)=0.02*PRAD*DFLUX
      EPER=2.0*RF/VELSUN $ PER=EPER+1800.0
      OUP(1)=UP(1) $ ODP(1)=-DX(1) $ I=2 $ IDUMB=MTXS+1
      DO 343 J=1,5
      DO 343 K=1,IDUMB
      OUP(I)=UP(I) $ ODP(I)=ODP(I-1)+DX(J) $ I=I+1
 343  CONTINUE
      GO TO 50
*
*     VESTA PARAMETERS
*
 400  PLNAME(1)=10HVESTA
      PLNAME(2)=10HTEMPERATUR $ PLNAME(3)=10HE
      JR=4 $ SPH=0.2 $ EMS=0.93 $ ALB=0.07 $ R=2.36
      FPER=1.0/(3.0*120.0) $ FWAVE=0.05 $ XWAVE=5.0
      PER=19200.0 $ IORD(1)=0
      DO 318 I=2,9
 318  IORD(I)=IORD(I-1)+30
      BTEMP=IORD(1) $ TTEMP = IORD(9) $ GO TO 50
 500  CONTINUE
 600  CONTINUE
 700  CONTINUE
 800  CONTINUE
 900  CONTINUE
*
*     THE STEP SIZES AND NUMBER OF STEPS ARE SET UP
*
 50   DT=PER*FPER $ DPLOT=PER/120
      DIFF=XKAPA/(RHO*SPH)
      TWAVE=SQRT(DIFF*PER/PI)
      GAMMA=1.0/SQRT(XKAPA*RHO*SPH)
      DX(1)=TWAVE*FWAVE
      DX(2)=1.50*DX(1)
      DX(3)=2.25*DX(1)
      DX(4)=3.38*DX(1)
      DX(5)=5.06*DX(1)
      MTXS=TWAVE*XWAVE/(DX(1)+DX(2)+DX(3)+DX(4)+DX(5))
      MTX=MTXS*5 + 6
*
*     THE DEPTHS AT WHICH THE 6 PLOT VALUES ARE TAKEN
*
      D(1)=0
      D(2)=5.0*DX(1)
      D(3)=7.0*DX(1)+2.0*DX(2)
      D(4)=7.0*DX(1)+6.0*DX(2)
      D(5)=7.0*DX(1)+8.0*DX(2)+1.0*DX(3)
      D(6)=7.0*DX(1)+8.0*(DX(2)+DX(3)+DX(4)+DX(5))
*
*     IN ECLIPSE CASE REARRANGE KNOWN SUR TEMP FOR NEW DEPTH
```

```
*
      IF(MBODY.EQ.3) 340,623
340   I=2 $ L=1 $ DEP=-DX(1) $ IDUMB=MTXS+1
      UP(1)=OUP(1)+(OUP(2)-OUP(1))*(DEP-ODP(1))/(ODP(2)-ODP(1))
      DO 330 J=1,5 $ DO 330 K=1,IDUMB
      DEP=DEP+DX(J)
      IF(DEP.GE.ODP(L).AND.DEP.LE.ODP(L+1)) GO TO 335
      L=L+1
      IF(DEP.GE.ODP(L).AND.DEP.LE.ODP(L+1)) GO TO 335
      STOP 4
335   UP(I)=OUP(L)+(OUP(L+1)-OUP(L))*(DEP-ODP(L))/
     X (ODP(L+1)-ODP(L))
      I=I+1
330   CONTINUE
      GO TO 570
*
*     INITIAL EQUIL BB SURFACE TEMP IS FOUND
*
623   RLAT=XLAT*DR $ RLONG=XLONG*DR $ COSLAT=COS(RLAT)
      S1=SUNRAD*COSLAT*(1.0-ALB)/(R*R) $ S2=PII/PER
      TEMPS=SQRT(SQRT(S1*COS(RLONG)/(EMS*SIG)))
*
*     INITIAL TEMP WITH DEPTH ARE FOUND
*
      K7=1.0 $ IF(GAMMA.LT.150.0) K7=0.0
622   AMP=(TEMPS-TEMPB)/COS(RLONG) $ DEP=0.0 $ J4=2
      DO 11 J=1,5
      IDUMB=MTXS+1
      DO 10 I=1,IDUMB
      PG=DEP/TWAVE $ PH=PG-RLONG
      UP(J4)=TEMPB+AMP*EXP(-PG)*COS(PH)
      DEP=DEP+DX(J)
10    J4=J4+1
11    CONTINUE
      UP(1)=UP(2)+(UP(2)-UP(3))
*
*     COEFS FOR THE C-N SURFACE,BOTTOM,AND LAYER EQS
*
570   F1=2.0*DX(1)/XKAPA
      DO 533 I=1,5
      A(I)=DIFF*DT/DX(I)**2
      A1(I)=2.0*A(I)
      A2(I)=2.0-A1(I)
533   A3(I)=2.0+A1(I)
*
*     COEFS FOR C-N INTERNAL BOUNDARY EQS
*
      DO 534 I=1,4
      C1(I)=1.0/DX(I)
      C2(I)=1.0/DX(I+1)
534   C3(I)=DIFF*DT/(DX(I)+DX(I+1))
*
*     COEFS FOR GAUSSS SOLUTION TO EQS
*
```

```
      AL(1)=-A1(1) $ CM(1)=A3(1) $ J=2
      DO 536 K=1,5
      DO 537 L=1,MTXS
      CM(J)=-A(K)
      AL(J)=A3(K)+A(K)*CM(J-1)/AL(J-1)
      AG(J)=A(K)/AL(J-1)
537   J=J+1
      GO TO (504,504,504,504,536)K
504   CM(J)=-C3(K)*C2(K)
      AL(J)=1.0+C3(K)*(C2(K)+C1(K))+C3(K)*C1(K)*CM(J-1)/AL(J-1)
      AG(J)= C3(K)*C1(K)/AL(J-1)
      J=J+1
536   CONTINUE
*
*     PERIOD LOOP PARAMETERS
*
15    IF(JR.EQ.0) GO TO 70
      JR=JR-1 $ T=0.0 $ DAY=0.0 $ PTIME=DPLOT $ DM=DT/60.0
      IF(JR.GT.0) GO TO 586
      PRINT 14
   14 FORMAT(1H1)
      DLONG=XLONG*RD
      PRINT 305,PLNAME(1),DM,DX(1),MTX,TWAVE,GAMMA,XLAT,DLONG,JR
305   FORMAT(/,1X,A8,* MODEL PARAMETERS   DT=*,F7.2,*MIN   DX=*
     X,F6.2*CM   MTX=*I3*   TWAVE=*F6.2*CM   GAMMA=*F7.2
     X*  XLAT=*F6.2* XLONG=*F7.2*  JR=*I1)
      PRINT 306,(D(I),I=1,6)
306   FORMAT(/10X*TEMP(K) RECORDED AT FOLLOWING DEPTHS(CM)   A =*
     XF7.2*   B =*F7.2*   C =*F7.2*   D =*F7.2*   E = *F7.2
     X*   F =*F7.2)
      PRINT 307
307   FORMAT(*              FOR X.X DAYS AT SUN ANGLE X.X*)
*
*     ONCE EVERY N HOURS PRINT
*
586   DO 19 K1=1,121
      Y1(K1)=UP(2)
      IF(JR.GT.0) GO TO 309
      IF(MBODY.EQ.2) GO TO 581
      SUNANG = RD*ACOS(COSLAT*COS(RLONG+S2*T))
      GO TO 589
581   TFP=DAY+TA $ XM=TFP*PII/OPER $ SA=TFP*PII/SPER
      V=(2.0*E-0.25*E**3)*SIN(XM)+(5.0*E*E/4.0-11.0*E**4/24.0)
     X*SIN(2.0*XM)+13.0*E**3*SIN(3.0*XM)/12.0+103.0*E**4
     X*SIN(4.0*XM)/96.0+XM
      SUNANG=RD*ACOS(COSLAT*COS(SA-V-DS))
589   X1(K1)=DAY
      X2(K1)=SUNANG
      Y2(K1)=UP(7)
      Y3(K1)=UP(11)
      Y4(K1)=UP(15)
      Y5(K1)=UP(18)
      Y6(K1)=UP(MTX)
      PRINT 308,X1(K1),SUNANG,Y1(K1),Y2(K1),Y3(K1),Y4(K1)
```

```
     X,Y5(K1),Y6(K1),K1
308   FORMAT(11X,F7.3,15X,F6.2,9X,6(F6.2,7X),3X,I3)
309   IF(K1.GE.121) GO TO 19
*
*     THE MAIN COMPUTING LOOP
*
30    T=T+DT $ DAY=T/86400.0
*
*     MAKE FIRST GUESS OF SURFACE TEMP
*
      GO TO (590,591,592,590,590,590,590,590,590) MBODY
590   SURRAD=S1*COS(RLONG+S2*T)
      GO TO 599
591   TFP=DAY+TA $ XM=TFP*PII/OPER $ SA=TFP*PII/SPER
      V=(2.0*E-0.25*E**3)*SIN(XM)+(5.0*E*E/4.0-11.0*E**4/24.0)
     X*SIN(2.0*XM)+13.0*E**3*SIN(3.0*XM)/12.0+103.0*E**4
     X*SIN(4.0*XM)/96.0+XM
      RI=B*(1.0-E*E)/(1.0+E*COS(V))
      SURRAD=S1*(R*R)*COS(SA-V-DS)/(RI*RI)
      GO TO 599
592   RX=SQRT((RF-VELSUN*T)**2+DA*DA)
      AREA=0.0
      DO 593 I9=1,100
      PRAD=I9*0.01-0.005
      IF(RX.LT.PRAD+RE) GO TO 594
      PHI=0.0 $ GO TO 593
594   IF(RE.LT.RX+PRAD) GO TO 595
      PHI=PI $ GO TO 593
595   PHI=ACOS((PRAD*PRAD+RX*RX-RE*RE)/(2.0*PRAD*RX))
593   AREA=AREA+FSUN(I9)*(PI-PHI)/PI
      SURRAD=S1*AREA*COS(RLONG+PII*T/2.5514429E6)
      GO TO 599
599   IF(SURRAD.LT.0.0) SURRAD = 0.0
      D1=A(1)*UP(1)+A2(1)*UP(2)+A(1)*UP(3)
      D2=A(1)*UP(2)+A2(1)*UP(3)+A(1)*UP(4)
      T4=UP(4)+A(1)*(UP(3)-2.0*UP(4)+UP(5))
      G1=A(1)*F1*SIG*EMS
      G2=(A3(1)-2.0*A(1)*A(1)/A3(1))
      G3=(A1(1)*(D2+A(1)*T4)/A3(1)+A(1)*F1*SURRAD+D1)
      UN3=UP(2)
      DO 440 K4=1,100
      UN2=(3.0*G1*UN3**4+G3)/(4.0*G1*UN3**3+G2)
      IF(ABS(UN2-UN3).LT.0.01) GO TO 640
440   UN3=UN2
      PRINT 441
441   FORMAT(*       440 DO LOOP ITERATION EXCEEDED*)
640   F = F1*(EMS*SIG*UN2**4-SURRAD)
*
*     THE GAUSSIAN SOLUTION PARAMETERS ARE CALCULATED
*
      SY(1)=A(1)*UP(1)+A2(1)*UP(2)+A(1)*UP(3)+A(1)*F
      J=2
      DO 546 K=1,5
      DO 547 L=1,MTXS
```

```
      SY(J)=A(K)*UP(J-1)+A2(K)*UP(J)+A(K)*UP(J+1)+AG(J)*SY(J-1)
547   J=J+1
      GO TO (554,554,554,554,546)K
554   SY(J)=C3(K)*C1(K)*UP(J-1)+(1.0-C3(K)*(C2(K)+C1(K)))*UP(J)
     X+C3(K)*C2(K)*UP(J+1)+AG(J)*SY(J-1)
      J=J+1
546   CONTINUE
      IDUMB=MTX-1
      DO 20 N=1,IDUMB
      M=MTX-N
20    UP(M)=(SY(M)-CM(M)*UP(M+1))/AL(M)
      IF(ABS(PTIME-T).GT.10.0) GO TO 30
      PTIME=PTIME+DPLOT
19    CONTINUE
*
*     A PERIOD IS PAST, A PLOT IS MADE
*
      ASUM=2.0*Y1(3)
      DO 732 L5=3,120
732   ASUM=ASUM+Y1(L5)
      TEMPB=ASUM=ASUM/120.0
      JX=JR+1
      PSAVE(1,JX)=JR $ PSAVE(2,JX)=Y1(60) $ PSAVE(3,JX)=TEMPB
      IF(JR.GT.0) GO TO 735
      PRINT 14
      IX=1
      DO 17 I=1,16
      AXS(I)=X1(IX)
17    IX=IX+8
      CALL PRNPLOT(0, 8,15,1,120,51,IMAGE)
      CALL PRNPLOT(1,0.0,ASS(16),BTEMP,TTEMP,51,IMAGE)
      CALL PRNPLOT(2,NX,NY,3,1,51,IMAGE)
      CALL PRNPLOT(3,1HF,X1,Y6,121,51,IMAGE)
      CALL PRNPLOT(3,1HE,X1,Y5,121,51,IMAGE)
      CALL PRNPLOT(3,1HD,X1,Y4,121,51,IMAGE)
      CALL PRNPLOT(3,1HC,X1,Y3,121,51,IMAGE)
      CALL PRNPLOT(3,1HB,X1,Y2,121,51,IMAGE)
      CALL PRNPLOT(3,1HA,X1,Y1,121,51,IMAGE)
      CALL PRNPLOT(4,30,PLNAME,ASS,IORD,7,IMAGE)
      PRINT 306,(D(I),I=1,6)
      DLONG=XLONG*RD
      PRINT 305,PLNAME(1),DM,DX(1),MTX,TWAVE,GAMMA,XLAT,DLONG,JR
      PRINT 733,(PSAVE(I),I=1,15)
733   FORMAT(5(* (JR=*F1.0* MT=*F6.2* AT=*F6.2*)*))
735   IF(K7.LT.1) GO TO 15
      TEMPS=UP(2)
      K7=0 $ GO TO 622
*
*     BATCH PROCESSING LOOPS FOR PARTICULAR RUNS
*
70    CONTINUE
      END
```